Wireless Power Transfer for Implantable Biomedical Devices Using Adjustable Magnetic Resonance

by
Basem M. Badr

M.A.Sc., Dept. of Electrical Engineering, King Saud University, Saudi Arabia, 2011
B.Sc., Dept. of Electrical Engineering, Mansoura University, Egypt, 2007

A Dissertation Submitted in Partial Fulfillment
of the Requirements for the Degree of

DOCTOR OF PHILOSOPHY

in the Department of Mechanical Engineering

© Basem M. Badr, 2016
University of Victoria

All rights reserved. This dissertation may not be reproduced in whole or in part, by photocopy or other means, without the permission of the author.

Supervisory Committee

Wireless Power Transfer for Implantable Biomedical Devices Using Adjustable Magnetic Resonance

by
Basem M. Badr

M.A.Sc., Dept. of Electrical Engineering, King Saud University, Saudi Arabia, 2011
B.Sc., Dept. of Electrical Engineering, Mansoura University, Egypt, 2007

Supervisory Committee

Prof. Nikolai Dechev, Dept. of Mechanical Engineering, University of Victoria

Supervisor

Prof. Kerry R. Delaney, Dept. of Biology, University of Victoria

Co-Supervisor

Prof. Yang Shi, Dept. of Mechanical Engineering, University of Victoria

Departmental Member

Prof. Jens Bornemann, Dept. of Electrical and Computer Engineering, University of Victoria

Outside Member

Abstract

Supervisory Committee
Prof. Nikolai Dechev, Dept. of Mechanical Engineering, University of Victoria
Supervisor
Prof. Kerry R. Delaney, Dept. of Biology, University of Victoria
Co-Supervisor
Prof. Yang Shi, Dept. of Mechanical Engineering, University of Victoria
Departmental Member
Prof. Jens Bornemann, Dept. of Electrical and Computer Engineering, University of Victoria
Outside Member

Rodents are essential models for research on fundamental neurological processing and for testing of therapeutic manipulations including drug efficacy studies. Telemetry acquisition from rodents is important in biomedical research and requires a long-term powering method. A wireless power transfer (WPT) scheme is desirable to power the telemetric devices for rodents. This dissertation investigates a WPT system to deliver power from a stationary source (primary coil) to a moving telemetric device (secondary coil) via magnetic resonant coupling. The continuously changing orientation of the rodent leads to coupling loss/problems between the primary and secondary coils, presenting a major challenge. We designed a novel secondary circuit employing ferrite rods placed at specific locations and orientations within the coil. The simulation and experimental results show a significant increase of power transfer using our ferrite arrangement, with improved coupling at most orientations. The use of a medium-ferrite-angled (4MFA) configuration further improved power transfer. Initially, we designed a piezoelectric-based device to harvest the kinetic energy available from the natural movement of the rodent; however, the harvested power was insufficient to power the telemetric devices for the rodents. After designing our 4MFA device, we designed a novel wireless measurement system (WMS) to collect real-time performance data from the secondary circuit while testing WPT systems. This prevents the measurement errors associated with voltage/current probes or coaxial cables placed directly into the primary magnetic field. The maximum total efficiency of our novel WPT is 14.1% when the orientation of the 4MFA is parallel to the primary electromagnetic field, and a current of 2.0 A (peak-to-peak) is applied to the primary coil. We design a novel controllable WPT system to facilitate the use of multiple secondary circuits (telemetric devices) to operate within a single primary coil. Each telemetric device can tune or detune its resonant frequency independently of the others using its internal control algorithm.

Table of Contents

List of Tables

List of Figures

List of Abbreviations

Wireless Power Transfer	WPT
Loosely Coupled Wireless Power Transfer	LCWPT
Wireless Measurement System	WMS
Electroencephalogram	EEG
Finite Element Analysis	FEA
Energy Harvesting	EH
Degree-of-Freedom	DOF
Lead Zirconate Titanate	PZT
Polyvinylidene Fluoride	PVDF
Energy Harvester for Small Animal Motion	EHAM
Quick Pack	QP
Macro fiber composite	MFC
Radio Frequency Identification	RFID
Space Solar Power Satellites	SPS
Inductive Power Transfer	IPT
Capacitive power transfer	CPT
Rodent implant device	RID
Secondary implant prototype	SIP
Radio Frequency	RF
Zero Voltage Switching	ZVS
International Commission on Non-Ionizing Radiation Protection	ICNIRP
Non-Ionizing Radiation	NIR
Phase Lock Loop	PLL
Liquid Crystal Polymer	LCP
Flexible Printed Circuit Board	FPCB
Drain Brain Stimulation	DBS
Power Management Unit	PMU
Series Series	SS
Series Parallel	SP

Parallel Series	PS
Parallel Parallel	PP
Four Wrapped Ferrite Rods	WFR_4
Four Medium Ferrite	4MF
Four Medium Ferrite Angled	4MFA
Effective Capture Diameter	ECD
Surface Mount Devices	SMD
Analog to Digital Converter	ADC
Low Effective Series Resistance	ESR
Bandwidth	BW
Contraction Factor	CF
Microcontrollers	MCU
Left Ventricular Assist Devices	LVAD
Secondary Coil	SC
Pulse Width Modulation	PWM
Zero Current Switching	ZCS
Dynamic Tuning/Detuning	DTD
Inductor Capacitor Inductor	LCL
Low Dropout Regulator	LDO
Switching Mode Regulator	SMPS
System on Chip	SOC

List of Symbols

m	is the effective mass of the EHAM
C	is the mechanical damping of the EHAM
K	is the stiffness of the EHAM
f_e	is the effective force due to the piezoelectric element
$X_1(t)$	is the mechanical displacement of the proof mass
$X(t)$	is the applied displacement to the EHAM
D	is matrix representing the electrical displacement (polarization) of the piezoelectric
d	is the matrix representing the strain piezoelectric coefficients
T	is the matrix representing the mechanical strain
ε	is the matrix representing the material permittivity and the electric field
E	is the matrix representing the electric field applied to the piezoelectric
k_m	is the effective electromechanical coupling coefficient of a piezoelectric structure
$V_p(t)$	is the voltage across the piezoelectric electrodes
$Q_p(t)$	is the charge generated on the electrodes
C_{pzt}	is the capacitance of the piezoelectric material
P_{av}	is the power extracted by the transduction mechanism plus the power lost through parasitic damping mechanisms
ζ_T	is the total damping ratio
Y	is the amplitude of the applied external vibration
w	is the frequency of the applied excitation
ω_n	is the natural frequency of the EHAM
P_e	is the electrical power extracted from the EHAM
ζ_E	is the electrical damping ratio
ζ_P	is the mechanical damping ratio
k_{mat}	is the material stiffness of the beam
λ_{eig}	is the eigenvalue of the EHAM
μ_a	is the viscosity of air
ρ_a	is the density (1.3 kg·m^{-3}) of air
τ	is the structural damping coefficient

g is the gap distance (10 mm)

b is the width of the silicon beam

h is the height of the silicon beam

ρ_m is the density of the silicon beam

f is the operating frequency

d_0 is the amplitude of the excitation displacement to the EHAM

$I_R(t)$ is the current of the load

$V_R(t)$ is the voltage of the load

W_{pzt} is the piezoelectric layer width

L_{pzt} is the piezoelectric layer length

H_{pzt} is the piezoelectric layer thickness

ε_o is the permittivity of free space

ε_r is the relative dielectric constant of the piezoelectric layer

R_{piezo} is the inherent impedance for the EHAM

f_{res} is the resonant frequency of the EHAM device or the WPT system

P_{RMS} is the RMS harvested power by the EHAM

P_f is the electrical power values at the applied frequency

R_L is the resistor load

λ is the wavelength of the transmitted signal

r is the separation distance from the radiation source

L_P is the primary coil

C_P is the primary capacitor

L_S is the secondary coil

C_S is the secondary capacitor

I_P is the current applied to the primary coil

N_P is the number of primary turns

a_P is the primary coil radius

a_S is the secondary coil radius

N_S is the number of secondary turns

A_S is the loop area of the secondary coil

μ_r is the relative permeability of a specific medium

μ_0	is the permeability of free space
V_{ind}	is induced voltage onto the secondary coil
Z_s	is the lumped impedance
M_{SP}	is the mutual coupling between the primary and the secondary coils
k	is the coupling coefficient between the primary and the secondary coils
Z_r	is the reflected impedance
Q_P	is the quality factor of the primary coil
Q_S	is the quality factor of the secondary coil
P_o	is the received power
R	is the resistive loss of the secondary tank
ψ_{SP}	is the total flux captured by the secondary coil
B_C	is the flux density crossing perpendicularly through the secondary coil
V_G	is the gate driver signal to the MOSFET
C_{par}	is the parallel capacitor in Class-E amplifier
C_{ser}	is the series capacitor in Class-E amplifier
L_{Choke}	is the choke inductor in Class-E amplifier
V_{CC}	is the DC power supply in Class-E amplifier
C_{oss}	is the output capacitance of the MOSFET
V_{rec}	is the rectified voltage
R_{LC}	is the impedance of the L_SC_S-tank circuit
$\eta_{DC\text{-}Load}$	is the end-to-end efficiency, from the DC supply source to the application load
P_{in}	is the total DC input power to the system (i.e. into the power amplifier and transfer link)
η	is the efficiency of a two coil system using magnetic resonant coupling
d	is the separation distance between the coils
C_{Pn}	is the normalized primary capacitance
w_o	is the resonant frequency of the design WPT system
R_{AC}	is the ac resistance of a coil
C_{self}	is the equivalent parasitic capacitance of a coil
R_{DC}	is the dc resistance of the coil
f_h	is the frequency at which power dissipation of the coil is twice the dc power

	dissipation
r_s	is the radius of an individual strand
σ	is the conductivity of the conductor
N_t	is the total of turns
N_{st}	is the number of strands
β	is the area efficiency defined as the ratio of the total conducting area over the cross section of the winding,
υ	is the parameter defined to characterize a coil's geometry properties
f_{peak}	is the frequency at which a coil has maximum quality factor
Q_{peak}	is the maximum quality factor
f_1	is the lower cut-off frequency
f_2	is the upper cut-off frequency
l	is the length of the coil
$\hat{x}$	is a unit vector of the transmission distance along *x*-axis
C_{parmos}	is the parasitic capacitance effect of the MOSFET
w_t	is the width trace of the PCB
I	is the maximum current in RMS value (8 A) passes in the PCB traces
ΔT	is temperature difference
t_{pcb}	is the thickness of the PCB
I_{ind}	is the induced current in the secondary circuit
Z_2	is the impedance of the secondary circuit
L_{DC}	is the dc inductor
C_{DC}	is the dc capacitor
Z_{oc}	is the open-circuit impedance
C_C	is the coupling capacitor of the half-bridge rectifier
C_{smooth}	is the smoothing capacitor of the half-bridge rectifier
L_{eq}	is the equivalent secondary inductance due to the mutual coupling
Z_{rtot}	is the total reflected impedance from the multiple RIDs
n	is the number of the RIDs in the cage
M_{SPn}	is the equivalent mutual inductance of the multiple RIDs
k_n	is the equivalent coupling coefficient of the multiple RIDs

R_P is the equivalent parallel resistance of the secondary coil

C_{iss} is the input capacitance of the MOSFET, is measured between the gate and the source, with the drain shorted to the source

C_{oss} is the output capacitance of the MOSFET, is measured between the drain and the source, with the gate shorted to the source

C_{rss} is the reverse transfer capacitance of the MOSFET, is measured between the drain and the gate, with the source is connected to the ground

C_{GD} is the gate-drain capacitance of the MOSFET

C_{GS} is the gate-source capacitance of the MOSFET

C_{DS} is the drain-source capacitance of the MOSFET

Acknowledgments

I would like to express my sincere appreciation and thanks to my advisor Professor Nikolai Dechev: you have been a tremendous mentor for me. I would like to thank you for encouraging my research and for allowing me to grow as a research scientist. Your advice on both research as well as on my career have been priceless. I would also like to thank Professor Kerry Delaney for his invaluable insights and suggestions. I really appreciate your willingness to meet me on short notice every time and going through my thesis progress reports; you are an inspiration.
I am also very grateful to my committee members Professor Yang Shi and Professor Jens Bornemann for serving as my committee members. I also want to thank you for letting my defense be an enjoyable moment, and for your brilliant comments and suggestions.
I would like to acknowledge those who have helped with technical aspects: Art Makosinski (manager of laboratories at Dept. of Mechanical Engineering, University of Victoria), Robert Somogyi-Csizmazia, and Paul Leslie (Research Associate with the Neurobiology department at University of Victoria). I am most grateful to my father Mohamed Badr. Without his love and support, this endeavour could not be accomplished.
Finally, I would like to acknowledge the most important person in my life – my wife Corina Botelho. She has been a constant source of strength and inspiration. There were times during the past few years when everything seemed hopeless. I can honestly say that it was only her determination and constant encouragement (and sometimes a kick on my backside when I needed one) that ultimately made it possible for me to see this project through to the end.

Dedication

This thesis is dedicated
to my mother, Nemat Elborgy
and to my loving wife, Corina Botelho.

Chapter 1: Introduction

1.1 Motivation

Biomedical devices are useful for a variety of medical applications including generating stimulus signals, monitoring, and communicating internal vital signs to the outer world. Providing power to the electronics, radio, and the stimulator/sensor of these devices is one of the major challenges in designing such systems [1]. Power requirements for these devices vary with application and can range from a few milliwatts to dozens of milliwatts. Supplying required power to biomedical devices in a reliable manner is of utmost importance [2]. The primary motivation of this thesis is to develop a system that will provide adequate power to these biomedical devices. For this research, we focus on using a wireless power transfer (WPT) technique based on magnetic resonant coupling.

There are different methods used for powering implantable biomedical devices. One method is to use transcutaneous wires to deliver power from an externally positioned battery or other power source to the implanted devices. However, the use of transcutaneous links across skin increases the risk of infection to the body/patients. Alternatively, batteries can be implanted along with a biosensor. However, these batteries provide limited energy storage and life span and may exceed size and mass requirements for the implantation in small animals. In addition, replacing the batteries is only performed by a surgical procedure, and long-term implantation introduces a potential risk of leakage. To reduce the risk of the possibility of infection by wires piercing the skin, wire breakage, and undesirable replacement and corrosion of embedded batteries, an alternative approach for providing power to the implantable devices is recommended. Another approach utilizes ambient energy sources, such as harvesting motion energy or capturing electromagnetic fields, to power biomedical devices. The generated power from these harvesters depends on the volume of the implanted device [1-7].

Biotelemetry systems are effective tools for clinical medicine and also in animal research, because they allow for the acquisition of otherwise unavailable physiological data [8-9]. Rodents are important animals for biomedical applications and tracking their movements is widely used to study various disease models. A vast majority of research on neural mechanisms of therapies is currently conducted using rodents [2]. Mice are used in such studies due to the availability of many different genetically modified lines that have been generated as models of human

disorders. Their small size presents a significant problem for the design and manufacturing of telemetry devices. These devices can be implanted subcutaneously or externally mounted to measure biophysical signals. Telemetric biosensors must be small, with a mass of a few grams and volumes of a few cubic centimeters, in order to provide monitoring without limiting mobility or behaviour of mice [1-2]. The main purpose of this work is to power the telemetric devices equipped with these biosensors, to transmit/record electrophysiological data of nerves or muscle tissue, or to provide stimulation.

1.2 General Literature Search for Energy Harvesting

Different energy harvesting approaches have been investigated to power the implantable biomedical devices in rodents. These approaches are thermoelectric energy harvesting, implantable glucose fuel cells, vibration-based energy harvesting, and WPT system.

Thermoelectric energy harvesting is based on the heat flux through a thermoelectric element or a thermos-generator comprising a multitude of such elements. The heat flux is driven by a temperature difference across the element. The generated voltage is proportional to the number of elements and the temperature difference. The thermal gradient provides an energy source which is extracted from the model body to generate electrical power via thermoelectric elements [10-11]. It is recommended that the room temperature range for rodent housing is between 20°C and 26°C, and significant fluctuations in temperature should be avoided [12]; therefore, the thermoelectric energy harvesting technique is not suitable for telemetric devices using rodents. Glucose is considered the most common substance for implantable fuel cells. Implantable fuel cell systems convert glucose into electricity via a spatially separated electrochemical reaction chamber [11]. Cinquin *et al*. developed a glucose bio-fuel cell implanted in rats which produced a peak specific power of 24.4 µW/mL [13]. It is obvious that these approaches of energy harvesting are inappropriate to provide suitable power (milliwatts) for the implantable biomedical device in rodents. Vibration-based energy harvesting and WPT techniques are investigated in this dissertation.

1.3 Proposed Thesis Scope

As such, a long-term powering scheme for telemetry electronics and radios is needed. In some applications, such as monitoring animal behaviour over long duration studies, embedded

batteries may be insufficient to provide the power needed to sample, record, and transmit large amounts of data. However, for rodent applications, battery replacement, size, and weight pose a problem for experiments of long durations. Powering the telemetric device for rodents using energy harvesting techniques (such as vibration and electromagnetic radiation) is preferred for long-term operation.

The major challenges of creating such devices for rodents are: (i) relatively small size, (ii) low frequency motion of rodents, and (iii) changing orientation of the rodent moving. Our proposal is to build a power system for telemetric devices used with rodents, which must be able to move freely inside their cages. We designed two different approaches for providing power to the devices; the first approach used vibration-based energy harvesting. Chapter 2 presents the initial work done involving design and simulation of a piezoelectric-based device to harvest the kinetic energy available from the natural movement of rodents. Ultimately, that approach was abandoned due to the low power available. Then we used the second approach: WPT based on magnetic resonant coupling.

1.4 Thesis Objectives and Contributions

The primary goal of the proposed thesis research is to develop a power system for telemetry devices that can be implanted subcutaneously in rats or head-mounted on mice. Initially, we considered various ways to power the biomedical implants. We initially investigated vibration-based energy harvesters utilizing piezoelectric materials. However, we found the achievable power of the piezoelectric energy harvesting device did not suit the application because it was too low. We then developed the WPT approach. The key objectives of this proposed thesis are:

(1) To provide enough power to the electronics, radio, and stimulators/sensors in telemetric devices for rodents.
(2) To achieve magnetic resonant coupling between the primary (transmitter) coil and the secondary (receiver) coil of a loosely coupled wireless power transfer (LCWPT) system.
(3) To design a measurement system to measure the received power of LCWPT systems while under test, and transmit the information wirelessly.
(4) To maintain the required power to the telemetry devices (stimulators/sensors) at different orientations when the small rodents move (their head tilts).

(5) To ensure that the maximum received power is achieved with the telemetry device, by using the matching impedance of the secondary circuit.
(6) To improve the efficiency by minimizing the power losses in the LCWPT system.
(7) To build an adjustable magnetic resonant system capable of tuning/detuning the WPT system, to be able to use multiple secondary coils (implants) in one primary (transmitter) coil.

More details for objectives (1-7) is as follows: Objective (1) is the main goal for the proposed thesis. For example, for an application with EEG sensing and stimulation, the power needed to start up the device is 51 mW for 100-300 milliseconds. After start-up, the system can run indefinitely with a power of 12 mW. The literature survey has shown that magnetic resonant coupling (objective (2)) is the most suitable approach for the LCWPT applications. This is accomplished by obtaining the same resonant frequency of the primary and secondary circuits [2]. For objective (3), we found traditional measurement techniques employing coaxial cables and voltage/current probes to measure power/efficiency of LCWPT systems are sensitive to electromagnetic interference, and produce poor results. We developed a custom wireless measurement system (WMS) to reduce measurement errors of the received power [2]. The rodent implanted with the telemetric device is moving and changing its orientation freely inside the cage (primary coil), so the secondary coil could lose coupling at high orientations (beyond 30°). Objective (4) reduces this problem through our design of a novel secondary coil configuration that employs ferrite rods placed at specific locations and orientation within the secondary coil [2]. The objectives (5&6) focus on minimizing the losses and maximizing the power transfer. The maximum power transferred by the secondary circuit occurs when the load is conjugately matched (such a load is called a matched load). The efficiency of the WPT system depends on many factors such as: the quality factor of the coils, the coupling coefficient, the separation and orientation between the coils, and the primary and secondary circuit topology. Objective (6) also focuses on improving the efficiency of the LCWPT systems, as summarized in Chapter 6. Objective (7) aims to expand the application by closed-loop control of the resonant frequency of the secondary circuit. This has useful application to power multiple implants (one per rodent) that are all in the same cage. When using multiple secondary coils within same cage, there is a mutual coupling effect between the coils, which leads to a mismatch of the magnetic resonant coupling between the secondary coils and the primary coil. It also has application for preventing

excessive heat build-up in the secondary circuit, in cases where high voltage may be induced within the secondary coil due to favourable orientations. This high temperature can cause over heating problems in the telemetric device. We refer this overheating problem as “electronic heating.” We designed a novel control scheme (objective 7) to tune/detune the LCWPT system for the multiple secondary coils (implants) within the same primary coil. The LCWPT system is a highly nonlinear dynamic system and has many variables. Our controllable WPT system is based on adjusting the magnetic resonance of the secondary circuits to meet the load requirements.

1.5 Thesis Organization

This thesis is divided into nine chapters as follows:

In Chapter 1, the motivation of this thesis presented the power requirements of telemetric biosensors for small rodents, and the different approaches used to power the implanted devices. The thesis objectives are also outlined in order to show the structure of this document and the contributions of this thesis are described. Chapter 2 presents the design and simulation of a piezoelectric-based device to generate electrical power by harvesting energy available from the natural movement of a mouse. The piezoelectric-based energy harvester is simulated using COMSOL, to predict the electrical power for different mouse motion excitation frequencies with the matched load impedance. Additionally, the actual data of mouse runs that is captured by an accelerometer is used to simulate its excitation to the proposed energy harvesting system. Chapter 3 describes the different WPT techniques for various applications used in the literature. The magnetic induction technique based on magnetic resonant coupling is suitable for powering biomedical applications. Mathematical equations of achieving the magnetic resonant coupling in the LCWPT systems are also illustrated in this Chapter. In Chapter 4, COMSOL is used to investigate the magnetic flux distribution surrounding four different secondary coil configurations. The simulation and experimental results showed the appropriate secondary coil configuration to provide the power requirement to the application device (EEG) while the rodents are moving freely inside the cage. In Chapter 5, the WMS is designed using Multisim simulation software. The physical prototype WMS is constructed to measure the received power by the secondary circuit wirelessly. In Chapter 6, different losses of the LCWPT systems are analyzed to maximize the total efficiency. The LCWPT system is redesigned and rebuilt to

minimize the losses and improve its total efficiency in Chapter 6. Chapter 7 describes the problems of using the multiple secondary coils in the WPT system. A literature survey of solving these problems is illustrated, and our new proposed controller system is designed to tune/detune the resonance of the secondary circuits in the LCWPT systems. Chapter 7 shows our design controllable LCWPT system for freely moving rodents. Chapter 8 provides a discussion of all the research presented in this thesis, as well as the features of our LCWPT system. In Chapter 9, conclusions are drawn concerning the results, the future potential, and the thesis contribution. These Chapters are then followed by the references used in this thesis.

Chapter 2: Piezoelectric Energy Harvesting

2.1 Introduction

Miniature portable sensors and telemetry systems can provide great advantage for monitoring animal behavior, physiological information and tracking. To operate remotely, such telemetry systems must have a suitable power source to carry out their task, for the longest possible duration. Often, these remote systems must operate wirelessly, since animal mobility and behavior can be adversely affected by wires and cable harnesses. A significant challenge for these devices is to provide a power source sufficient to meet the needs of the application. The process of gathering ambient energy surrounding a system, and converting it into usable electrical energy is termed as energy harvesting (EH) [14-15].

The energy gathered by EH devices can be used as the sole power supply for the device, to recharge on-board batteries, or to extend the life of a conventional battery. Of particular interest to our work is a device suitable for small rodents. Vibration-based energy harvesting is used in numerous applications ranging from biomedical devices, common household devices, transportation tools, industrial machinery, and even human motion [15]. Significant development in EH devices using mechanical vibration has taken place using various conversion mechanisms, including electromagnetic, electrostatic, and piezoelectric [16-18]. Table 1 provides a summary of various vibration-based EH techniques, which have been implemented using micro-electromechanical systems (MEMS) technology, and also lists the reported advantages and disadvantages of these techniques [19-34]. Techniques using piezoelectric EH have desirable features for this application, in particular: high energy density, high voltage developed, and small size with the ability to scavenge energy in the range of 1 to 375 $\mu W/cm^3$ [19-23]. For vibration-based EH, the optimal electrical power is achieved within a narrow frequency bandwidth, close to the resonant frequency of the device. The work of this Chapter shows the design and simulation of a piezoelectric-based energy harvesting device to provide power for miniature telemetry systems.

TABLE 1: SUMMARY OF VARIOUS EH SYSTEMS [19-34]

Ref.	Power (μW)	Freq. (Hz)	Vol. (mm^3)	Advantages:	Disadvantages:
			Piezoelectric EH		
[19]	2.1	80.1	125	- No external voltage source	- Depolarization
[20]	210	120	1000	- High output voltage	- Charge leakage
[21]	0.001	35	60	- Compact design using MEMS	- High output impedance
[22]	0.6	900	2	- High coupling in single crystals	
[23]	2.15	461.2	0.652		
			Electromagnetic EH		
[24]	0.3	4400	5.4	- No external voltage source	- Low mutual coupling factor
[25]	530	322	240	- Simple design	
[26]	180	322	840	- No smart materials.	
[27]	1.44	400	250		
[28]	10	64	1000		
[29]	830	110	1000		
			Electrostatic EH		
[30]	64	2520	75	- Simple design using MEMS	- External (charge) source is required
[31]	3.7	30	750	- No smart materials	
[32]	6	10	800		
[33]	70	50	32.4		
[34]	110	120	1000		

This Chapter involves the design and simulation of a vibration-based piezoelectric energy harvester for small animal motion (EHAM). A major challenge for this application is the relatively small size and low frequency motion of rodents. Rodents exhibit motion at low frequencies and small displacement amplitudes, where different gaits correspond to different frequencies [35]. Fig. 1 illustrates the proposed concept, where the EHAM design is mounted on a rodent. Of interest to this work are frequencies that correspond to typical (predominant)

behavior, such as running. An experiment is done to record mouse acceleration data while it is running, in three axes of motion. A power spectral density (PSD) is computed for all axes, to locate the highest observed power, its corresponding frequency, and the direction of that predominant rodent motion. Based on that information, the EHAM design has been developed, such that it operates at this predominant frequency to maximize the power harvested. Currently reported piezoelectric EHs in literature have been designed to typically operate at frequencies of 50 Hz, or higher. However, most animals exhibit typical motion at frequencies below 20 Hz, and there are no reported small-sized EH devices that operate below 36 Hz [15, 17].

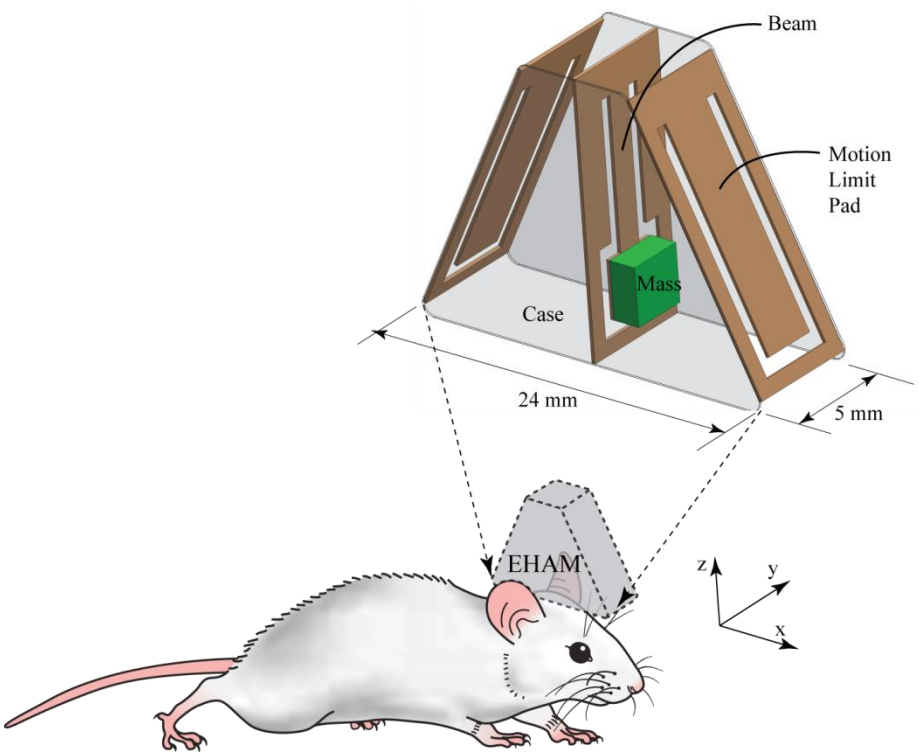

Figure 1: Illustration of energy harvester for rodent motion.

2.2 Model of Piezoelectric Energy Harvesting Device

A dynamic model of the proposed EHAM device is presented, along with the equations for the piezoelectric effect. This model is used to estimate the resonant frequency, the maximum theoretical power, and later the electrical impedance of the system. These are used to design the system, and are later compared to the finite element analysis (FEA) results. The EHAM can be approximated as a 1 degree-of-freedom (DOF) spring-mass-damper system, as illustrated in Fig. 2 [17]. This single DOF consists of a moving mass, *m*, connected to the base with a spring, *K*,

and damper, *C*. In addition, electric energy will be extracted from the oscillating system by the piezoelectric element, which is modeled as f_e in the diagram. The system of Fig. 2 is modeled as base-excitation, whereby the excitation acts on the housing (base) of the EHAM, as an acceleration $\ddot{X}(t)$. Accordingly, the EHAM is modeled as a second-order, spring-mass-damper system, as written in Eq. (1) [36]:

$$m\,\ddot{X}_1(t) + C\,\dot{X}_1(t) + K\,X_1(t) + f_e(t) = m\,\ddot{X}(t) \tag{1}$$

where, *m*, *C*, and *K* are the effective mass, mechanical damping, and stiffness, respectively; f_e is the effective force due to the piezoelectric element, and $X_1(t)$ is the mechanical displacement of the proof mass.

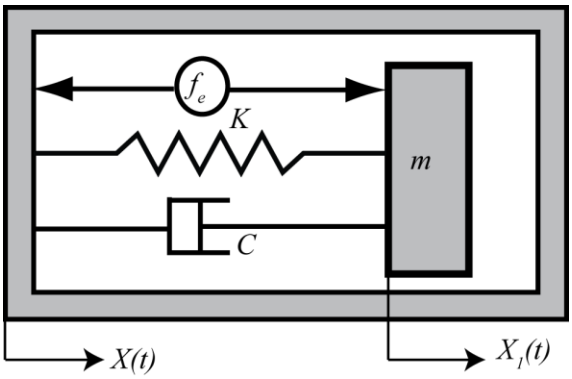

Figure 2: Model of single DOF vibration based energy harvester.

The piezoelectric effect occurs when certain crystalline materials are subjected to mechanical strain, causing them to become internally electrically polarized, where the degree of polarization is proportional to the applied strain. This phenomenon is known as the direct piezoelectric effect whereby the piezoelectric material generates an electric field across its volume. This electric field causes surface charge to accumulate on either side of the piezoelectric volume, which can be harvested with metal electrodes. The direct piezoelectric effect is described by [37-38]:

$$D_i = d_{ij}\,T_j + \varepsilon_{ik}E_k \tag{2}$$

where, *D*, *d*, *T*, ε and *E* are matrices representing the electrical displacement (polarization), strain piezoelectric coefficients, mechanical strain, material permittivity and the electric field, respectively. The subscripts i = 1, 2, 3; k = 1, 2, 3; and j = 1, 2, 3, 4, 5, 6 denote the direction to which physical properties are related, where 1, 2 and 3 correspond to the directions *x*, *y* and *z*,

respectively. For instance, d_{ij} is the piezoelectric coefficient that describes the charge collected in the plane perpendicular to the *i*-direction due to applied strain in the *j*-direction [38].

Piezoelectric materials are widely available in many forms including single crystal (e.g. quartz), polycrystalline piezoceramics (e.g. lead zirconate titanate (PZT)), thin films, screen printable thick-films based upon piezoceramic powders, and polymeric materials (e.g. polyvinylidene fluoride (PVDF)). Piezoelectric materials typically exhibit anisotropic characteristics, thus, the properties of the material differ depending upon the direction of applied forces, and the orientation of material polarization. Sodano *et al*. investigated and experimentally tested three types of piezoelectric devices including PZT, quick pack (QP) and macro fiber composite (MFC). Their work confirmed that PZT is highly effective in random vibration environments, which is usually encountered when dealing with vibration-based EH [39]. Using equation (1) for the EHAM; the effective transducer force f_e can be presented as [36]:

$$f_e = k_m V_P(t) \tag{3}$$

$$k_m X_1(t) - C_P V_P(t) = Q_p(t) \tag{4}$$

where, k_m is the effective electromechanical coupling coefficient of a piezoelectric structure, $V_p(t)$ is the voltage across the piezoelectric electrodes, $Q_p(t)$ is the charge generated on the electrodes, and C_p is the capacitance of the piezoelectric material. For the model of Fig. 2, the average power dissipated within the damper, P_{av}, (i.e. the power extracted by the transduction mechanism plus the power lost through parasitic damping mechanisms) is given by [17]:

$$P_{av} = \frac{m \zeta_T Y^2 \left(\frac{w}{w_n}\right)^3 w^3}{\left[1 - \left(\frac{w}{w_n}\right)^2\right] + \left[2\left(\frac{w}{w_n}\right)\zeta_T\right]} \tag{5}$$

where, ζ_T is the total damping ratio given by $\zeta_T = C/2mw_n$, Y is the amplitude of the applied external vibration, w is the frequency of the applied excitation, and ω_n is the natural frequency of the system. This equation is valid for steady state conditions, where the average power (P_{av}) is equal to the kinetic energy supplied per second, due to vibration. Note that maximum power occurs when the device is excited at an applied frequency of ω_n (i.e. $\omega = \omega_n$), which can be expressed as [17]:

$$P_{av(max)} = \frac{mY^2 \, {w_n}^3}{4\zeta_T} \tag{6}$$

The maximum power that can be extracted by the transduction mechanism, including the parasitic and transducer damping ratios, is calculated as [17]:

$$P_e = \frac{m\zeta_E Y^2 \, {w_n}^3}{4(\zeta_P + \zeta_E)^2} \tag{7}$$

P_e is maximized when the electrical damping ratio equals the mechanical damping ratio ($\zeta_E = \zeta_P$) [17].

2.3 Collection of Mouse Gait Acceleration Data

An experiment to collect motion data of mice has been conducted. This data is used to determine the predominant (most frequently occurring) frequencies of motion during running. As well, it is later used as input for a FEA simulation of the EHAM, to predict its performance given real mouse motion. This allowed for the EHAM to be designed by adjustment of parameters, and evaluation of the simulation results. Fig. 3 shows the experimental setup to measure motion, which uses a three-axis accelerometer (PMU-9150) attached to the mouse head to measure the acceleration while the mouse runs on a wheel. This measurement system consists of a battery, accelerometer, circuit board and attachment hardware, where the total weight is 4.40 grams. Such a battery-based system is used for other types of short-term data acquisition, and the size and mass is well tolerated by the rodent.

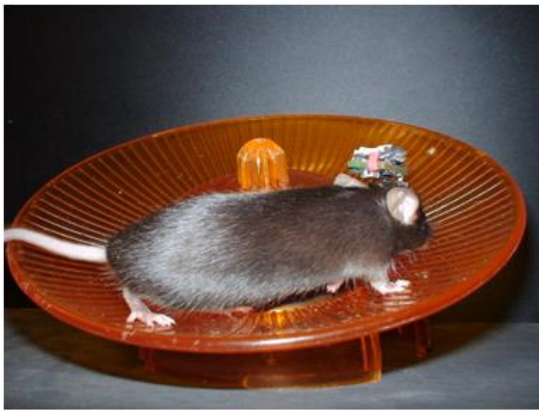

Figure 3: Experimental setup for measuring the acceleration of mouse gait.

Acceleration is measured in three axes, where the *x*-axis corresponds to front/back motion, the *y*-axis to right/left motion, and the *z*-axis to up/down motion. The range setting of the accelerometer is $\pm$4g (m/s^2) and the sampling frequency is 200 Hz, as defined by the onboard microcontroller. A sample of *x*-axis acceleration data obtained while the mouse is running for 11 seconds is shown in Fig. 4. By creating a PSD of all three axes of the acceleration data, the predominant frequencies of motion along with their relative power can be identified. Fig. 5 shows the PSD plots for the *x*, *y* and *z* axes. It was found that the predominate frequency and motion amplitude occurred along the anterior-posterior axis of the mouse, which corresponds approximately to the *x*-axis of the EHAM, as shown in Fig. 1. Due to difficulty in mounting the measurement device to the mouse, there was a difference of approximately 20-30 degrees between the angle of the *x* and *z* axes, as evidenced by the *x*-axis offset seen in Fig. 4. As a consequence, power is observed in both the *x*-axis and *z*-axis, in the PSD plot at similar frequencies, as seen in Fig. 5. There are a number of resonant frequencies apparent in Fig. 5, corresponding to peaks of power, however, the major resonant frequency is found at 11.7 Hz.

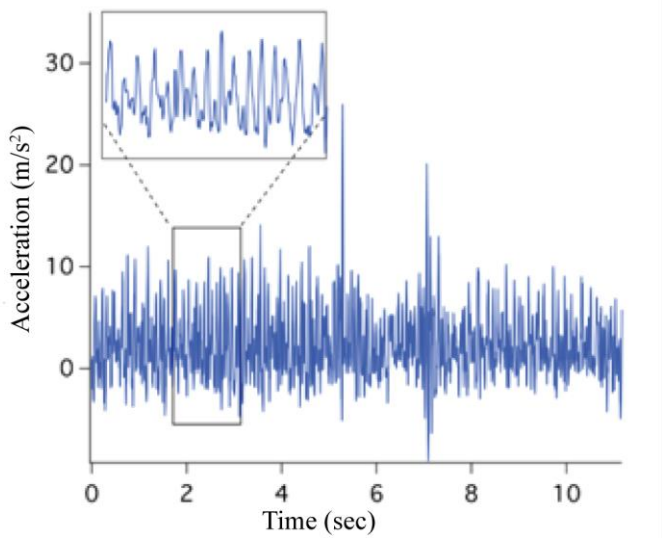

Figure 4: Acceleration recorded in the *x*-axis during mouse gait.

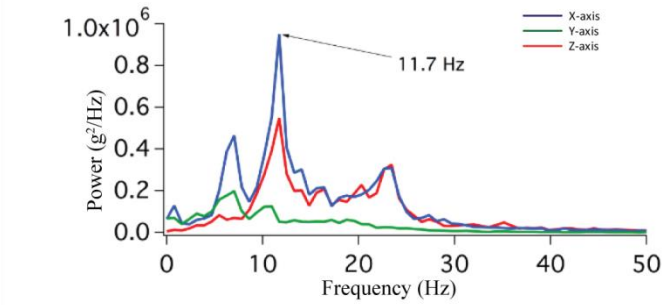

Figure 5: PSD plot of the *x*, *y* and *z* axis acceleration measurements during mouse gait.

2.4 Design of the EHAM

The motivation of the EHAM design is to convert mouse motion energy into electrical power. Given this goal, a set of design requirements for the EHAM device are established, and summarized in Table 2.

TABLE 2: DESIGN REQUIREMENTS FOR THE EHAM SYSTEM

Design Requirement	Description	Target Value [units]
Operating Frequency	Predominant gait frequency of mouse	11.7 [Hz]
Total volume	Maximum volume of EHAM tolerated by mouse	2000 [mm^3]
Proof Mass	Maximum moving mass tolerated by mouse during regular activity	1 [g]
Amplitude (d_0)	Maximum amplitude of moving mass, tolerated by mouse	1.5 [mm]
Stress in Beam	Maximum allowable stress of oscillating beam material. To be less than 30% of ultimate strength, to avoid fatigue damage.	600 [MPa]
Power Output	Maximize power given design requirements	Max. [Watts]

Creating a design to meet these requirements was challenging. Several design iterations were done whereby the design was simulated with FEA, the results analyzed and the design parameters adjusted. The cantilever-beam structure with proof-mass was found to be the simplest oscillator design that could meet the objectives for the EHAM. A cross-sectional diagram of the proposed configuration is illustrated in Fig. 6 (not to scale). Given the requirement for low frequency operation at 11.7 Hz, a combination of high proof-mass weight and low beam stiffness is used. It was determined that a silicon-based cantilever beam with a PZT layer is best able to

provide low beam stiffness, and yet is strong enough to prevent breakage of the structure given the loading produced by mouse motion. Some suggestions [15, 18, 40] were used when designing with the aim of getting a low natural frequency with maximum power generation. These included a longer beam length *L*, shorter beam width *W*, and lower ratio of piezoelectric layer thickness to beam thickness.

To minimize the volume of the proof-mass, tungsten material is selected due to its high density and relative abundance. By placing the proof-mass near the tip of the cantilever beam, and increasing the beam length, the structure's natural frequency ($w = \sqrt{k_{mat}/m}$, where k_{mat} is the material stiffness and *m* is the mass) decreases. However, this also results in increasing the stress at the root of the cantilever, resulting in a design compromise between low frequency operation and beam strength. A unimorph cantilever configuration (structural layer plus piezoelectric layer) is chosen over that of a bimorph configuration (structural layer plus upper and lower piezoelectric layers), since the unimorph is more suitable for lower frequencies and load impedances [15, 17]. Given that the ultimate strength of crystalline silicon is approximately 2 GPa, the maximum allowable stress of 600 MPa was chosen as a design requirement to avoid fatigue damage to the beam. Given several design iterations, the final design parameters of the EHAM are listed in Table 3.

TABLE 3: FINAL DESIGN PARAMETERS FOR THE EHAM

Design Parameter	Description:	Design Value [units]
Overall EHAM Case Size	Size of packaged EHAM [$L \times W \times H$]	$17 \times 5 \times 24$[mm]
Beam Geometry	Material: Crystalline silicon [$L \times W \times H$]	$15 \times 2 \times 0.05$ [mm]
PZT layer Geometry	Material: PZT-5 [$L \times W \times H$]	$15 \times 2 \times 0.005$ [mm]
Mass Geometry	Material: Tungsten [$L \times W \times H$]	$5 \times 4 \times 2.4$ [mm]
Operating Frequency	Natural Frequency of structure	11.7 [Hz]
Proof mass	Weight of proof tungsten mass	0.9 [g]

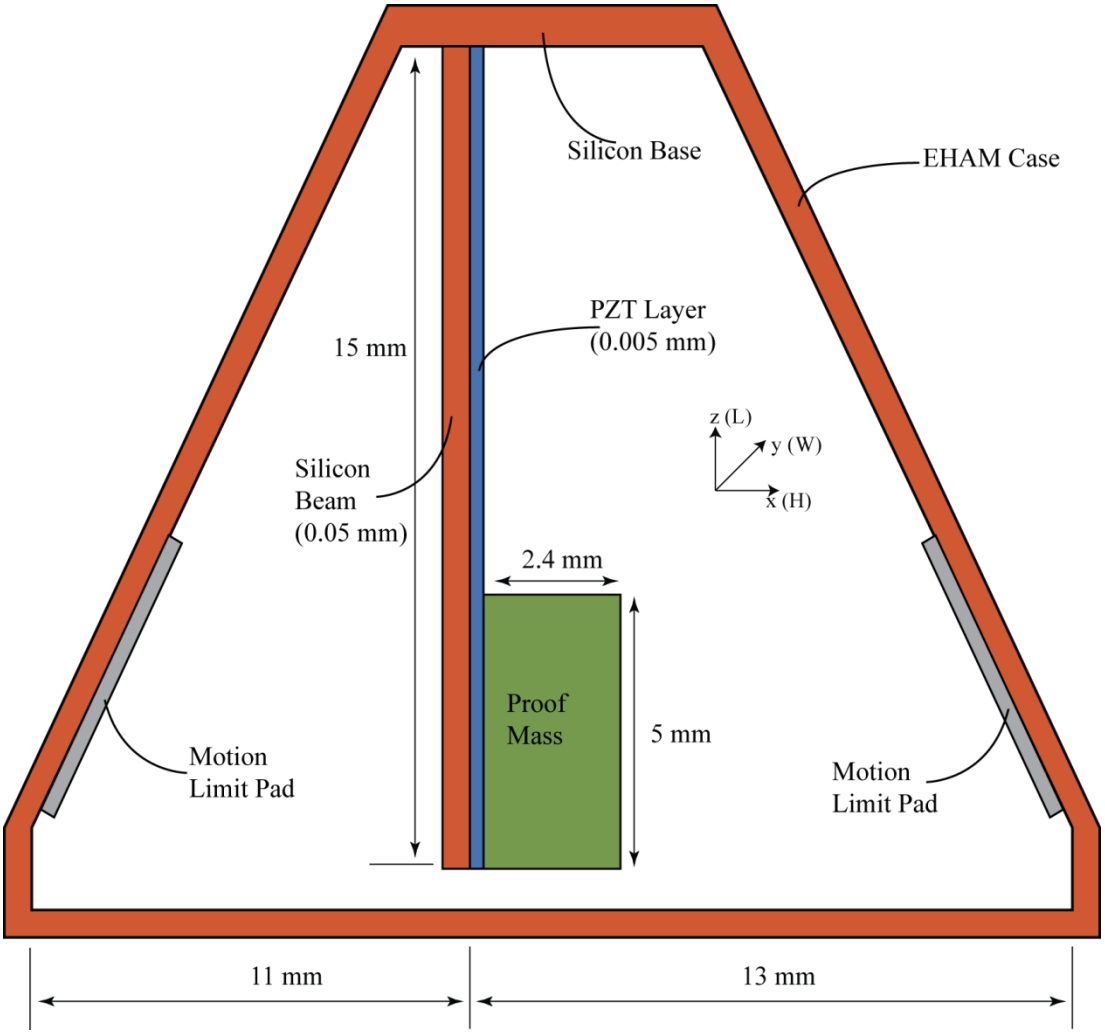

Figure 6: Illustration of dimensions for final design of EHAM cantilever (not to scale).

2.5 Simulation of Model Performance

A series of computer models were developed to simulate the performance of the EHAM design as shown in Fig. 6. The simulation is done with COMSOL, a commercial FEA package for finding the approximate solution of partial differential equations where the domain boundaries of a given problem are complex. Further, the model is multi-physics, combining the structural mechanics aspects, the piezoelectric electrical aspects, and a simulated electrical load for the model. Given the constant geometry of the design in the *y*-direction as per Fig. 6, the model is simulated with 2-D (two-dimensional) analysis. One challenging aspect of the FEA simulation is the considerable differences in the size between various parts, or in the parts themselves. This is a common problem when simulating MEMS devices, known as multi-scale FEA [15]. In this case, the piezoelectric layer is only 0.005 mm thick, yet 15 mm long, and the

mass is much larger than the beam thickness. Hence, creating a FEA mesh for such geometries is not a trivial task. In order to guarantee mesh integrity, the aspect ratio of individual mesh elements should not be greater than three [18], and hence necessitates a large number of elements for structures with considerable size differences. The model solution convergence strongly depends on the quality of the mesh elements, and computation time depends on the number of elements. Our approach was to use structured meshes or mapped meshes. The most significant drawback of using the default free meshing in thin material layers is that the number of elements increases significantly, since the meshing algorithm builds elements with individual aspect ratios that are close to unity [15, 18].

In the EHAM simulation the meshing parameters are configured for each part (piezoelectric layer, silicon beam, and tungsten mass) separately. A *Free Triangular* mesh type is used for the piezoelectric layer (PZT-5A) using the *Coarse* mesh setting. A *Free Quad* mesh and a *Mapped* mesh are used for the silicon beam and tungsten mass respectively. An *Extremely Fine* mesh setting is used for both the silicon beam and tungsten mass. In order to improve the mesh quality, a *Refine Distribution* function is applied at the root (fixed constraint) of the silicon beam, to force the mesh into approximately square elements, and hence limit the aspect ratio to about one. Fig. 7 (a) illustrates the overall of EHAM meshing, and a close-up of the transition of the mesh between the silicon beam, the piezoelectric layer, and the proof-mass. The model mesh consisted of a total of 38,360 elements, and internal mesh quality analysis showed the mesh to be of high quality, as shown in Fig 7 (b).

The base excitation is modeled using a *Roller constraint* in COMSOL. Using the developed FEA model, four different studies are done to investigate the performance: (1) An *Eigenfrequency Study* to determine the first eigenfrequency (natural frequency) and its mode shape; (2) A *Stationary Study* to check the total displacement and corresponding stress within the beam due to gravity alone, and also at the limit pad positions; (3) A *Time Dependent Study* (transient response analysis) to simulate the performance (displacement, stress and electrical properties) of the model when a range of sinusoidal excitation frequencies are applied; (4) An additional *Time Dependent Study* to simulate the EHAM performance when mouse gait displacement data is used as excitation for the model.

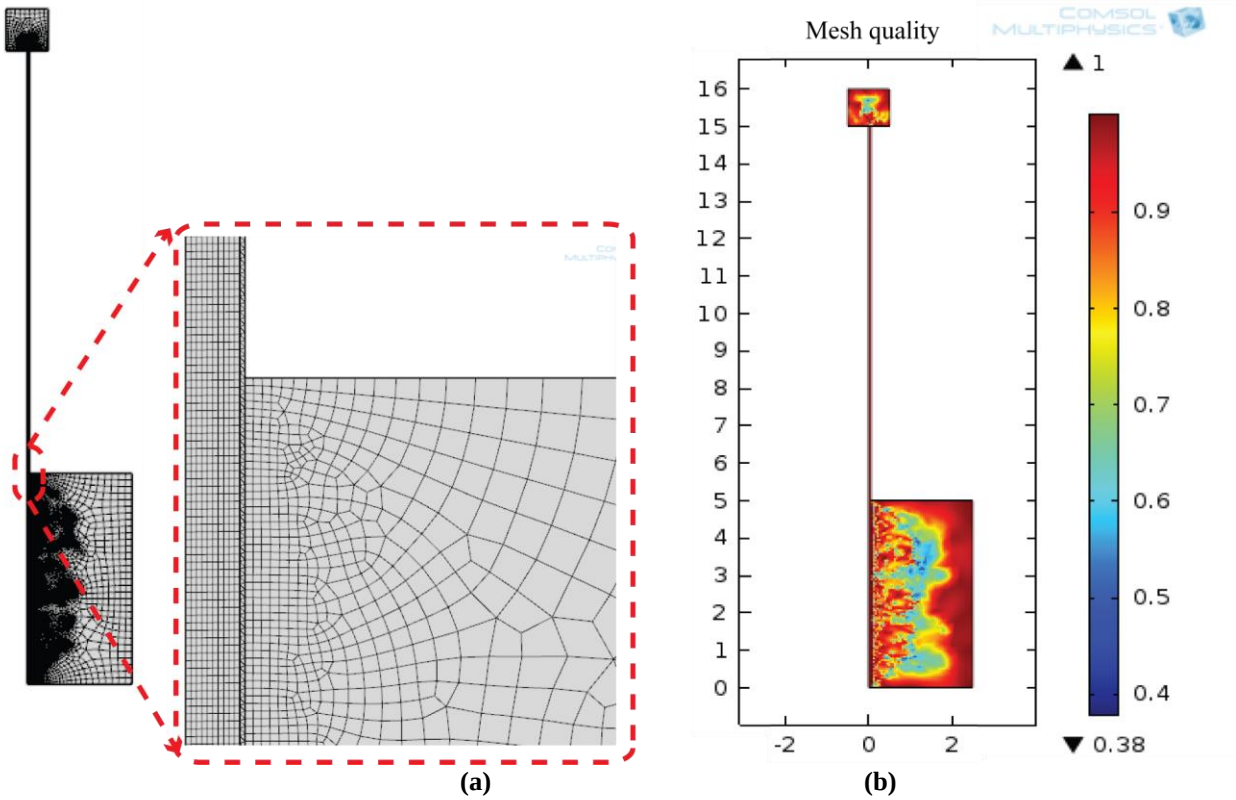

(a) (b)

Figure 7: Illustration of FEA element mesh used for EHAM; (a) meshing with close-up of transition from beam into proof-mass, (b) mesh quality.

2.5.1 Eigenfrequency Study

The EHAM model is analyzed to determine its resonant frequencies using FEA to find the eigenfrequencies and mode shapes of the structure. This analysis is extensively used during the geometrical design of the EHAM. The first three eigenfrequencies of the EHAM (*x*-*z* plane of Fig. 6) are found to be: 11.7, 136.3, and 3616.6 Hz. The eigenfrequencies (*f*) in the structural mechanics field are related to the eigenvalues, λ_{eig}, returned by the solvers through:

$$f = \frac{\sqrt{\lambda_{eig}}}{2\pi} \tag{8}$$

2.5.2 Stationary Study

A static response FEA analysis is done to determine the displacement and stress of the EHAM, for its limiting conditions. This occurs for the nominal case where gravity alone acts on the mass, and also if the EHAM comes into contact with the motion limit pads (Fig. 6), due to excessive acceleration loads. The EHAM is investigated for the static response (gravity alone) using the

gravity function in COMSOL. The maximum displacement is due to gravity is 0.34 mm, as shown in Fig 8 (a). This would correspond to the case where the mouse is at rest, with gravity acting in the -L direction. At this position the maximum Von Mises stress is found to be 10 MPa near the root of the beam, as shown in Fig. 8 (b). In the limiting position when touching the motion limit pads, the maximum stress at the root of the beam was found to be 430 MPa.

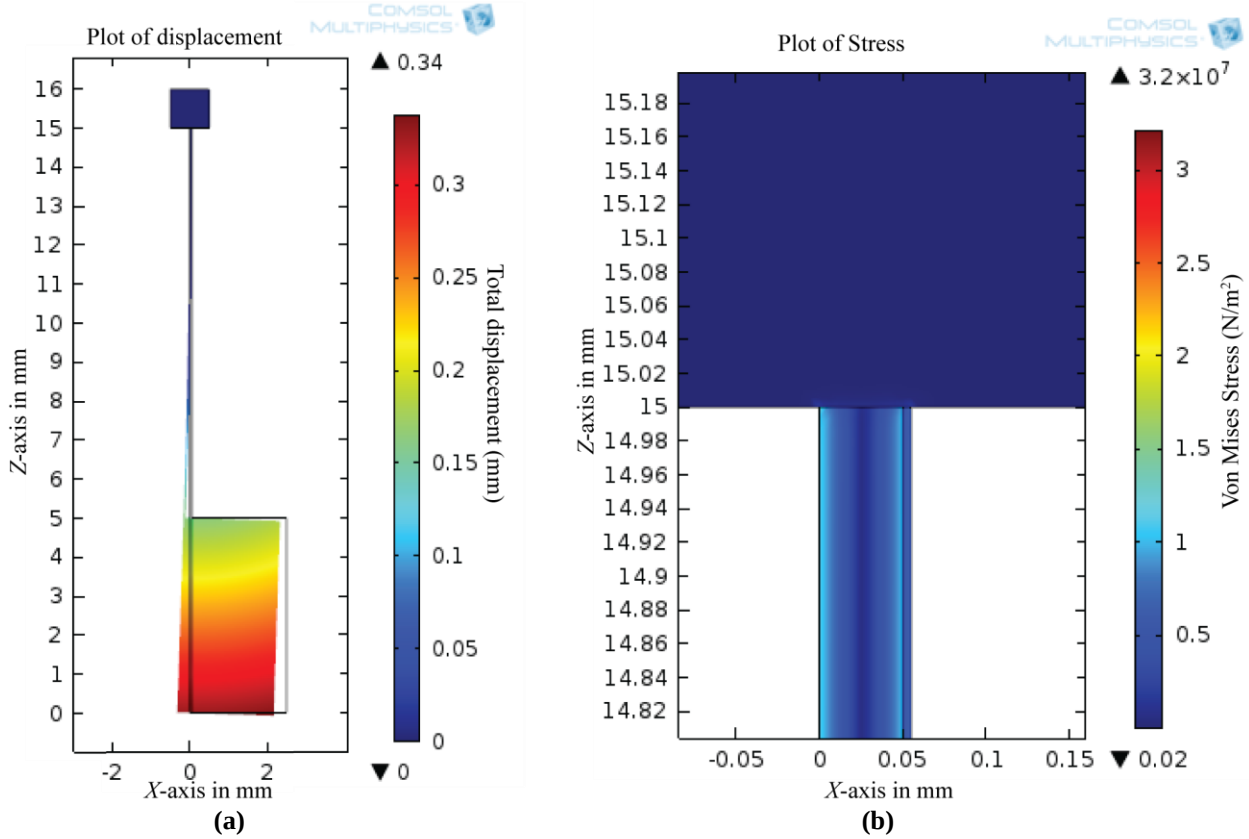

Figure 8: Simulation results of *Stationary study*; (a) total displacement, (b) Stress at the root.

2.5.3 Transient Study (Sine wave excitation)

In this study, a simulation of the oscillatory response of the EHAM is done. Here, the EHAM model is subjected to sinusoidal excitation at several specific frequencies. The resulting amplitude of its steady state response and the time to reach that response is determined. The simulations are done with a transient (time domain) FEA study where a four-second response is computed, using a time step of 0.002 seconds. The four-second duration was used to allow the model response to transition from a motionless state, to an oscillatory steady state for most configurations. For example, Fig. 12 shows the four-second result for one such transient study where the EHAM is excited at the resonant frequency of 11.7 Hz. In addition to this, it is of

interest to observe the EHAM response to other frequencies. For this, simulations are done with excitation frequencies in the range of 9 Hz to 13 Hz, using steps of 0.2 Hz. The oscillatory steady state response is also dependent on the system damping. Damping has been added to the simulation to model the effects of energy dissipation (loss) within the EHAM. There are four possible types of damping effects that can influence the behavior of cantilever-based energy harvesters [41]. These damping effects include: airflow force, squeeze force, internal friction, and support loss. For the proposed EHAM, the airflow damping ratio has been applied, while the other damping effects are small values that can be neglected, as computed in Table 4.

TABLE 4: DAMPING RATIO CALCULATIONS FOR THE PROPOSED EHAM, BASED ON [41]

Damping type	Equation		Value for silicon beam
Airflow	$\zeta = \frac{3\pi\mu_a b + 0.75\,(\pi b^2\,(2\rho_a \mu w_n)^2)}{2\rho_m h w_n b^2}$	(9)	0.062
Squeeze force	$\zeta = \frac{\mu b^2}{2\rho_m h g^3 w_n}$	(10)	2.34×10^{-8}
Internal friction	$\zeta = \tau/2$	(11)	1×10^{-6}
Support loss	$\zeta = \frac{0.23\,h^3}{l^3}$	(12)	8.518×10^{-9}

In Table 4, the variables are defined as follows: μ_a and ρ_a are viscosity (1×10^{-4} Pa·s) and density (1.3 kg·m^{-3}) of air respectively, τ is the structural damping coefficient, g is the gap distance (10 mm), b, h and ρ_m are the width, height and density of the silicon beam.

The Rayleigh damping model is used in the COMSOL setup to configure the damping ratio. The two major materials of the cantilever are calculated separately for internal friction (silicon beam and the PZT layer), while the other effects are geometrically based. The values summarized in Table 4 are calculated for the silicon beam, and the Rayleigh damping coefficients used in COMSOL are configured as [18]:

$$\alpha = 0 \text{ and } \beta = \frac{\zeta}{\pi f} \tag{13}$$

where, the values for β, for the silicon beam, and the PZT, are 1.7×10^{-3} and 4×10^{-3}, respectively.

The nature (magnitude and frequency) of the excitation force applied to the EHAM is important, since it determines the maximum displacement of the EHAM proof mass and the corresponding power generation. For this application, the proposed application requires mounting on the head of the mouse, as illustrated in Fig. 1. Mouse motion is multi-frequency, chaotic, and varies based on behavioral factors. Further, the mouse is not a single rigid body, but

can be considered as several connected masses, each of which are moving at different frequencies and amplitudes of acceleration. For this reason, the experiment described in Section 2.3 is conducted to collect acceleration data of the mouse motion in three axes. From this data, a PSD was created which shows a distribution of animal power available at different frequencies, as shown in Fig. 5. It is noted that the highest power occurs with motion in the *x*-axis (forward/backward) at 11.7 Hz, which has been chosen as the operating frequency for the EHAM.

In the sine wave excitation simulation, the excitation displacement, $X(t)$, is applied in the *x*-axis. For simulation at the operating frequency (*f*), the predominant excitation frequency found from the *x*-axis mouse motion is used, as shown in Fig. 5. Although there is a component of motion in the *z*-axis, only the *x*-axis motion will be considered, to be conservative in the estimation of generated power. It is likely that there will always be some misalignment when mounting the EHAM to a mouse. Another important question is the magnitude of the exciting displacement $X(t)$ of the base excitation model, as shown in Fig. 2. We excited our EHAM by 1.25 mm amplitude displacement (d_0). Therefore, the excitation displacement $X(t)$ used in our simulation is determined using equation (14).

$$X(t) = d_0 \cdot sin(2\pi f t) \tag{14}$$

Fig. 9 shows the maximum displacement result during the *Transient Study* (*sine wave excitation*) at the resonant frequency of 11.7 Hz, which is about 10 mm. In this position, the proof mass would be located mid-way between the right and left motion limit pads. Another important aspect of the simulation is the electrical configuration of the piezoelectric material, the generation of electric potential, and the resulting current flow through an application circuit. Here the application circuit is modeled as a simple resistive load of value R_L. The value used for R_L can be optimized for an ideal value, and will be described in Section 2.6. The general equation for the electrical output (power dissipation across load resistor R_L) for the piezoelectric energy harvester, is given by:

$$P_R(t) = I_R(t) \cdot V_R(t) \tag{15}$$

For the configuration where a piezoelectric is connected with a R_L in parallel, the relationship between the output of the piezoelectric EH and the input to the resistive load are [36]:

$$I_R(t) = w \cdot Q_P(t) \qquad (16)$$
$$V_P(t) = V_R(t)$$

where, $I_R(t)$ and $V_R(t)$ are the current and the voltage of the load.

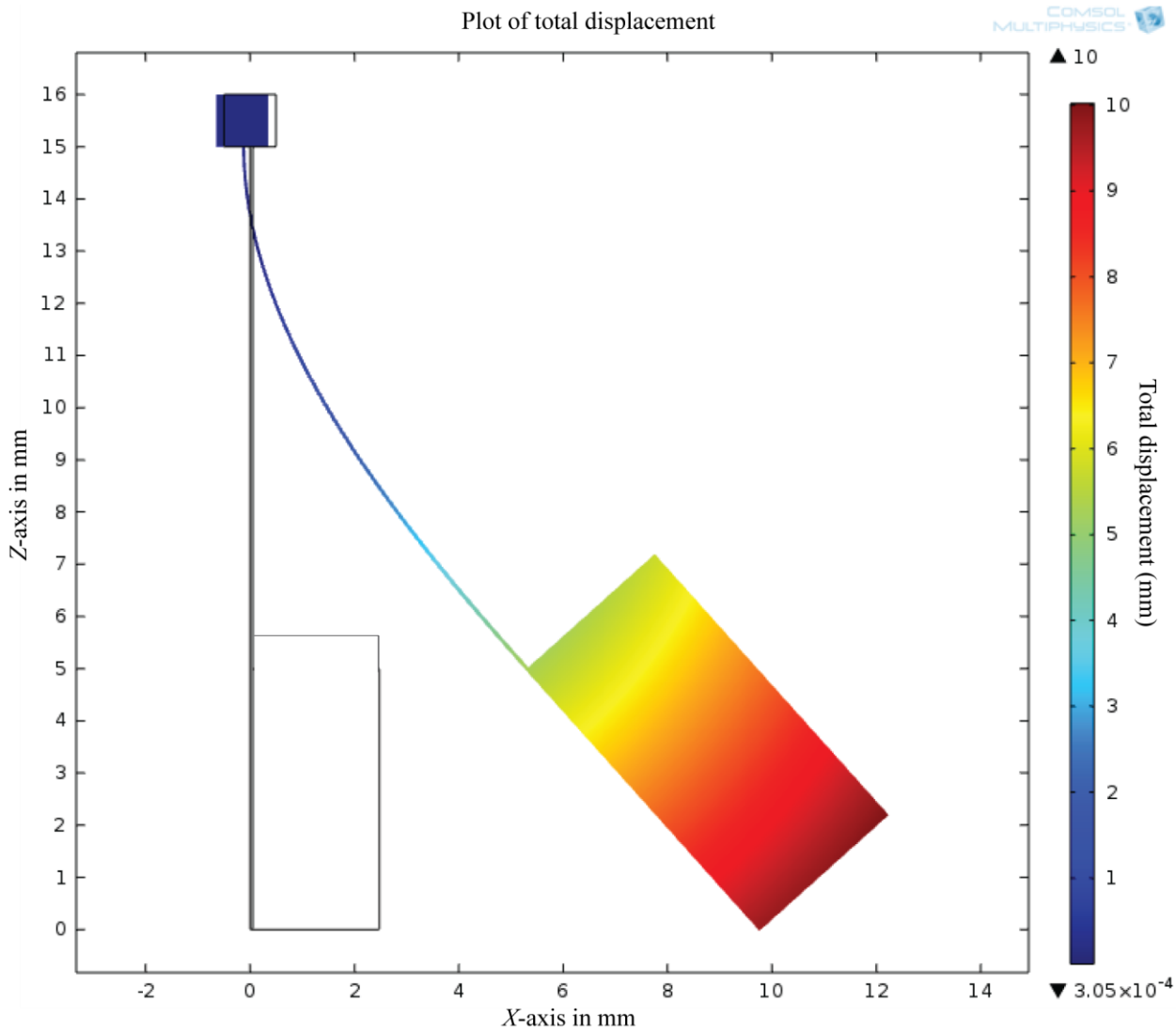

Figure 9: Total displacement in the *Transient Study*.

From the derived equations, it is observed that $X_1(t)$, $V_R(t)$, and $I_R(t)$ are coupled together through R_L and k_m. This means that $X_1(t)$, $V_R(t)$, and $I_R(t)$ are all affected by R_L and k_m. In the simulation, the circuit is configured by specifying the electrodes on the piezoelectric layers, and connecting them to a resistive load. In COMSOL, this is done by configuring a *Ground* and *Terminal (circuit)* on the PZT layer, using a resistive load with *Electrical Circuit Physics*.

2.5.4 Transient Study (Arbitrary waveform excitation)

In this section, the actual acceleration data from a mouse during running was imported in COMSOL to excite the EHAM. However, the simulation results (displacement, voltage) of the EHAM had accumulation error and did not follow the pattern of the excitation actual acceleration data, as the tip displacement of the cantilever was increasing. Since the basic partial differential equations of the FEA are based on the force and the displacement [42], the EHAM should be excited by the displacement. Therefore, the actual acceleration data was integrated twice, to get the displacement of the mouse head while the mouse was running. We removed the random errors and the noise from the acceleration data during the integration using "moving average curve" technique [15, 18].

A sample of *x*-axis acceleration data is used to obtain the actual displacement. The accelerometer hardware sampling time for the actual acceleration data is 0.005 seconds. For the simulation, we interpolated that data 5× to a time step of 0.001 seconds, as shown in Fig. 10 (a). We found that the larger sample size of the moving average curve technique, the less error is obtained in the integration [15]. We used 500 and 1000 sample sizes to obtain the velocity and the displacement, as shown in Fig. 10 (b and c). The actual displacement that is shown in Fig. 10 (c) was imported in COMSOL to excite the EHAM. Fig. 15 (a) shows the *x*-component displacement result when exciting the EHAM with actual displacement data. It is noticed that the maximum displacement is 10 mm, so the proposed cantilever will not hit the motion limit pads of the EHAM, as shown in Fig. 6. The harvested power (P_{RMS}) from exciting the EHAM with the actual displacement data (using a matched impedance load) is 37.5 µW.

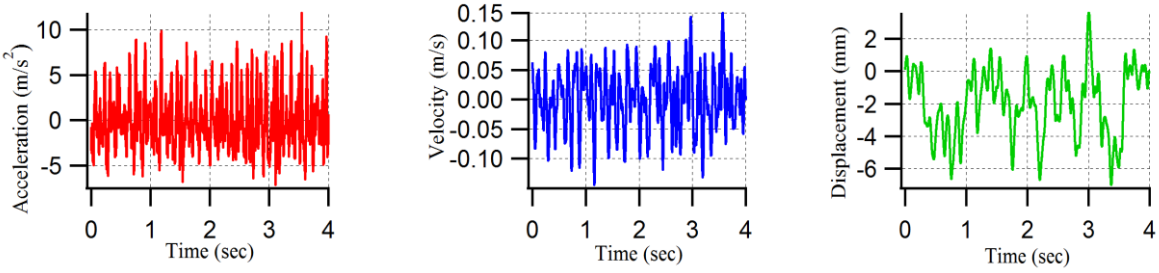

(a) **(b)** **(c)**

Figure 10: Actual data (*x*-axis) of mouse head movement (running); (a) acceleration, (b) velocity, (c) displacement.

2.6 Results and Discussion

The simulation results of the proposed EHAM design are analyzed and discussed. The response of the EHAM to various excitation frequencies is done with an extensive simulation, consisting of a transient study performed for each excitation frequency between 9 Hz to 13 Hz, in 0.2 Hz increments. This is accomplished using the *Parametric Sweep* function within COMSOL. Additionally, the electrical power generated by the piezoelectric layer of the EHAM is analyzed for the same range of applied excitation frequencies. When considering the electrical power output of the piezoelectric layer, the value of the application circuit load R_L, is important. The circuit load represents the impedance of the application circuit that would be powered by the energy harvester, and its value will vary depending on the nature of the application. For any piezoelectric-based harvester system, there is inherent impedance R_{piezo}, which can be calculated. This inherent impedance must be matched to the impedance of the proposed application circuit load, to maximize the output power. The inherent impedance R_{piezo} can be computed as follows: the piezoelectric layer acts as capacitor, so the capacitive impedance of the piezoelectric layer is given by [17]:

$$R_{matched} = \frac{1}{2\pi f_{res} C_{pzt}} \tag{17}$$

where, C_{pzt} is the capacitance of the piezoelectric layers, and f_{res} is the resonant frequency of the EHAM device. The capacitance of the piezoelectric material depends on the layer dimensions, including in-plane area and thickness, and is given by:

$$C_p = \frac{\varepsilon_r \varepsilon_o \, W_{pzt} \, L_{pzt}}{H_{pzt}} \tag{18}$$

where, W_{pzt} is the piezoelectric layer width, L_{pzt} is the piezoelectric layer length, H_{pzt} is the piezoelectric layer thickness, ε_o is the electrical permittivity of free space, and ε_r is the relative dielectric constant of the piezoelectric layer. For the EHAM, these values are W_{pzt} = 2 mm, L_{pzt} = 15 mm, H_{pzt} = 0.005 mm, and ε_r = 1730. Therefore, the inherent impedance, R_{piezo}, for the proposed EHAM is 222 kΩ. Given this value for the inherent impedance, we know that the application circuit load R_L must be equal. Hence, the application circuit load must consist of both the application circuit and with the buffer energy cells, along with their charge/discharge circuit.

Given the value for R_{piezo}, can now proceed to compute the power over a range of applied frequencies. The RMS electrical power value is calculated by:

$$P_{RMS} = \sqrt{mean\,(P_f{}^2)} \tag{19}$$

where, P_f is the electrical power values over the period at the applied frequency (f).

The performance of the EHAM is simulated with a resistive load R_L (matched to load R_{Piezo}) of 222 kΩ, and the excitation force of equation (14). Fig. 11 illustrates a plot of the electrical power (P_{RMS}) produced, over a range of excitation frequencies from 9 Hz to 13 Hz, in 0.2 Hz increments, with sampling time 0.002. It is noteworthy to observe that the maximum power is computed to occur at 11.7 Hz, which corresponds to the frequency at which maximum displacement of the cantilever occurs. This verifies the earlier eigenfrequency result of Section 2.5.1, which predicted the first resonant mode to occur at 11.7 Hz.

The transient results for displacement of the cantilever tip is plotted in Fig. 12 for the single-frequency case of excitation at 11.7 Hz, with R_L = 222 kΩ. These tip displacement values are used to verify the operational volume of the EHAM cantilever beam with proof mass, where the maximum displacement is ± 10 mm. Therefore, the proposed configuration of the EHAM illustrated in Fig. 6 shows a 11-13 mm clearance on either side of the beam. Beyond this range, two motion limit pads (right and left) as shown in Fig. 6, must be used to protect the cantilever beam in the event of an applied displacement that exceeds $X(t)$, such as an unexpected large acceleration or shock. As a point of interest, the theoretical equation (1) does not study the limit stop effect in the EHAM design. If such an event occurs, the mass will make contact with the motion limits, which will damp out the energy, and protect the beam from excessive deformation and stress, as shown in Fig. 13. The maximum stress at the root of the beam is determined to be 0.53 GPa.

Upon reviewing the PSD plot in Fig. 5, it is observed that there are three effective peaks at 7 Hz, 11.7 Hz and 20 Hz. As a point of interest, the EHAM is simulated with these two additional frequencies of 7 Hz, and 20 Hz. For each of these cases, the resulting displacement was 0.5 mm, and 0.25 mm, respectively. Therefore, these frequencies were ignored, and only 11.7 Hz was considered.

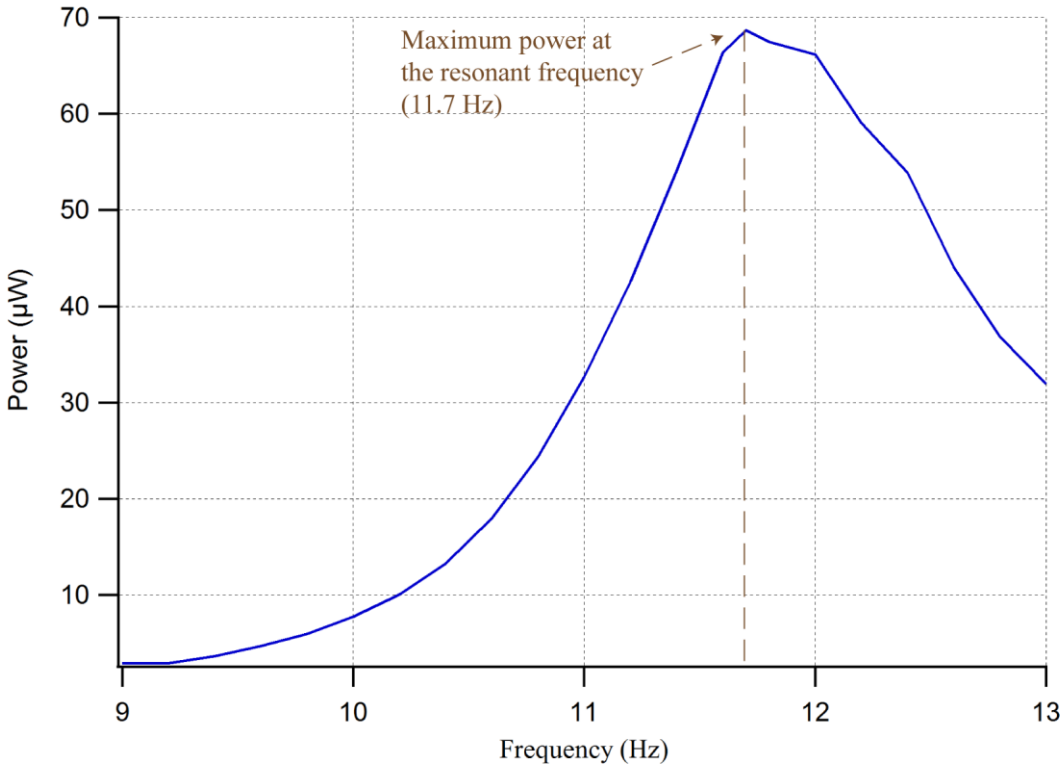

Figure 11: Plot of electrical power versus excitation frequency, with R_L =222 kΩ.

The importance of impedance matching between the EHAM and the application circuit load, R_L, is now described. Fig. 14 shows a plot of the electrical output power from the EHAM, versus different (non-ideal) circuit resistive loads, over a range of excitation frequencies. Different resistive loads are illustrated with different colored lines, which represents the RMS electrical power over a period of four seconds for different resistive loads (1, 100, 1000 and 222 kΩ). Table 5 shows the maximum displacement achieved at steady state. These simulation results confirm that the maximum output power is obtained when the impedance computed from equation (17) is used as the matched application load resistance.

Fig. 14 shows that the maximum electrical power generated from the EHAM is obtained with the matched resistance load. The best case for maximum power would occur with constant excitation at 11.7 Hz, which would provide continuous power predicted to be 68 μW. However, since mouse motion at this frequency is intermittent, the resulting average power would be lower. It is noticed that the maximum tip displacement of the beam is highest at the resonant frequency (11.7 Hz) with the matched resistive load, than the other configurations. Moreover, the time to reach steady state at the resonant frequency with the matched resistive load is lower than the others. The maximum electrical power that can be generated from a vibrating mass is directly

related to the oscillation frequency and drops dramatically at low frequencies [2]. This is a logical outcome, since fewer oscillations per second of the piezoelectric generator will lead to less work done per second (i.e. less power). This results in the relatively low power results shown in Fig. 11 and Fig. 14.

The EHAM can harvest 37.5 μW when the mouse is running (importing the actual displacement). Fig. 15 (b) shows the stress at the root of the beam when the EHAM is excited by the actual data. The maximum stress is 0.5 GPa. Since the ultimate stress (failure stress) of the silicon is approximately 2 GPa and higher, this indicates the cantilever is in a safe range of operation.

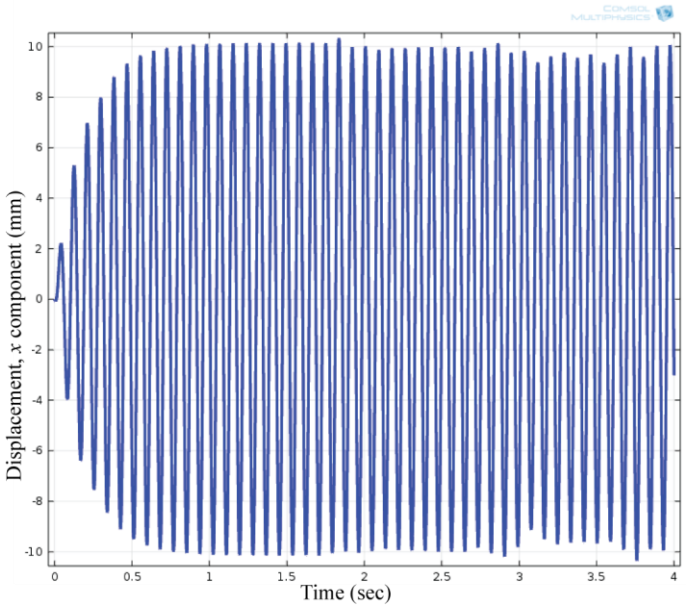

Figure 12: *x*-component displacement of EHAM, with an excitation at 11.7 Hz, with R_L =222 kΩ.

TABLE 5: MAXIMUM BEAM TIP DISPLACEMENT FOR DIFFERENT RESISTIVE LOADS

Frequency (Hz)	222kΩ (matched)	1kΩ	1 MΩ	100kΩ
9	±3.5	±2.5	±3	±3
10	±4.6	±3.5	±4.2	±4.5
11	±7.3	±7.5	±7	±7.2
11.7	±10	±8	±9.2	±9.5
12	±9	±7.8	±8.5	±9
13	±7	±4.5	±5	±6

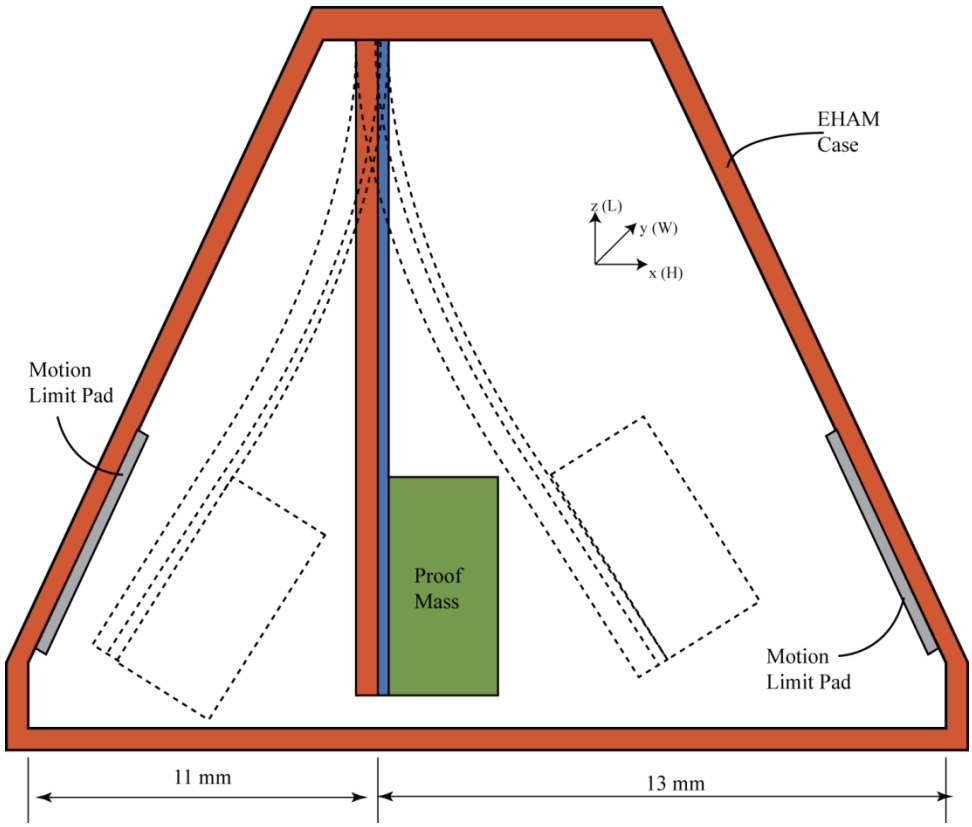

Figure 13: EHAM with motion limit pads.

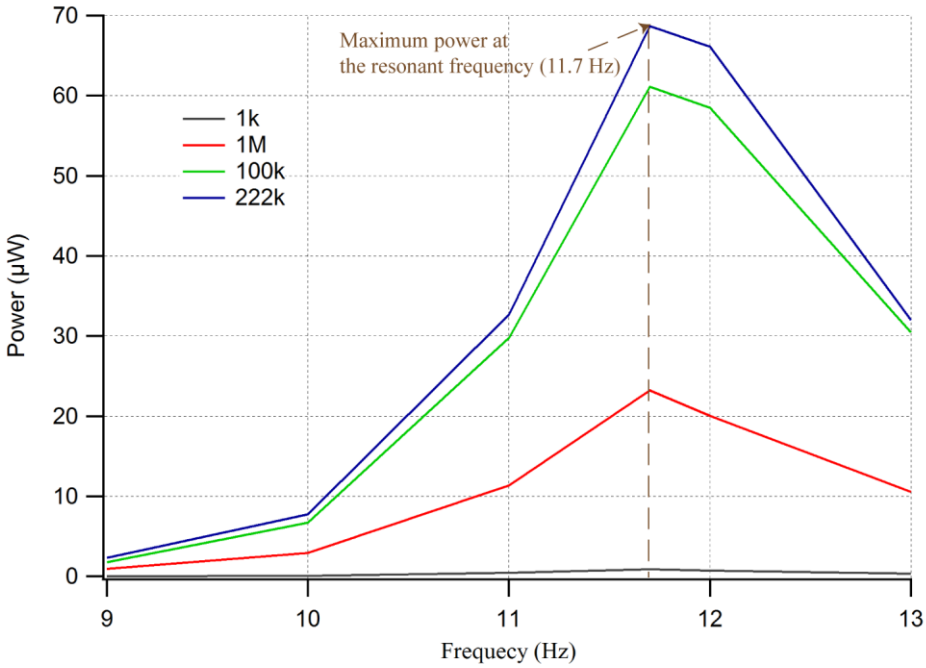

Figure 14: Power versus sweep frequency for different resistive loads.

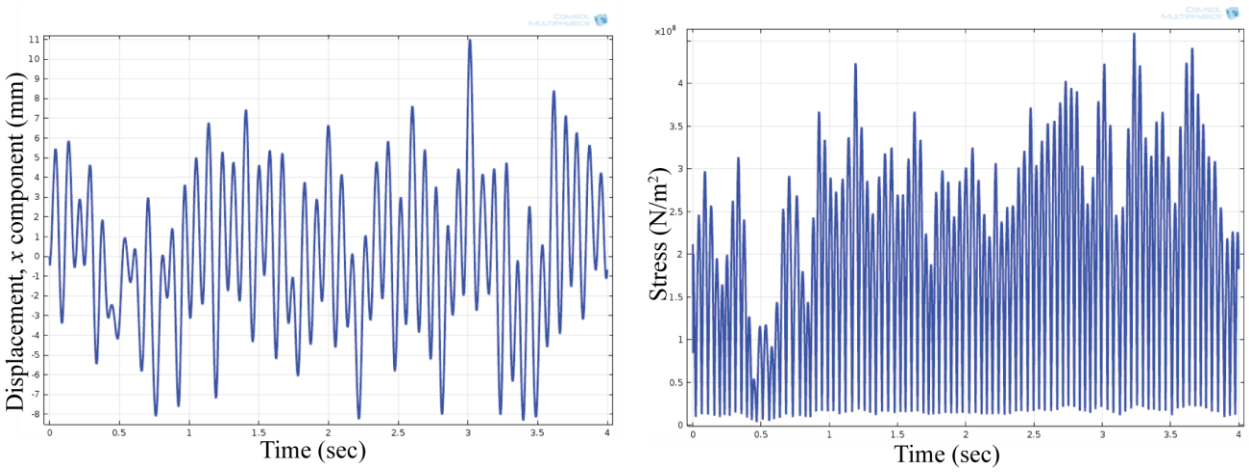

(a) **(b)**

Figure 15: Simulation results of exciting the EHAM by the actual displacement data; (a) *x*-component displacement of EHAM, (b) Stress at the root of the EHAM.

2.7 Conclusion

The EHAM model was proposed for harvesting energy from mouse motion. The EHAM was designed with the help of FEA COMSOL software, to predict beam displacement, beam stress, electrical power produced, and impedance matching for the application load. The design of this harvester consists of a cantilever beam with a piezoelectric layer, a proof mass, and motion limit pads. An experiment was conducted to characterize the frequency and acceleration amplitudes produced by a running mouse, using a head-mounted accelerometer. The PSD was computed for all axes, and the highest power was observed in the forward/backward direction (*x*-axis) at a frequency of 11.7 Hz, which is the typical gait frequency. It was found that the predominate frequencies and motion amplitude occurred along the anterior-posterior axis, which was roughly aligned with the *x*-axis of the measurement device. Hence, the proposed energy harvester was specifically designed to resonate at 11.7 Hz. A multi-scale FEA meshing approach was used to accommodate the thinness and long length of the cantilever design using mapped meshes. The final design parameters for the EHAM are listed in Table 3, which provide dimensions that can be reasonably tolerated by a mouse in a simple and manufacturable configuration. The EHAM is designed for operation with an excitation frequency of 11.7 Hz, with displacement amplitude as described in equation (14). Additionally, there are a few other mouse behaviors such as scratching and head lifting that also occur near the 12 Hz range. Although lower in acceleration amplitude, those motions may also contribute to the power generated. The simulation model described accounts for damping parameters in the material and also accounts for the effect of

different resistive circuit load (application circuit load) values. The simulation results confirmed that the maximum power was obtained when the matched resistive load was connected at the applied resonant frequency. The best case (constant excitation), continuous power for the device is predicted to be 68 μW. The simulation indicates that the EHAM is capable of harvesting 37 μW if driven by patterns of motion derived from measurements of mouse movements. These values are a consequence of 11.7 Hz operation and mouse running data, which inherently provides low power values, but may be of use in a low-power analog application circuit.

Chapter 3: Wireless Power Transfer

3.1 Introduction

The designed EHAM was able to harvest 68 µW from mouse motion using piezoelectric-based energy harvesting, as described in Chapter 2. This harvested power by the EHAM (68 µW) is insufficient to power biomedical devices. The thermoelectric EH and glucose fuel cells approaches are unsuitable to power the implantable biomedical devices in rodents, as explained in Section 1.3. We found the WPT approach is the suitable candidate technique to power implantable sensors/stimulators, specifically for applications involving sensors for rodents.

The WPT is the transmission of electric energy from a power source to a load without conductors. The power is transmitted wirelessly via an electromagnetic field/different radiation. The space around a radiation/transmitter source is divided into two separate regions that are the near field and the far field. We operate in near field region, roughly given as [43-44]:

$$r \ll \frac{\lambda}{2\pi} \tag{20}$$

The WPT is categorized into three types: electromagnetic radiation WPT, electric induction WPT, and magnetic induction WPT, as shown in Fig. 16. The electromagnetic radiation WPT works in the far field and has been used in many applications. These applications are: (1) RFID (radio frequency identification) that allows data stored in a device to be transferred wirelessly using electromagnetic waves [45]; (2) microwave WPT that is based on radio waves that have a spectrum range of 1-30 GHz [46]; (3) laser coupled WPT that is based on the photovoltaic effect [47]; (4) SPS (space solar power satellites) that is considered as a travelling energy plant in the geostationary earth orbit [48]. The electric induction WPT and the magnetic induction WPT systems are in the near field region and operate at distance less than a wavelength of the signal being transmitted [44, 49]. Inductive power transfer (IPT) is a popular technique of transferring power wirelessly over a short range, which is based on magnetic induction. This technique depends on two fundamental laws of physics: Ampere's law and Faraday's law [50-51]. Capacitive power transfer (CPT) is a technique used to transfer power wirelessly between the two electrodes of a capacitor, which depends on the theory of electric induction. The electrical power is transferred by means of an electric field. The CPT consists of a pair of capacitors each

consisting of two parallel plates separated by a certain distance. The transmitter is connected to the first plates of each capacitor and the receiver is connected to the second plates. When an alternating voltage is applied to the transmitter plates, a varying electric field will be generated across the two plates of both capacitors. According to Maxwell's equations, a time-varying electric field will produce a displacement current proportional to the rate of change of the electric field. The displacement current will generate an electric current in the receiver plates [51].

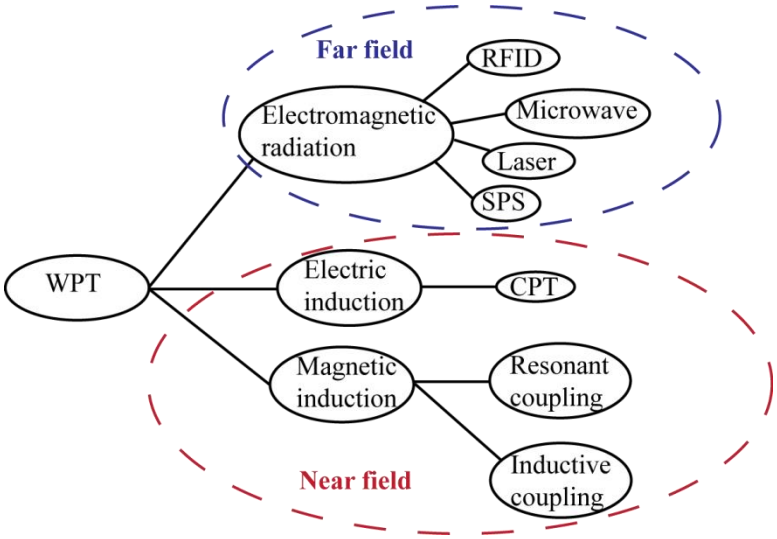

Figure 16: Category of WPT systems.

The CPT system is an inappropriate technique to transfer power to the implantable biomedical devices. This is due to the requirement of applying high voltages (kV) to the transmitter plate of the CPT and the need for large plates for long distances. Capacitive coupled systems are generally used in applications that require an intense electric field [51]. On other hand, the IPT system is based on the changing magnetic field that is created due to alternating currents through a primary coil (transmitter). The alternating magnetic field induces a voltage and a current onto a secondary coil (receiver) [1, 50-51]. Given the requirements for a general telemetric devices sensor/stimulator, it is recommended to use the IPT technique to power the biomedical devices [1-2, 50].

A common characteristic of the WPT applications for rodent telemetry acquisition is loose coupling between the primary and secondary coils [1-2]. These WPT systems are recognized as LCWPT, where their coupling coefficient is less than 2% [52-53]. To compensate for loose coupling, the use of resonant circuit systems is employed, to boost the induced voltage/current levels at the secondary circuit [1-2, 51]. The magnetic resonant power transfer is dependent on

factors such as the frequency match between the inherent resonant frequency of the primary circuit and the inherent resonant frequency of the secondary circuit [1]. The magnetic resonant technique was first proposed by Tesla [54].

This work proposes the use of a WPT system to continuously power a telemetric device. This provides power to the device for indefinite periods, without the risks of surgery for battery replacement or transcutaneous wiring. The proposed application is for a rodent implant device (RID) that can act as a stimulator and sensor for a freely moving small rodent. The current RID prototype is suitable for subcutaneous implantation in a rat, and is suitable as a head-mounted device for a mouse. Fig. 17 illustrates the mouse-based concept for telemetry acquisition, where the telemetric device is located on the head of a freely moving mouse. The mouse moves within a stationary primary coil wrapped around a small mouse housing cage sized 250 × 120 × 150 mm^3 (length × width × height). This cage size is needed to meet the minimum animal care standards for mice.

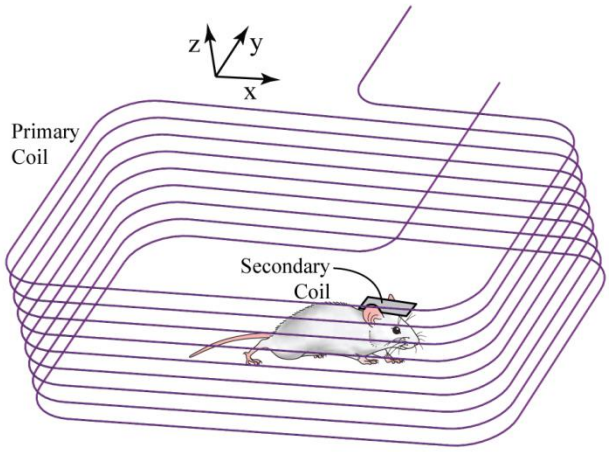

Figure 17: Rodent WPT concept.

3.2 Our Application Device

The use of animal models to investigate human disease processes plays a vital role in biomedical research. The telemetric devices for rodents are needed to investigate the behavior of rodents and collect the biological data from rodents. These telemetry devices require a reliable power source without limiting rodents' mobility or behavior. The RID is intended as a stimulator and EEG measurement device for small rodents. Electrophysiological recording and stimulation requires 51 mW for 100 – 300 milliseconds, to start up the application telemetry device. After

start up, the system can run indefinitely with a power of 12 mW of continuous power for periods of at least 24 hours, or preferably several weeks. The power requirement is based on the bio-signal acquisition (analog to digital bit depth and sample frequency), stimulation regiments, microcontroller power, and radio transmitter power [1-2, 53].

For our rodent telemetry application, the rodent moves freely within the cage, as illustrated in Fig. 17. While developing the telemetric device, we found several limitations: (1) the continuously changing orientation of the rodent leads to coupling loss/problems between the primary and secondary coils, presenting a major challenge. According to [35], they found the predominate orientation of mouse movement is along the *z*-axis (up and down) rather than the *y*-axis (left and right) or *x*-axis (forward and backward). Therefore, we propose a novel configuration of the secondary circuit to be able to harvest power while the RID is freely moving at any orientation from 0° through to 90°, with respect to the cage surface plane (*z*-axis); (2) The size and weight of the RID (telemetric device) must be suitable to be implanted subcutaneously in a rat or mounted on a mouse head; (3) The distance between the generated primary electromagnetic field and the secondary coil/RID varies as the animal moves around its cage; (4) A resulting mutual coupling effect of freely moving multiple secondary coils in the same primary coil, which causes a magnetic resonant mismatch between the secondary coils and the primary coil; (5) A rising temperature that occurs as a result of excessive received power by the secondary coil. This rising heat creates trouble for the electronic components of the telemetric devices. We propose a control scheme to eliminate the problems of the resonant frequency mismatch, and also the excessive received power causing high temperature, as listed in points (4&5). We considered these issues to develop a solution to address them by providing the required power to the RIDs that occupy minimal volume and weight.

We designed the WMS that is used to collect real-time performance data from the secondary circuit/RID, while testing LCWPT systems. We found that the traditional measuring techniques for the received power of WPT systems create measurement errors. These conventional techniques are coaxial cable-based that require the use of the voltage/current probes and oscilloscopes. We developed the WMS that is a portable tool to evaluate the RID/telemetric device without the problematic use of the conventional techniques.

When designing our RID, we consulted the ICNIRP (International Commission on Non-Ionizing Radiation Protection) to understand the effects of the electromagnetic field (energy

density) on living tissue of rodents. The ICNIRP provides scientific advice and guidance on the health and environmental effects of non-ionizing radiation (NIR) to protect living bodies (human and animals) and the environment from detrimental NIR exposure. NIR is sub-grouped into different frequencies or wavelength bands. These subgroups have different effects on the living bodies and require different protection measures. ICNIRP provides recommendations on limiting exposure for the frequencies in the different NIR subgroups [55]. Muscle and nerve stimulation occurs with frequencies of up to 100 kHz, while frequencies higher than 100 kHz cause tissue heating. The Specific Absorption Rate (SAR) is the parameter used to determine the effects of this heating. A SAR of 4 W/kg or higher is the threshold where harmful heating begins to occur in living tissue [56-57].

Prior to this PhD work, Dr. Delaney's team investigated telemetric devices for collecting bio-signals from rodents, to be powered by WPT. They developed the original primary and secondary coil architecture, using an earlier version of the *air core* secondary, as well as a multi-coil secondary design. They also developed the RF data transmission scheme and hardware for telemetry communication to the base station. In addition, they developed the EMG and EEG sensors used to acquire data from a rodent. In their multi-coil secondary design [1], two different coils were housed on the secondary, where each coil was connected with its own resonant capacitor and its own rectifier circuit: one coil was the earlier *air core* coil, and the other was a tightly wrapped ferrite rod. They encapsulated their telemetric device (secondary circuit), and it was successfully mounted on mice heads and subcutaneously implanted in rats. However, their telemetric device (secondary circuit) had several issues, including poor received power at high orientations, and had an electronic heating problem that damaged the encapsulation and the electronic components of the device. They used PP (parallel to parallel) topology to achieve magnetic resonant coupling, which has low efficiency in this WPT application involving rodents, as explained in detail in this thesis. In addition, their WPT system had issues in achieving resonant matching between the primary and secondary, and they did not use impedance matching within the secondary, which both led to low power transfer efficiency in that early system.

3.3 WPT Theory

The IPT is a popular technique for WPT based on magnetic induction over a short range. The principal operation of the IPT systems is creating an oscillating electromagnetic field that is

generated due to an alternating current through a primary coil. This electromagnetic field induces a voltage onto a secondary coil [1-2]. The resulting magnetic field at the secondary (receiver) coil can be obtained by integrating Biot-Savart's law around the primary (transmitter) loop [58]:

$$\vec{H} = \frac{I_P}{4\pi}\oint \frac{\overrightarrow{dl} \times \vec{r}}{r^3} \tag{21}$$

where, I_P is the current applied to the primary (transmitter) coil. The integration of Biot-Savart's law with respect to the line integral of the wire carrying the current (I_P) is [59]:

$$H = \frac{I_P N_P {a_P}^2}{2(\sqrt{{a_P}^2 + r^2})^3} \tag{22}$$

where, N_P is the number of primary turns, and a_P is the primary coil radius. By Faraday's law, the induced voltage (V_{ind}) at the secondary coil is given by the rate of change of flux crossing the secondary coil [44]:

$$V_{ind} = -N_S \mu_0 \mu_r A_S \cdot jwH \tag{23}$$

where, N_S is the number of secondary turns, A_S is the loop area of the secondary coil, μ_r is the relative permeability of a specific medium and μ_0 is the permeability of free space. Combining equations (22 and 23), the induced voltage in the secondary coil can be expressed in terms of the primary current (I_P), as [44]:

$$V_{ind} = -\frac{N_P N_S \mu_0 \mu_r A_S {a_P}^2}{2(\sqrt{{a_P}^2 + r^2})^3} \cdot jwI_P \tag{24}$$

There are four topologies for achieving magnetic resonant coupling between the primary and secondary coils. The topologies are SS, SP, PP, and PS, where the first S or P stands for series or parallel compensation of the primary winding, and the second S or P stands for series or parallel compensation of the secondary winding. In this work, we initially used the PP topology, as shown in Fig. 18 (a).

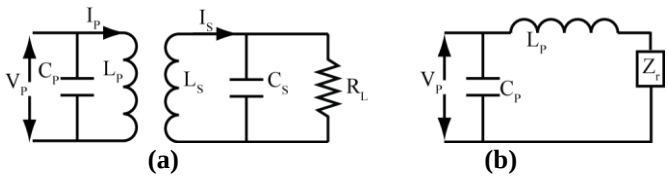

(a) **(b)**

Figure 18: PP topology of primary and secondary coils; (a) PP topology, (b) parallel compensation.

The load impedance of the secondary resonator is calculated as a lumped impedance Z_s whose value depends on the secondary parallel compensation as given by [60]:

$$Z_s = jwL_s + \frac{1}{jwC_s + \frac{1}{R_L}} \tag{25}$$

The loading effect of the secondary coil back onto the primary circuit is shown in Fig. 18 (b), as a reflected impedance Z_r. It depends on the coupling factor and operating frequency, and it can be written as [60]:

$$Z_r = \frac{w^2 {M_{SP}}^2}{Z_s},\ M_{SP} = k\sqrt{L_P L_S} \tag{26}$$

where, M_{SP} is the mutual inductance between the primary and secondary coils, and k is the coupling coefficient (value between 0 and 1). Substituting equation (25) into equation (26), the reflected impedance is obtained as [60]:

$$Z_r = \frac{w^2 {M_{SP}}^2 R_L}{{R_L}^2(w^2 C_s L_s - 1)^2 + w^2 {L_s}^2} + j\,\frac{-w^3 {M_{SP}}^2 \left[{R_L}^2 C_s \left(w^2 C_s L_s - 1\right) + L_s\right]}{{R_L}^2(w^2 C_s L_s - 1)^2 + w^2 {L_s}^2} \tag{27}$$

In order to minimize the VA ratings of the power supply and to achieve magnetic resonant coupling, it is desirable to operate at the zero phase angle of the impedance at the resonant frequency of the load impedance. This zero phase angle of the impedance at the resonant frequency must be achieved to ensure maximum power transfer. The primary capacitance used for PP topology can be obtained by [60]:

$$C_P = \frac{L_p - {M_{SP}}^2 / L_s}{(\frac{{M_{SP}}^2 R}{{L_s}^2})^2 + w^2 (L_P - \frac{{M_{SP}}^2}{L_s})^2} \tag{28}$$

The maximum power received by the secondary circuit occurs when the load is conjugately matched. At resonance, the reactive components cancel and the impedance is simply the real component, which is the resistive loss of the secondary tank. For maximum power transfer to occur, the load resistance needs to be equal to the resistive loss (R) of the secondary tank (L_SC_S). We found the optimum value of load resistance (R_L) required for maximum power transfer is:

$$R_L = \frac{R\sqrt{1+k^2Q_PQ_S}}{{Q_S}^2} \tag{29}$$

where, Q_P and Q_S are the quality factor of the primary and secondary coils, respectively. At resonance, the reactive parts in the secondary coil impedance cancel out. The transferred real power via the magnetic resonant coupling is defined as:

$$P_o = \frac{{V_{ind}}^2}{R_L} \tag{30}$$

3.4 Our Methodology/Approach

In this work, we employ a rectangular-helical primary coil, as shown in Fig. 17, with an approximately uniform internal magnetic field. Further, we employ ferrite rods within the secondary coil to increase the quality factor to improve the coupling at all orientations. Chapter 4 describes the novel design secondary coil configuration that eliminates the orientation problem between the primary and the secondary coils.

Researchers are using conventional techniques to measure the induced voltage, the received power, and the efficiency of the WPT systems. These techniques depend on using the coaxial cables, twisted-pair cables, or oscilloscope probes, which are sensitive to the parameters of the LCWPT systems. The use of these techniques leads to measurement errors of the LCWPT systems. In Chapter 5, we design a new measuring system that is denoted as WMS to accurately measure the induced voltage and the received power of the LCWPT systems.

Our novel development configuration of the secondary coil employing ferrite rods, captures electromagnetic flux at most orientations. The maximum efficiency achieved using this secondary circuit configuration is 1.5%, as explained in Chapter 4. A further limitation of our previous LCWPT system is poor efficiency because of high heat dissipation and losses in the primary and secondary circuits. The high efficiency is a great importance for the LCWPT for

biomedical applications. The LCWPT systems are recommended to have a good efficiency to minimize the electronic heating problem that represents a major concern for any implantable device [61-62]. Chapter 6 focuses on improving the efficiency of the LCWPT system. Chapter 7 reports the resonant frequency mismatch that occurs in the WPT systems using multiple secondary coils (receivers). A control scheme is designed to tune/detune the LCWPT system for rodent applications in Chapter 7.

For the experimental validation of this thesis, there were no animals (rodents) used. We used angled fixtures that mimic rodent orientations for the experiments. Our experiments using the SIP/RID are not currently conducted in vivo. In future work, we plan to mount the RID on mice heads or to implant subcutaneously in rats.

Chapter 4: WPT for Variable Oriented Telemetric Devices

4.1 Literature Work of WPT for Rodents

A number of researchers are investigating WPT for mice and rats. Where possible, features of their WPT systems are reported, such as their primary coil size and applied current, secondary coil received power, the use of the ferrite rods, multiple-secondary coils, and size. Wentz *et al*. developed a head-mounted device for mice using resonant RF (radio frequency) WPT. Their secondary coil employed a wrapped ferrite rod where the received energy was 200 mW continuous [63], with 2W bursts available when buffered with an adaptive supercapacitor circuit. Their primary magnetic field strength (H) was 300 A/m. Laskovski *et al*. designed a WPT device (*air core*) for mice roaming on top of primary planar-spiral coils, where each coil was 100 × 100 mm^2. The resulting electromagnetic field was not uniform, with reported blind-spots where the secondary coil received insufficient power [64]. Cong *et al*. designed a wireless implantable microsystem (*air core*) to capture blood pressure information from a freely moving laboratory mouse, with a 150 × 250 mm^2 primary, and a received power of 2.5 mW [65]. Soltani *et al*. designed a WPT system consisting of an array of planar-spiral primary coils (100 × 100 mm^2) to deliver power to a planar-spiral *air core* secondary coil (40 × 40 mm^2). They reported power transfer of 21-225 mW [66], with a parallel orientation between coils. Russell *et al*. demonstrated a WPT mouse implant with a wrapped ferrite secondary coil. It delivered 20 mW to the arbitrarily oriented secondary, using a system of 24 overlapping primary coils, each of which were 100 × 100 mm^2 planar-spiral coils. They were selectively switched, providing coverage anywhere over the surface area of 150 × 300 mm^2. The peak primary coil current was 4.4 A [67]. Kilinc *et al*. developed an implantable device (*air core*) for a freely moving mouse, to monitor organic compounds, pH and temperature. They designed a coil tracking system to move the primary coil, using a servo-controlled system with two rails (*x*-axis and *y*-axis) under the mouse cage. The moving primary coil was 80 × 80 mm^2, with a transfer of 1.7 mW to the secondary [68].

Other researchers designed WPT systems for rats. Jow *et al.* designed a WPT device (*air core*) for a rat roaming on primary spiral coils on printed circuit boards. The primary coil was 308 × 283 mm^2, consisting of an overlapping (four layers) hexagonal planar-spiral coil array. The maximum power received was 33 mW when the secondary coil was at 90^o with respect to the

primary coil plane [69]. McCormick *et al*. designed a WPT device (*air core*) for rats roaming over a charging pad (primary coil) to deliver 100 mW to a secondary coil, in a parallel orientation. The charging pad was 300 × 300 mm^2, with nine coils at resonant frequencies between 97 kHz and 209 kHz, driven by an H-Bridge inverter by a phase locked loop (PLL) [70]. Xu *et al*. designed a WPT implant (*air core*) for rats roaming on several planar-spiral primary coils, each 132 mm in diameter. Their WPT system used four coils, namely a driver, primary, secondary, and load coil. The secondary coil was a combo of planar-spiral and helical coil, with a 29 mm diameter. The driver and primary coils generated a nearly flat magnetic field that induces 1.3 V for neural stimulation [71-72]. Eom *et al.* built a WPT system for an implantable device in freely moving rodents. They used also four coils based on magnetic resonant coupling. Their implanted secondary coil (*air core*) was fabricated on the biocompatible liquid crystal polymer (LCP) substrate of a six-layer structure. Four of the six layers are assigned for a resonator coil of 20.5 turns per layer with outer and inner diameters of 19 and 5 mm, respectively. Their multilayered receiver coil was fabricated on a flexible polymer LCP substrate with conventional flexible printed circuit board (FPCB) technology. They built columnar dual-primary (transmitter) coils to generate a three dimensionally uniform electromagnetic field, within a cage of 150 × 200 × 150 mm^3. Their WPT system achieved efficiency of 15.2% [73]. Hsu *et al*. proposed a model of a secondary with multiple coils (three coils perpendicular to each other wrapped on a square ferrite core) for rats [74]. Hosain *et al*. designed an antenna that was mounted on a rat head for drain brain stimulation (DBS). Their wireless power transferred through a rectenna and inductive coupling with operating resonant frequency of 915 MHz. The dimension of the mounted antenna is 10 × 12.5 × 1.5 mm^3. The dimension of their primary coil is 171×159×41 mm^3, which is a compact transmitter with an integrated antenna of gain of 8 dBi and 60-degree beam pattern [75]. Amelia *et al*. built a miniature optogenetics head-stage for wirelessly stimulating the brain of rodents. The dimension of their head-stage is 15 × 25 × 17 mm^3, which weighs 7.4 grams. The head-stage consists of three stacked PCBs (printed circuit board) that are comprised of an electrophysiological signal readout circuitry, a power management unit (PMU), and a low-power RF microcontroller. The head-stage device is powered wirelessly into an animal chamber using inductive coupling, the maximum received power by the head-stage is 94.52 mW [76].

It is noted that the power transfer of the WPT systems in [64-67, 69-73] decreases when the

freely moving rodent moves away from the center of the primary coil (rodent's cage). However, the edge and corners are of particular importance, as it is common in rodent behavior to loiter in the corners and move adjacent to the edges of their enclosures [70]. The WPT system designed in our work delivers higher power at the edges of the cage than at the center. We show the measurements at the center of the cage only in this Chapter. The measurements of the received power at the center and edge of the cage are illustrated in Chapter 7.

Some researchers have proposed or designed a secondary with multiple coils [74, 77-78] for implantation, in order to achieve reasonable orientation independence from the primary coil plane. Each coil is ideally orthogonal to the others, and with similar area [19], or with area on the same order, such as in [77-78]. The volume reported in [77] is 1090 mm^3 (*air core*) and 480 mm^3 (ferrite core). It is 1020 mm^3 for *air core* in [78]. In these multi-coil designs [74, 77-78] each coil was connected with its own resonant capacitor, and its own rectifier circuit (or half-wave rectifier equivalent). The main problem of a multiple-coil secondary is resonant frequency mismatch between the coils, due to component property variations (i.e. tank capacitors and inductors), and mutual inductance effects between coils [2].

In this work, we employ a rectangular-helical primary coil, as shown in Fig. 17, with an approximately uniform electromagnetic field. We employ ferrite rods within the secondary coil, to increase the quality factor to improve the coupling at all orientations. As well, we employ a single wound secondary coil. This is advantageous since a single-coil winding is not plagued by frequency mismatch with other coils, or mutual inductance from other coils. Further our minimal ferrite size leaves volume for on-board electronics, and has reasonable volume as compared to multi-coil designs.

4.2 Methodology for Ferrite Configurations

We reported WPT with a secondary coil encircling a PCB without ferrite rods [1]. That secondary configuration is called the *air core* in this thesis. It exhibits low coupling with the primary coil when the *air core* coil plane is at high orientations (i.e. oriented beyond 30° relative to the primary coil *x-y* plane). For our rodent telemetry application, as illustrated in Fig. 17, the rodent moves freely within the cage. Hence, its orientation and posture are constantly changing, which results in variable coupling and hence high variability in power transfer. In some orientations coupling is lost, resulting in system reset. To remedy these problems we propose

using ferrite rods located at specific locations within the secondary coil to boost the power transfer. To show the effect of using ferrites, four configurations are used in this work, as shown in Fig. 20 and Fig. 27, called the *air core*, WFR_4 (four wrapped ferrite rods), 4MF (four medium ferrite) and 4MFA (four medium ferrite angled) configurations. To allow for performance comparisons, the latter three configurations use the same volume of ferrite rods, with the same ferrite length, and have similar coil inductance values.

A baseline of power transfer is first established with the *air core* design. A variation of the *air core* employing ferrite rods is the 4MF (four medium ferrites) configuration. 4MF is studied to investigate improvements in power transfer from the distributed addition of ferrites. Also, a traditionally wrapped ferrite rod pack referred to as WFR_4 is examined. We propose that power transfer is improved with the 4MF configuration, compared to the WFR_4 configuration.

Another issue is the reduced coupling or loss of coupling of the 4MF, WFR_4, or *air core* configurations at high angular orientations (where the secondary coil plane is beyond $60°$ with respect to the primary coil plane). At these high orientations, little magnetic flux passes through the secondary coil plane. To overcome this problem, we propose use of tilted ferrite rods angled at $45°$ with respect to the secondary plane, to improve the capture of magnetic flux at high orientations. This is called the 4MFA configuration. We propose that 4MFA will increase the power transfer in comparison to 4MF at high angular orientations. In addition, 4MFA occupies less volume than 4MF.

We first simulate the *air core*, WFR_4, 4MF and 4MFA configurations using FEA. The simulation results show vector plots of the magnetic flux density surrounding these configurations. As well, we show magnitude plots of the flux density passing through these configurations, at various angular orientations. This data is used to determine the total flux that passes through each coil configuration, at each orientation. The FEA simulations are non-resonant models; hence, further analysis beyond calculation of total flux is not warranted. Rather, the simulations provide insight into the effect of ferrite placement and orientation, to help with design of the best configurations.

Physical prototypes of these four configurations are constructed and experiments are done to determine performance. Each configuration is placed within the primary coil (Fig.17), using fixtures with variable orientation. Performance is determined by measuring the voltage induced at the secondary, of various configurations, at various angular orientations, at various locations,

with various currents applied to the primary coil and different resistor loads (R_L). Since the experimental work employs magnetic resonant coupling between the primary and secondary circuits, effects such as frequency matching, impedance matching, and quality factor, all influence the total power transfer.

4.3 Simulation Setup

A simulation using 3-D FEA with COMSOL software is done to determine the magnetic field distribution surrounding the various secondary configurations. FEA is used to discretize a physical model into a mesh of elements (subdivisions) and nodes, to find the approximate solutions to Maxwell's equations that govern the system behavior. Physical models with irregular geometric shapes and multiple materials, such as our configuration models, are well suited for FEA. The entire model is discretized into millions of elements, which are then combined into a set of equations describing the entire system, and these are then solved with the appropriate boundary conditions [2]. The motivation for using 3D FEA is twofold. First, to understand how the primary magnetic field interacts with the ferrite rods in the secondary coil when the secondary is oriented with respect to the primary field. Also, to correlate the total flux captured by the secondary coil to the ferrite rod size and location within the secondary. Such FEA analysis is not trivial, and cannot be done with 2D-based or 2D axis symmetric FEA analysis. It requires fully 3D FEA, which is seldom reported in literature [68, 70, 77]. The second motivation is to use these 3D FEA results to help design novel configurations of ferrite coil combinations suitable for different applications. Our motivation is to add a minimal volume of ferrite at specific positions within the secondary coil, to maximize the secondary performance at different orientations. The best ferrite utilization occurs when the ferrite rods are made as long as possible [79]. Despite the ferrite rods being the same volume, the FEA simulation found that the longer ferrite rods pull more magnetic flux than the wider ferrite rods [53, 79]. The size of the ferrites chosen in this work is 6.4 mm long by 1.6 mm in diameter. This ferrite size was suitable for the 4MFA configuration (Fig. 27), and provides a balance between providing sufficient space for onboard PCB electronics (microprocessor, radio, buffer capacitors, rectifier, EEG and stimulator) while minimizing the overall RID volume. The total weight of the 4MFA RID configuration is 1.8 g.

Many authors have used FEA simulation software for plotting the magnetic flux density [1, 67, 70]. We analyze the magnetic flux density distribution around (and within) various configurations in this work. The first simulation done is for the *air core* configuration. This consists of a primary coil (L_p) that is 250 × 120 × 150 mm^3 (length × width × height) in size, together with the secondary *air core* coil (L_S, simplified as one wire loop) that is 13.25 × 20.25 mm^2 in size, as shown in Fig. 20 (a). Both coils are placed in a spherical domain of radius 120 cm with the properties of air, as shown in Fig. 19 (a). A Frequency Domain Study is used to investigate the WPT model at an applied frequency, corresponding to the system's resonant frequency. A simulated current of 2.5 A (peak-to-peak) is applied through the primary coil windings. The simulation output is the magnetic flux density at all points in space. A sample plot surrounding the primary coil is shown in Fig. 19 (b) (arrow vectors are normalized, with only the *x*-*z* plane plotted for figure clarity).

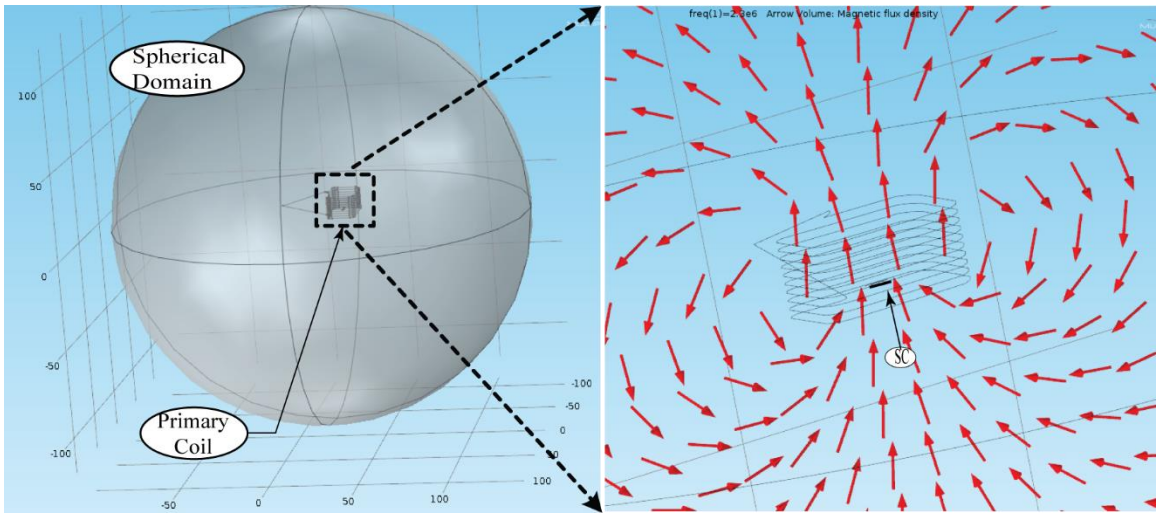

(a) **(b)**

Figure 19: WPT model in COMSOL; (a) spherical workspace, (b) arrow plot on single *x*-*z* plane, showing normalized magnetic flux density.

The second simulation is for the WFR$_4$ configuration. This uses the same primary coil (L_p), applied current, and spherical workspace, as in the previous simulation. The WFR$_4$ configuration consists of four pieces of ferrite rod (FR) bundled together as shown in Fig. 20 (b), where each piece is 6.4 mm in length and 1.6 mm in diameter. The secondary coil (SC) is wrapped tightly around the rods ($L_{S\text{-}WFR4}$, modeled as a simplified one wire loop). The third and fourth simulations are done for the 4MF and 4MFA configurations, respectively. These also use the same primary coil (L_p), applied current, and spherical workspace, as in the previous simulation.

The 4MF configuration uses four pieces of ferrite rod (6.4 mm long and 1.6 mm diameter) placed within the corners of the *air core*, as shown in Fig. 20 (c). The 4MFA configuration consists of the same four pieces of ferrite rod placed within the corners of the *air core*; however, they are tilted at 45° to the secondary coil plane, as shown in Fig. 20 (d). For both of these, the secondary coil is wrapped around the 13.25 × 20.25 mm^2 PCB ($L_{S\text{-}4MF}$ and $L_{S\text{-}4MFA}$, each modeled as a simplified one wire loop). The type of ferrite rod used in this work is 4B1, which is suitable for the operating frequency of our WPT system. Its material specifications [80] are configured in COMSOL, including the B-H curve and permeability as a function of frequency.

Modeling the system with 3D FEA simulation is challenging due to the considerable differences in the size between various system parts, or in the parts themselves. For this system, the secondary wire diameter is 0.100 mm, the ferrite rod diameter is 1.6 mm, and the major dimension of the primary cage is 250 mm. To guarantee FEA mesh integrity, the aspect ratio of individual 3D mesh elements should not be greater than three. Therefore, the 3D mesh must transition from small to large features, which necessitates a large number of elements for systems with considerable part size differences. The simulation convergence and accuracy of the calculated solution strongly depend on the quality of the mesh elements. An excessive number of elements increases the computing time [2].

The parts of each configuration are meshed using different elements, with different mesh settings. To minimize 3D FEA complexity and ensure convergence, the secondary coil and primary coil wires are modeled as 1D line elements. The sphere domain and the ferrite rods are modeled with tetrahedral elements, using the Finer and the Extremely Fine meshing settings, respectively. For example, the complete mesh of the entire 4MF simulation consists of 1,304,507 elements. Fig. 21 illustrates the meshing of the *air core*, WFR_4, 4MF and 4MFA configurations. The internal COMSOL mesh quality was found to be of high quality.

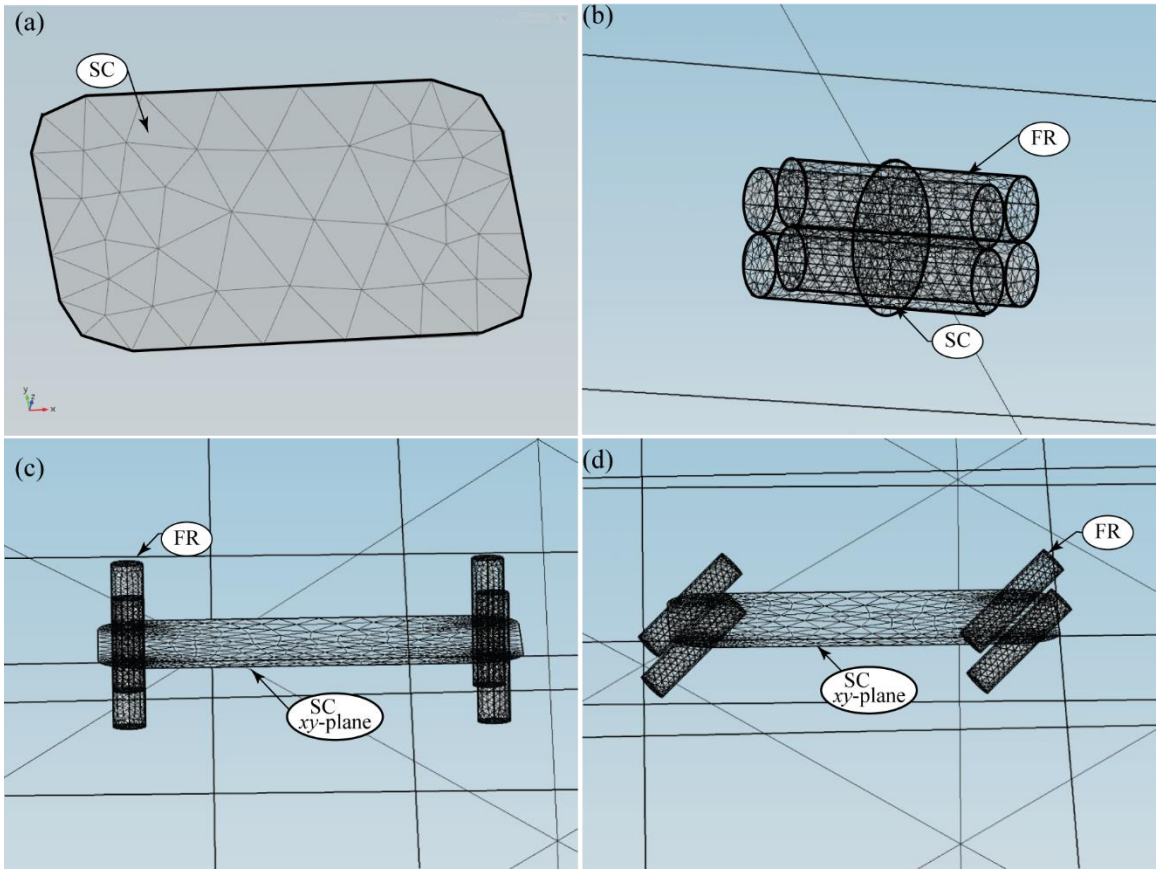

Figure 20: Meshing of secondary; (a) *air core*, (b) WFR$_4$, (c) 4MF and (d) 4MFA.

4.4 Simulation Results

The simulation results demonstrate a significant improvement in the total flux captured when using a secondary coil configuration with ferrite rods. The magnetic field is locally attracted by the ferrite, which improves the coupling between the primary and secondary coils. Fig. 21 shows an *x-y* plane plot of the magnetic flux density distribution produced by the primary coil, at the middle of the cage. The rectangle labeled SC indicates the location used to simulate the *air core* and other configurations, at the 0°, 30°, 60°, and 90° orientations. The 3D FEA models developed here cannot simulate resonant power transfer behavior; hence a direct estimate of power is not done. Instead, flux densities and total flux passing through the secondary coils are reported.

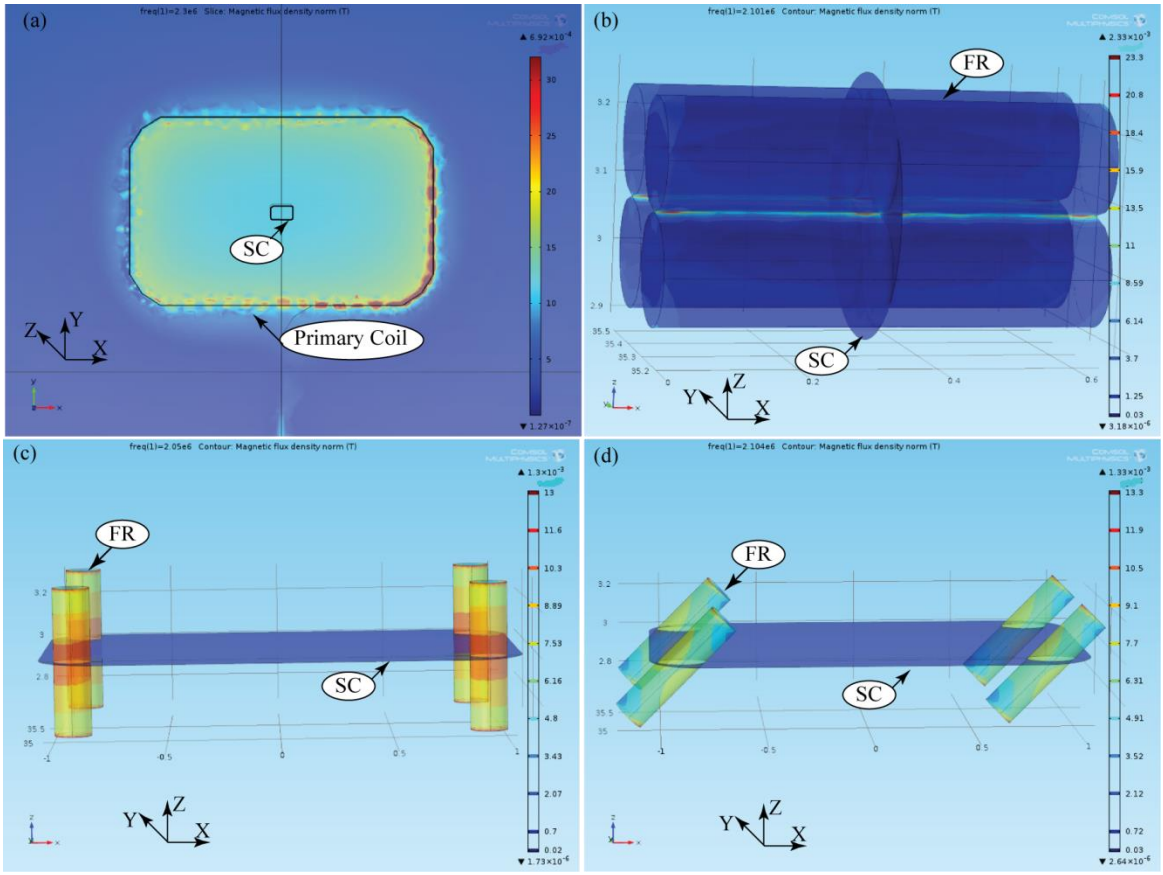

Figure 21: Color plot of the magnetic flux density; (a) plotted on the *x*-*y* plane within and around the primary coil, (b) plotted within the WFR_4 configuration coil, (c) plotted within the 4MF configuration coil plane and within the ferrite rods, (d) plotted within the 4MFA configuration coil plane and within the ferrite rods.

The mutual inductance, M_{SP}, between the primary and secondary coils, is defined when a second coil is located such that it captures a portion of the flux generated by the primary coil as [79]:

$$M_{SP} = \frac{\psi_{SP}}{I_P} \tag{31}$$

where, ψ_{SP} is the total flux captured by the secondary coil, that is given by [79]:

$$\psi_{SP} = \oint \overrightarrow{B_C} \times \overrightarrow{dA_S} = N_S \mu_0 \mu_r A_S H \tag{32}$$

where, B_C is the flux density crossing perpendicularly through the secondary coil. Combining equations (22, 31 and 32), the M_{SP} is given as [79]:

$$M_{SP} = \frac{\mu_0 \mu_r N_P {a_P}^2 N_S {a_S}^2 \pi}{2(\sqrt{{a_P}^2 + r^2})^3} \quad (33)$$

where, a_S is the secondary coil radius. When the coils are merely angularly misaligned the approximation mutual inductance equals $M_{SP} \cdot cos\theta$, where θ is the angle between of the primary and the secondary coils. The mutual inductance (M_{SP}) increases when a ferromagnetic material is inserted within the secondary coil (L_S). This is due to an increase in the relative permeability (μ_r) and thus an enhancement of the magnetic flux through the secondary coil. The aim of using ferrite rods in inductively coupled systems is to improve the power transfer between the primary and secondary coils [56]. Fig. 22 illustrates an arrow plot of the magnetic flux density, passing through the 4MF configuration. The plots are done in the *x*-*z* plane, where that plane intersects the axis of two ferrite rods. The arrow plots are logarithmatic, and show the 4MF configuration at 0°, and 30° orientations.

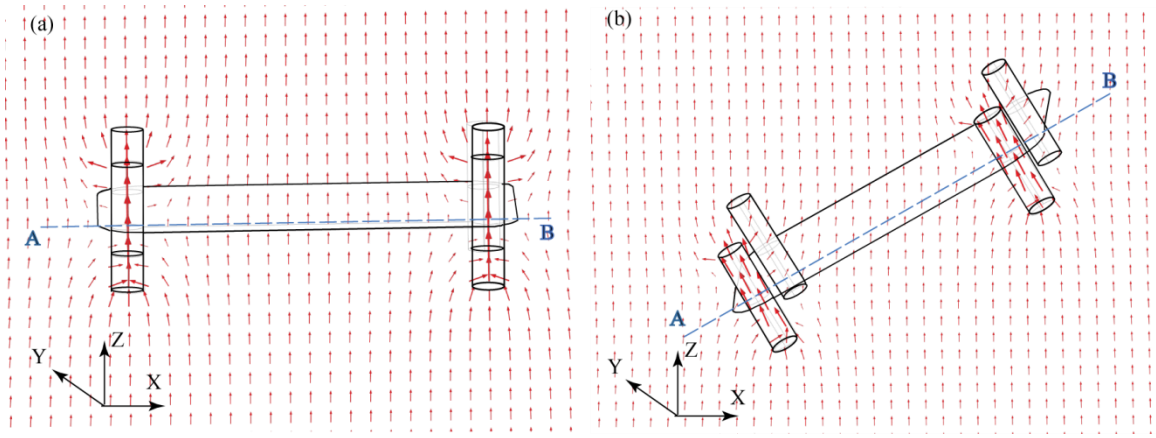

Figure 22: Arrow plot of the magnetic flux density passing through the 4MF configuration. Plots are in the *x*-*z* plane only; (a) 4MF at 0° orientation, (b) 4MF at 30° orientation.

Fig. 23 illustrates an arrow plot of the magnetic flux density, passing through the 4MFA configuration at the 0°, 30°, 60° and 90° orientations. The simulation results show that magnetic flux is pulled into the ferrite rods from the surrounding space, thereby increasing the flux density inside the ferrite rods. Note line AB shown in Fig. 22, which passes through two ferrites on the *x*-*y* plane. The magnitude of the flux density crossing the secondary coil, along line AB is then determined, and is plotted in Fig. 24. As seen from Fig. 24, the ambient magnetic flux density produced by the primary coil is approximately 1.15×10^{-4} Wb/m^2 in locations away from the ferrites. Close to the ferrites, but not within them, the field strength drops to near zero for the 0°

and 30° orientations. This occurs since the ferrites have consumed the surrounding field near their tips, leaving little flux around them. In this sense, there is an effective capture diameter (ECD) of flux around the tip of the ferrite, where all surrounding flux is drawn in. The ECD is related to the length, volume and material properties of the ferrite, as well as the ambient field strength. The ECD concept will be discussed further in the discussion. Within the ferrites, the field strength is relatively high. Using the plotted information of Fig. 24 and similar plots adjacent to the ferrites, the total flux ψ_{SP} passing perpendicularly through the inside of the secondary coil *x-y* plane is computed, as listed in Table 6.

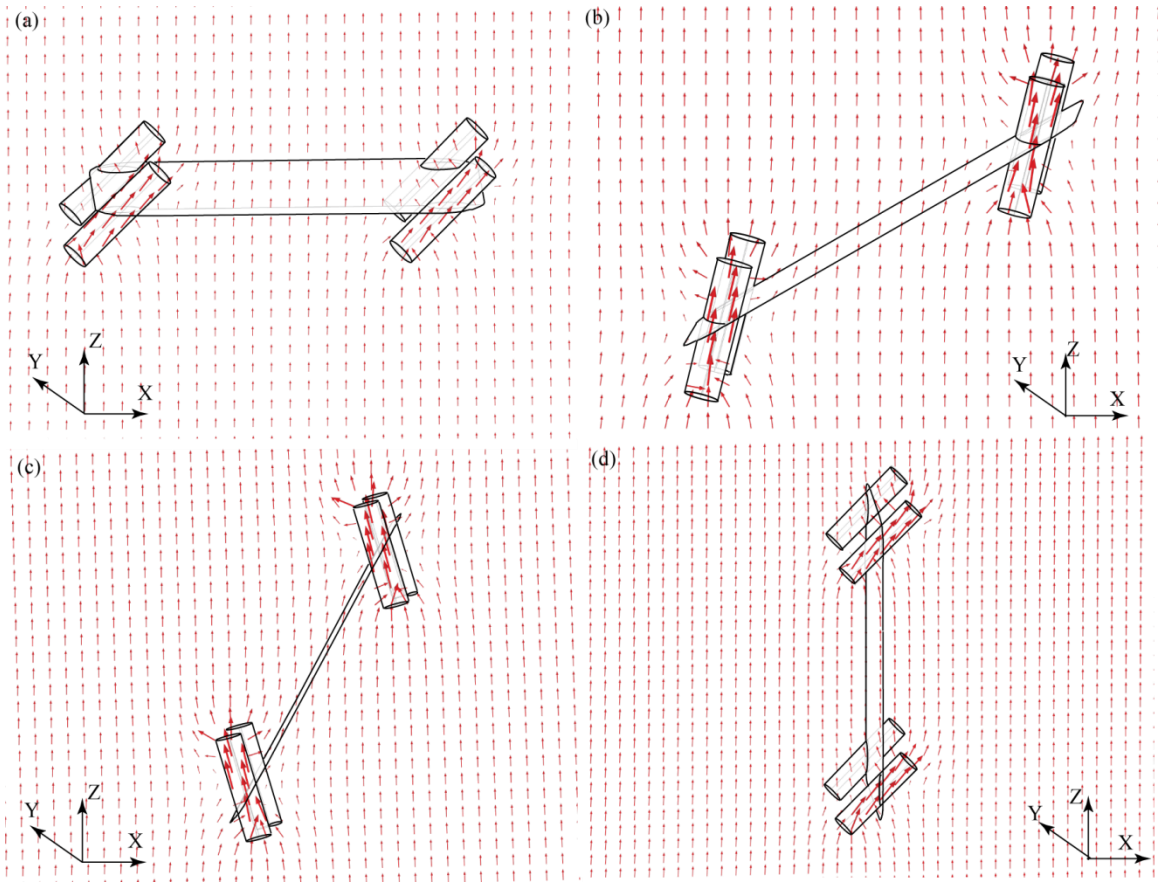

Figure 23: Arrow plot of the magnetic flux density passing through the 4MFA configuration. Plots are in the *x-z* plane only; (a) 4MFA at 0° orientation, (b) 4MFA at 30°, (c) 4MFA at 60°, (d) 4MFA at 90°.

The results of Table 6 begin with the nominal case for the *air core* secondary (with no ferrite rods), where the total flux through the coil is only a function of angular orientation. Notice that the ambient flux density through the 4MF coil and the 4MFA coil is less than the ambient flux density passing through the *air core* coil, at the 0° orientation. This occurs since the ferrite ECD starves the field in its vicinity, leaving less flux to pass through the air-filled portions of coil. For

the case of WFR_4, nearly no ambient field is available for the coil, since it is all captured by the ferrites. For the case of 4MF, 4MFA and WFR_4, the flux density within a single ferrite rod (third column) is listed. The total flux within all ferrites (fourth column) crossing normal to the coil is found by the ferrite area × number of ferrites × third column. The total flux (ambient + ferrite) of each configuration is listed in the fifth column. Note that the 4MF simulation predicts a substantial increase in flux gathered, in comparison to the *air core* configuration for the 0°, 30° and 60° orientations. However, it is near zero at the 90° orientation. The simulation predicts that the 4MFA configuration gathers less flux at the 0° and 30° orientations in comparison to 4MF (as expected since its ferrites are angled at 45˚). However, 4MFA provides improvement at the 60° and 90° orientations in comparison to 4MF, since it can still draw in flux at high orientations. The case of WFR_4 is provided as a reference, and demonstrates that the same volume of ferrite when tightly wrapped by a coil is far less effective than either 4MF or 4MFA, and is not effective at the 90° orientation.

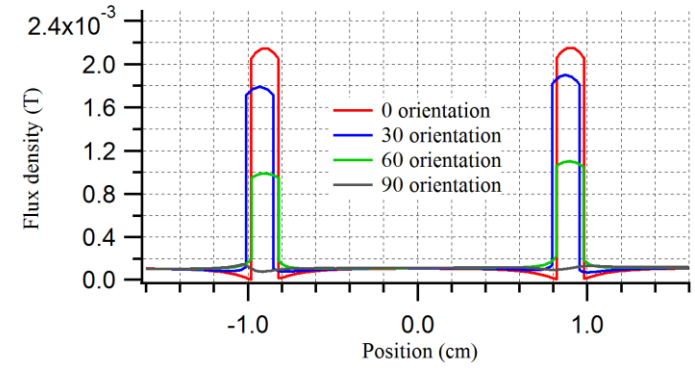

(a)

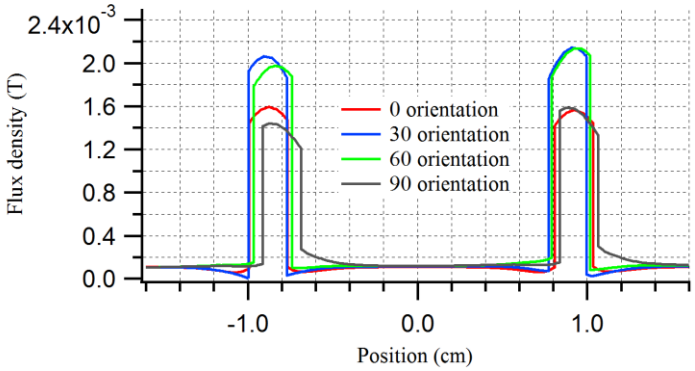

(b)

Figure 24: Waterfall plot of the magnetic flux density within the ferrite rods and the air space around them, where they intersect the plane corresponding to the secondary coil windings (coil *x*-*y* plane); (a) 4MF, (b) 4MFA.

TABLE 6: SIMULATION RESULTS OF SECONDARY COIL CONFIGURATIONS

Configuration	Ambient Flux through Coil $(Wb) \times 10^{-8}$	Flux Density in Ferrite (Wb/m^2)	Total Flux in Four Ferrites $(Wb) \times 10^{-8}$	Total Flux ψ_{SP} in Config $(Wb) \times 10^{-8}$
Air core, 0˚	2.95	0	0	2.95
Air core, 30˚	2.56	0	0	2.56
Air core, 60˚	1.48	0	0	1.48
Air core, 90˚	0	0	0	0
4MF, 0˚	2.37	2.20×10^{-3}	1.77	4.14
4MF, 30˚	2.32	1.60×10^{-3}	1.29	3.61
4MF, 60˚	1.61	0.70×10^{-3}	0.56	2.17
4MF, 90˚	0	0	0	0
4MFA, 0˚	2.55	1.60×10^{-3}	0.91	3.46
4MFA, 30˚	2.14	2.10×10^{-3}	1.19	3.33
4MFA, 60˚	1.45	2.10×10^{-3}	1.19	2.64
4MFA, 90˚	0	1.50×10^{-3}	0.85	0.85
WFR_4, 0˚	0	1.10×10^{-3}	0.89	0.89
WFR_4, 30˚	0	0.90×10^{-3}	0.72	0.72
WFR_4, 60˚	0	0.50×10^{-3}	0.40	0.40
WFR_4, 90˚	0	0	0	0

4.5 Experimental Setup

The four configurations have been physically prototyped and are tested using our custom designed LCWPT system. The WPT system can be divided into two parts, namely the primary and secondary circuits, as illustrated in Fig. 25. Magnetic resonant coupling is achieved by tuning the primary section such that both sections resonate at the same frequency.

The power is supplied to the primary circuit using a DC power supply. A signal generator (Agilent 33250A) provides the desired frequency to a Class-E power amplifier, which is used to

generate a sinusoidal current (I_P) in the primary coil (L_P), which in turn generates the electromagnetic field. This alternating electromagnetic field induces a sinusoidal voltage (V_{ind}) in the secondary coil (L_S) of the secondary implant prototype (SIP), which is rectified into a DC voltage (V_{rec}) that powers the application load (R_L). The DC voltage (V_{rec}) is measured across the load R_L, using the WMS that we have designed. The WMS is powered by battery and communicates via radio to a remote base station connected to a laptop. The WMS wireless data transmission helps our WPT measurements, since it overcomes many problems when using corded oscilloscope probes [81], to measure the secondary circuit. Initially, our attempts to measure the V_{rec} across the load R_L used an oscilloscope via coaxial cable. However, those measurements exhibited offset and noise problems, as explained in detail in Chapter 5.

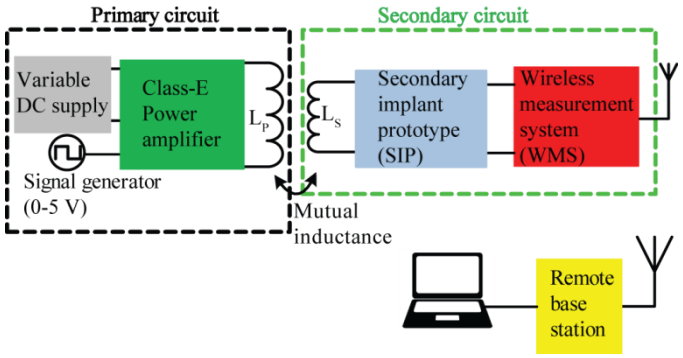

Figure 25: Block diagram of proposed LCWPT.

The Class-E amplifier design used to drive our primary coil (L_P) is shown in Fig. 26. This is a common approach used extensively by Sokal *et al*. who demonstrated the operational characteristics of their zero-voltage-switching (ZVS) inverter [82]. The Class-E topology is preferred as it reduces the stress on the switching element to a minimum. Our Class-E amplifier is configured as parallel resonance, where C_{par} works in combination with C_{tank}, to create a primary resonant tank, as shown in Fig. 26. We vary the parallel capacitor, C_{par}, to adjust the resonance of the primary circuit. The series capacitor (C_{ser}) shields the MOSFET from the high voltage developed by the primary resonant tank. The choke inductor (L_{Choke}) is connected in series with the DC power supply (V_{CC}) and blocks the ac current from the DC supply [53]. The parallel capacitance normally present in a Class-E amplifier has been replaced here by a diode where the diode allows for suboptimum operation [78].

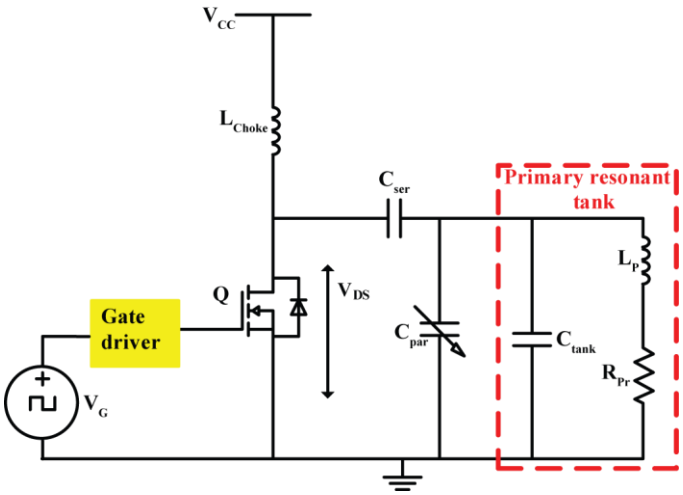

Figure 26: Class-E amplifier design schematic (parallel resonance).

A pulse train (V_G, duty cycle 0.5) is applied at the gate driver (MIC4421). The switch used is a MOSFET (STP16NK65Z), which has high power handling and nanosecond switching capabilities [83-84]. This MOSFET was also selected due to its relatively low output capacitance (C_{oss}) at high V_{DS} [84]. It is important to note that the C_{oss} is effectively absorbed by the C_{par} [2]. The power amplifier can deliver a maximum sinusoidal current (peak-to-peak) of 7 A through the primary coil, however, we use only up to 2.5 A in this work. This creates sinusoidal voltages (peak-to-peak) of up to 2.3 kV across the primary resonant tank, shown in Fig 26.

The SIP consists of a L_SC_S-tank (different for each of the four configurations) and a full bridge rectifier, as shown in Fig. 27. The rectification is an important part of the secondary circuit in the LCWPT system, where it is vital to efficiently utilize the generated V_{ind}. High frequency rectifiers have two losses associated with the diodes; losses due to forward conduction and a high frequency loss that can be attributed to the finite switching time of the diode. The switching losses occur as a consequence of the reverse recovery time of the diode. The forward conduction losses exist due to the forward voltage of the diode and the loss associated with its non-zero series resistance. Several rectifier topologies can be implemented for LCWPT (low power applications). The small diameter of the secondary coil (L_S) and the poor coupling factor, make it difficult in most applications to induce a high secondary voltage (V_{ind}). For this reason, full-bridge rectifiers with Quad diodes designed for use in ultra-high-speed switching applications [85] are preferred to rectify the induced voltage [86]. Fig. 27 shows the schematic diagram and cross section of the *air core*, WFR_4, 4MF and 4MFA configurations. The rectifier output from each configuration is connected to the load, R_L. The secondary coil is wound around the

perimeter of the PCB for the *air core*, 4MF and 4MFA configurations. For WFR_4 the secondary coil is wrapped directly around the ferrites.

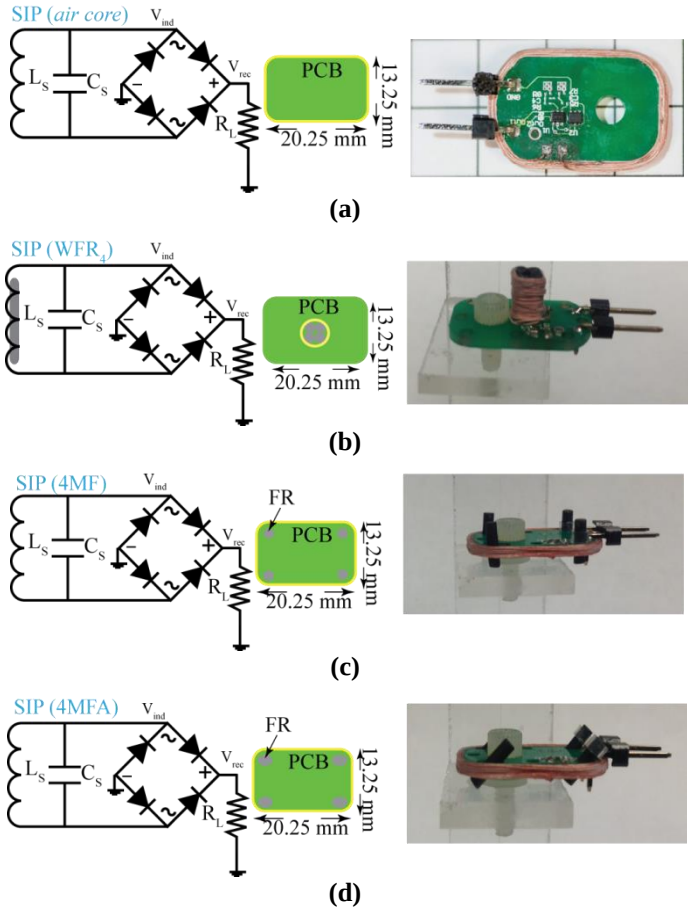

Figure 27: SIP configurations; (a) *air core*, (b) WFR_4, (c) 4MF and (d) 4MFA.

To achieve high quality factors, inductors with low effective series resistance (ESR) are required for high frequencies, due to the skin effect and proximity effect [2]. To reduce the ESR, multistrand Litz wires are commonly used [87]. For the application of this work, the ideal frequency range of operation is 100 kHz to 4MHz, where no biological effects have been reported [88]. All four configurations of the secondary coil employ 48/15 AWG/strands Litz wire. The number of turns per layer used in the *air core*, 4MF and 4MFA configurations is 7 turns/layer for four layers, so the total number of turns is 28 turns. The number of turns per layer used in WFR_4 is 25 turns for two layers, so the total number of turns is 50 turns.

The resonant frequency of each configuration is a function of its own L_SC_S-tank properties and is not adjustable. The secondary L_SC_S-tank is created by using a fixed 235 pF capacitor (C_s) for all configurations. The coil parameters (Q and L_s) of each configuration are listed in Table 7, as measured using a HP 4285A LCR meter. The resulting resonant frequency and the impedance (R_{LC}) for each configuration are listed in Table 8, along with the L_SC_S-tank impedance, which are measured using a HP 4193A Vector Impedance Meter.

TABLE 7: PARAMETERS OF THE SECONDARY COIL OF SIP CONFIGURATIONS

Configuration	Q	L (μH)
Air core	36	22.4
WFR_4	51.3	25.7
4MF	44	29.5
4MFA	44.3	26.8

The impedance matching within the SIP must be designed appropriately to avoid internally reflected power loss from the secondary load (R_L) to the secondary L_SC_S-tank. The rectifier in the SIP exhibits impedance with a resistive and reactive part. The reactive part (capacitive component) of this load impedance can be considered as part of the tank impedance of the secondary circuit. Maximum power will flow when the resistive component of the load R_L is conjugately matched [2], as explained in Section 3.3. Our experimental measurements make use of a conjugately matched load R_L to ensure the maximum power transfer for the overall system. Each SIP configuration has different impedance magnitude (R_{LC}), as shown in Table 8. Hence, different resistor loads (R_L) are suggested to determine the matched impedance for the SIP configurations (Fig. 30).

TABLE 8: MEASURED RESONANT FREQUENCY AND THE IMPEDANCE MAGNITUDE OF SIP CONFIGURATIONS

Configuration	F_{res} (MHz)	R_{LC} (kΩ)
Air core	2.302	10.1
WFR_4	2.101	12.3
4MF	2.057	12
4MFA	2.104	11.5

For our LCWPT experiments, the primary coil is wound around a small animal cage (Fig. 17). To simulate the angular orientations of a rodent, four experimental fixtures were constructed to hold the SIP at various orientations (0°, 30°, 60° and 90° with respect to the *x*-*y* plane of Fig. 17). Each fixture holds the SIP at a 3 cm height above the base of the cage, at the center of the cage. Fig. 28 shows the experimental setup of the complete LCWPT system. The output voltage of the Class-E power amplifier is measured by a high voltage probe and the primary current (I_P) is measured by a current probe (Agilent N2893A). The high voltage and current probes are connected to the oscilloscope, as shown in Fig. 28. Prior to each WPT experiment, a calibration procedure is done to ensure resonant coupling between the primary and secondary.

Most of the system losses occur as heat at either the amplifier transistor (MOSFET) or the primary coil (L_P). A temperature increase at the primary coil (L_P) is not critical because it is a passive component and more resilient to heat [86]. A 12V DC brushless fan is used to achieve an air flow for forced air cooling. In addition, the heat sink on the MOSFET further enhances the heat-dissipation capabilities. Fig. 29 shows the top view of the Class-E power amplifier.

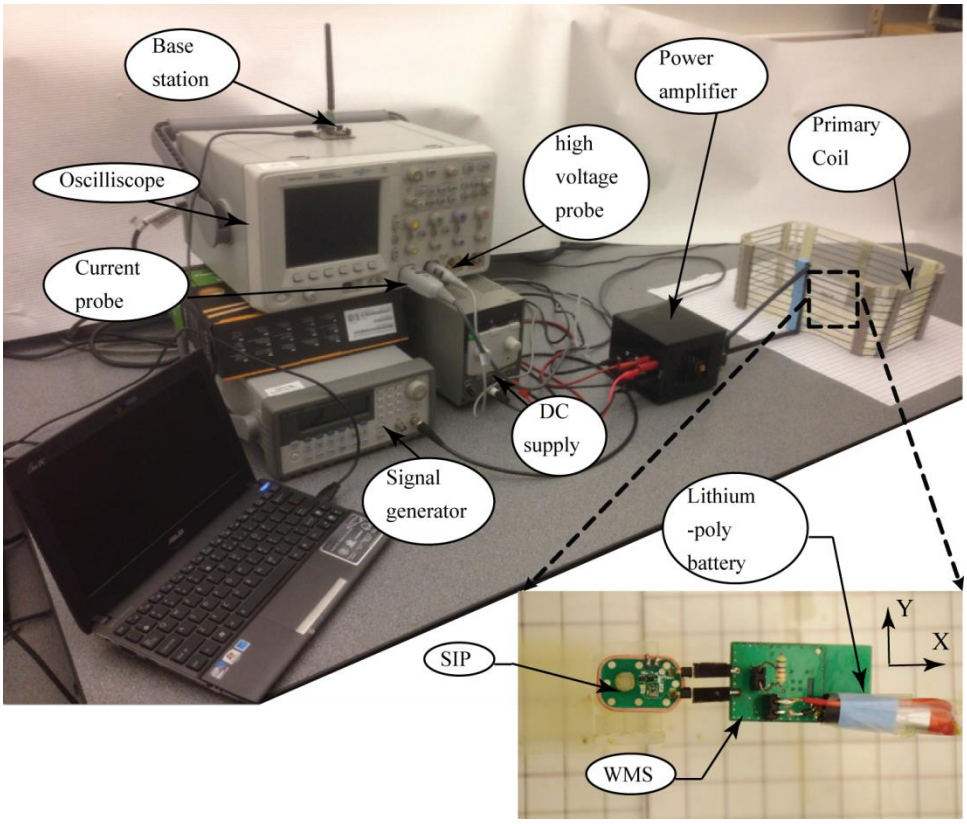

Figure 28: WPT experiment setup.

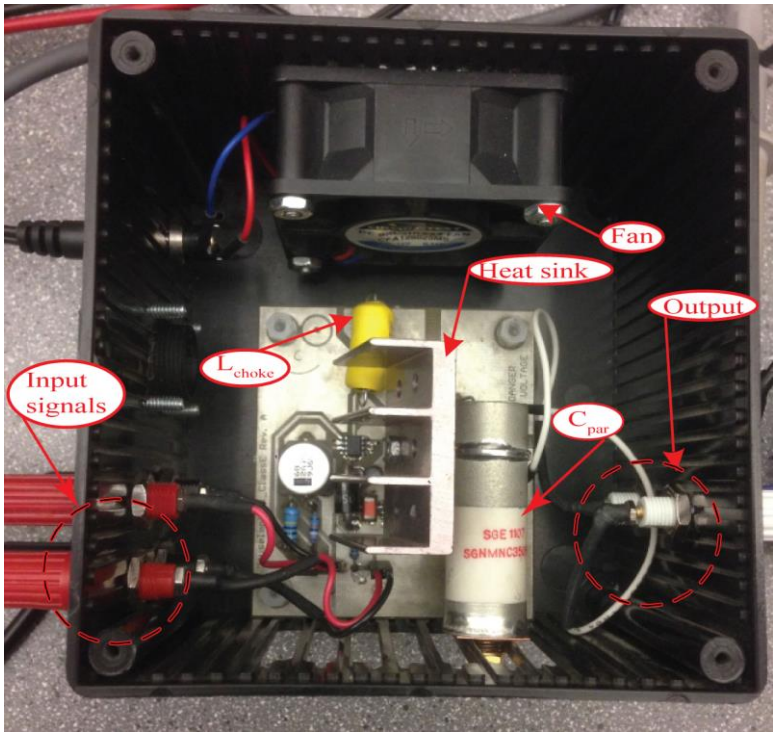

Figure 29: Top view of the Class-E power amplifier.

4.6 Experimental Results

Experiments with the four prototype SIP configurations were conducted to measure the power transfer between the primary and secondary circuits. The experiments varied four independent parameters: the SIP orientation (0°, 30°, 60° and 90° with respect to the *x-y* plane), the position of the SIP with respect to the primary coil, the matched impedance of the secondary circuit, and the current (I_p) applied to the primary coil (1, 1.5, 2 and 2.5 A peak-to-peak sinusoidal). The resulting voltage induced in the secondary SIP was measured by the WMS. In this Chapter, the rectified voltage and the received power were measured at the center of the cage only. All the measurements of the received power (V^2_{rec}/R_L) are RMS values. For the work of this thesis, there were no animals (rodents) used. We used angled fixtures that mimic rodent orientations for the experiments. Our experiments using the SIP/RID are not currently conducted in vivo.

4.6.1 Air Core Configuration

Fig. 30 shows a plot of the power received by the *air core* configuration with different resistor loads when the SIP is located at the centre of the primary coil, 3 cm above the base at a 0° orientation. The maximum power, with a matched load of 5 kΩ, is found to be 58 mW with an

applied primary coil current (I_p) of 2.5 A. The rectified voltage (V_{rec}) is measured across the R_L by the WMS, and the values are recorded in Table 9. Fig. 31 shows the power received by the *air core* configuration with a matched load (5 kΩ) at 0°, 30°, 60°, and 90° orientations.

The results of the *air core* configuration are expected. As the applied primary current increases, the V_{ind} increases, leading to higher power transfer. As the orientation of the secondary increases beyond 0°, coupling is reduced, leading to lower V_{ind}, which becomes very small when $\theta \approx 90°$. The power transfer could be further increased, by increasing the primary coil current, I_p, until the ferrites become saturated. This is possible as long as the DC power supply has sufficient power, the parameter V_{DS} (Fig. 26) stays within its breakdown voltage, and the primary coil voltage and current are safe.

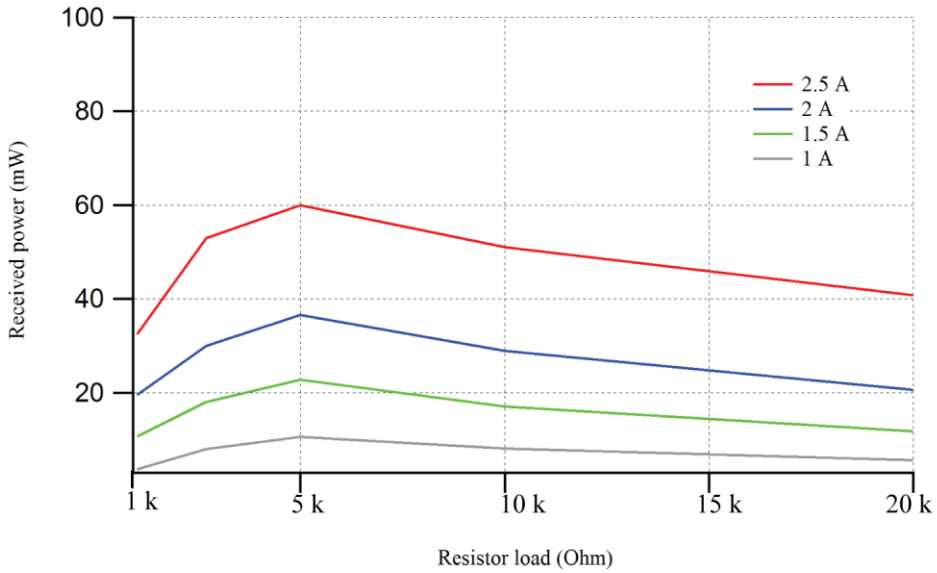

Figure 30: Power received in the *air core* configuration versus resistor loads for different currents applied to the primary coil. The SIP was located at the middle of the primary coil, in a horizontal (0°) orientation.

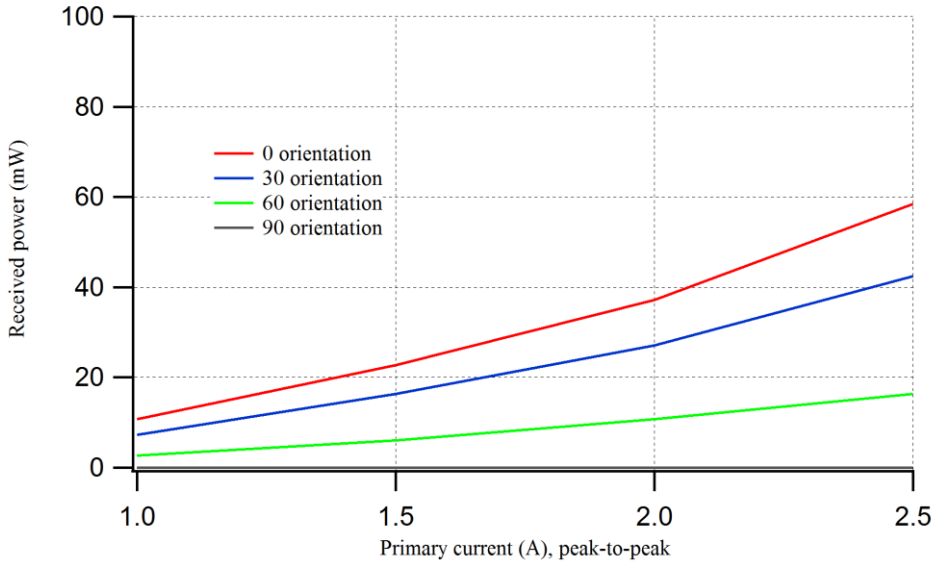

Figure 31: Power received in the *air core* configuration at the middle of the cage, with a 5 KΩ load R_L.

4.6.2 WFR4 Configuration

Fig. 32 shows a plot of the power transferred to the WFR_4 configuration at the middle of the primary cage. WFR_4 uses a R_L value of 5 kΩ to achieve impedance matching within the SIP. The V_{rec} is measured across R_L, and is recorded in Table 9. The maximum power received is 20.8 mW, which occurs at the 0° orientation with a primary coil current (I_p) of 2.5 A.

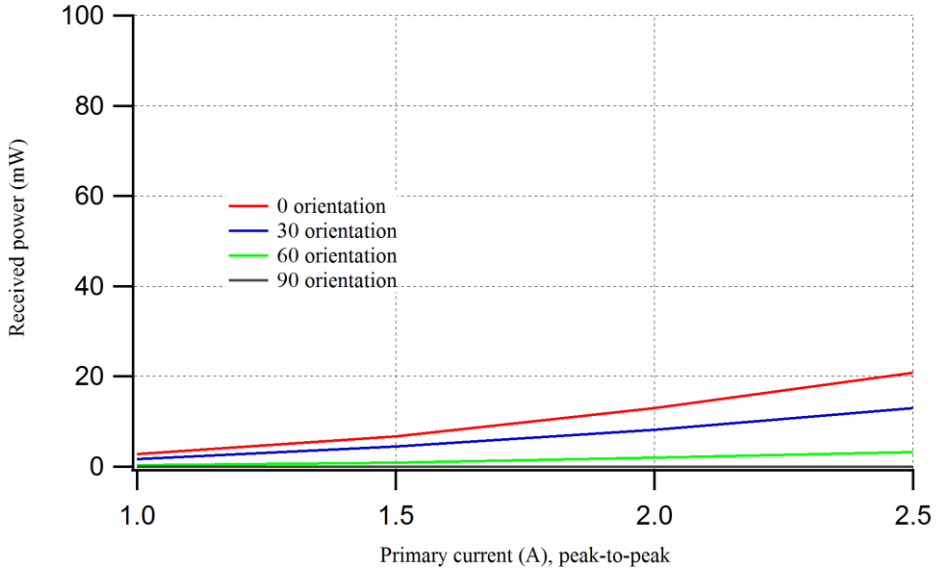

Figure 32: Power received in the WFR_4 configuration at the middle of the cage, with a 5 KΩ load R_L.

4.6.3 4MF Configuration

Fig. 33 shows a plot of the power transferred to the 4MF configuration at the middle of the primary cage. The 4MF configuration uses a R_L value of 10 kΩ to achieve impedance matching within the SIP. The V_{rec} is measured across R_L, and is recorded in Table 9. The maximum power received is 86 mW, which occurs at the 0° orientation, with a primary coil current (I_p) of 2.5 A. The 4MF configuration differs from the *air core* due to the 4 ferrite rods placed perpendicular to the PCB, as shown in Fig. 27 (c). Recall that the FEA simulations predict that 4MF picks up more flux at all orientations, compared to the *air core*. The experimental results confirm an increase in the received power at all orientations, as expected. However, the 4MF configuration is not effective at the 90° orientation, where the received power is only 1 mW.

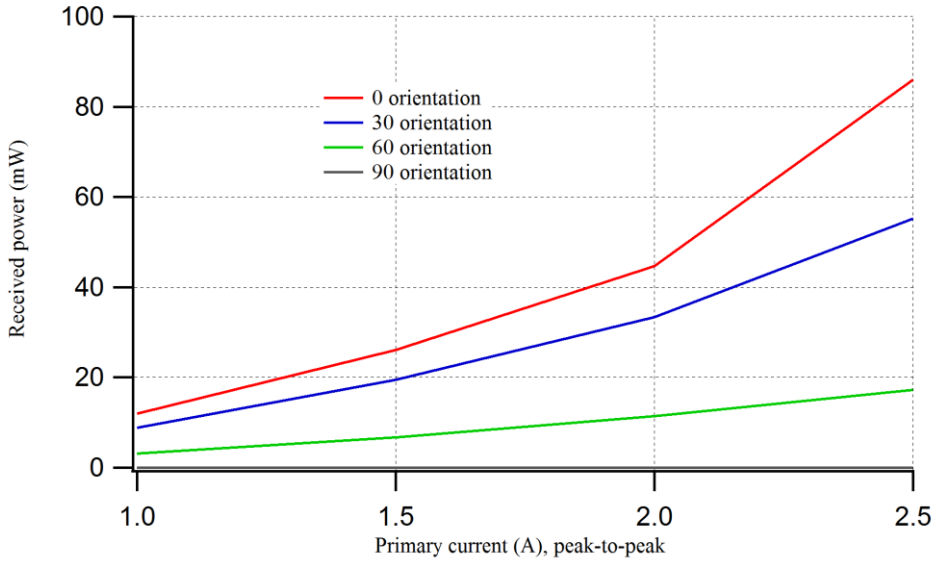

Figure 33: Power received in the 4MF configuration at the middle of the cage, with a 10 KΩ load R_L.

4.6.4 4MFA Configuration

Fig. 34 shows a plot of the power transferred to the 4MFA configuration at the middle of the primary cage. The 4MFA configuration uses a R_L value of 10 kΩ to achieve impedance matching within the SIP. The V_{rec} is measured across R_L and is recorded in Table 9. The maximum power received is 113 mW, which occurs at the 0° orientation, with a primary coil current (I_p) of 2.5 A. 4MFA has tilted (45°) ferrite rods located at the edges of the PCB, as shown in Fig. 27 (d). It can be seen that the power collected by 4MFA is higher than the 4MF configuration at all orientations, yet it uses the same size secondary coil with similar L and Q properties as listed in

Table 7, and the same size and volume of ferrites. The angularity of the ferrite rods at 45° demonstrates an improvement in coupling. Even at the 90° orientation, the power received by 4MFA is 1.7 mW (with I_p of 2.5 A), where all other configurations collected near zero power. The FEA simulation results predict that 4MFA would have a flatter spread of collected flux at the 0°, 30° and 60° orientations, as shown in Table 6. This flatter trend can be observed in the V_{rec} data of Table 9, at these orientations.

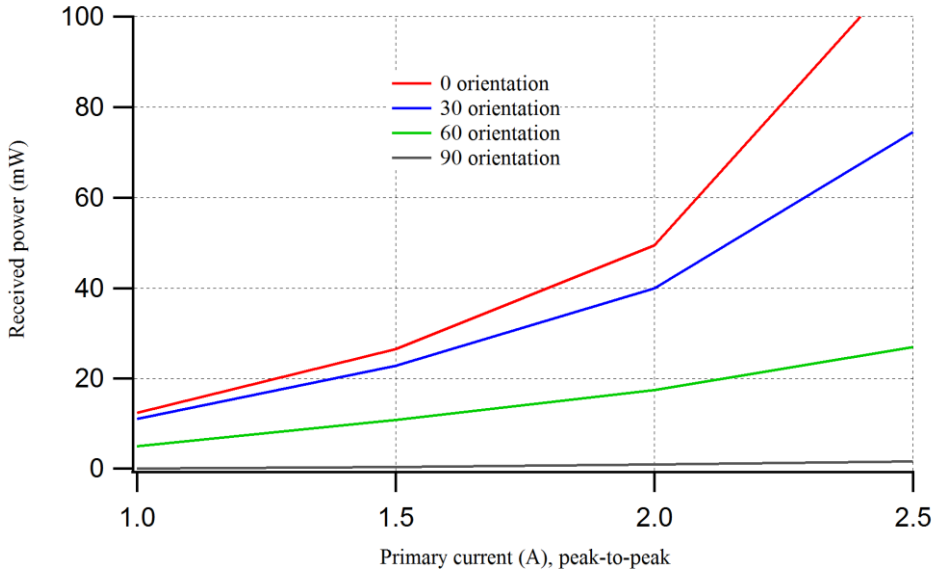

Figure 34: Power received in the 4MFA configuration at the middle of the cage, with a 10 KΩ load R_L.

4.7 Discussion

Improvements in wireless power transfer between the primary and secondary coils have been observed when using a small volume of ferrite rods within the secondary coil, at specific locations. This can be seen in the simulation results of Table 6, and also the experimental results of Table 9 and Figs 31 – 34.

The 4MF configuration shows a clear improvement in power transfer as compared to the air core configuration, as expected. The ability of the *air core* coil to harvest magnetic flux is directly proportional to the coil area through which the primary field passes, which defines the induced voltage (V_{ind}) in the secondary coil. Addition of ferrites draws more flux into the coil, resulting in improved coupling and hence power transfer.

The comparison of 4MF vs. WFR_4 is more interesting. Given that both configurations use the same volume of ferrite material, and have similar coil properties (L and Q), it is noteworthy to

observe that 4MF is far more effective at power transfer than WFR_4 at all orientations. This is noteworthy since the normal practice in the literature is to tightly wrap the windings around the ferrite for most WPT applications, as is done with WFR_4. The 4MF configuration is more effective for WPT for a number of reasons: (i) The coil winding area of 4MF is larger at 13.25 × 20.15 mm^2 than WFR_4, so extra ambient flux is captured, as listed in Table 6; (ii) The ferrite rods have an ECD. Since they are placed close to the corners of the 4MF coil windings, this allows them to pull magnetic flux into the coil from further beyond the coil. This effectively increases the coil area to a much larger size. The ECD is estimated as 9 mm in this work, but will vary for different shapes and properties of ferrite, as well as primary field strength. The ECD size can be visualized with the FEA simulations, as shown in Fig. 22 (a). In this work, we used 4 ferrites since their ECD areas overlap inside the coil, and hence the 4 ferrites consume most of the internal field. Addition of more ferrite rods within 4MF yields very little additional gain; (iii) Corner placement of the ferrite rods is important, since they would be much less effective if placed in the center of the secondary coil. The distance between the ferrite rods themselves is governed by the ECD. If two ferrite rods are placed too close together, such as for WFR_4, they will compete for the same flux, and hence will reduce their effectiveness. This only holds true as long as the ferrites are not saturated. If the ferrites become saturated, they can be placed closer together; (iv) The length of the ferrite rods (in addition to corner placement) also plays an important factor for collecting flux at orientations beyond 0°, such as between 0° and 90°. The maximum length of the ferrite rods becomes a design compromise between the device total volume and power transfer. In summary, although 4MF is more effective at power transfer than WFR_4, both are not effective at orientations that approach 90°.

To improve the performance of the 4MF configuration at high orientations, the 4MFA configuration was created by tilting the ferrites at 45° with respect to the PCB. It is observed that 4MFA will increase the power transfer in comparison to 4MF at all angular orientations. The motivation to tilt the ferrites was to allow them to draw flux through the secondary coil, even when the secondary coil is oriented at 90° to the primary electromagnetic field. This can be observed in the simulation of Fig. 23 (d). Further, Table 9 and Fig. 34 show that 4MFA is the most effective for WPT at any orientation, in comparison to all other configurations.

The complete WPT system can be characterized in terms of end-to-end efficiency, from the DC supply source to the SIP application load R_L ($\eta_{DC\text{-}Load}$). This can be calculated as [81]:

$$\eta_{DC-Load} = \frac{P_o}{P_{in}} \tag{34}$$

where, P_{in} is the total DC input power to the system (i.e. into the power amplifier and transfer link). Table 10 summarizes the efficiency of the *air core*, WFR_4, 4MF and 4MFA configurations. It is found that the efficiency of the power transfer depends on the coupling coefficient between the coils and their quality factors. The coupling coefficient essentially depends on the relative size of the primary and secondary coils, and their spatial arrangement [2]. In our application, the mouse is always inside the cage (primary coil), as shown in Fig. 17. Inside the primary coil, the electromagnetic field is uniform along the *z*-axis. Generally, inside there is little variation in received power along the *z*-axis. Once the RID (telemetric device) moves outside the coil (*z*-axis), the magnetic flux density is non-uniform and lower than inside the cage. In the region outside the coil, the efficiency of the LCWPT system ($\eta_{DC\text{-}Load}$) drops significantly. In this work, we did not measure outside the primary coil (cage).

The efficiency of our LCWPT system increases with increased primary current using this LCWPT system (PP topology). This LCWPT system draws 330 mA and 25 V from the DC power supply to provide primary current (I_P) 2.5 A (peak-to-peak). These VA ratings are high, so the total efficiency of this WPT system is low. In Chapter 6, the LCWPT system is redesigned to improve the efficiency.

Some comparisons can be made between the simulation results and the experimental results, in relation to induced voltage improvements from the addition of ferrite rods. Note that the simulation results are non-resonant, while the experimental results are resonant, hence, only comparisons of normalized trends can be made. Table 11 shows the total flux ψ_{SP} calculated from the simulation results (from Table 6), and the rectified voltage (V_{rec}) measured from experiment (from Table 9). Also included is the normalized percent variation (NPV), defined as: $\psi_{SP}/(\psi_{SP}$ at 0°), and V_{rec}/V_{rec} at 0°) for simulation and experiment, respectively. For WPT, the V_{ind} is directly proportional to the total flux ψ_{SP} passing through the secondary, so normalized comparisons can be made. For the *air core* configuration and the WFR_4 configuration, it can be seen that the NPV for the simulation matches the NPV for the experiment, quite well. For the 4MF configuration, the NPV for simulation and experiment are relatively close, however, discrepancies are observed for the 30° and 60° orientations. For the 4MFA configuration, there are significant differences in NPV between simulation and experiment. The simulation predicts

that the angled ferrites should create a flatter induced voltage between the 0° through 60° orientations, with a notable increase at 90°. However, experimental results show a more gradual variation in the V_{rec} across the orientations, also with a reasonable improvement at 90°. Recall that the "total power" for 4MFA as indicated in Fig. 34 is still much higher than other configurations. This indicates that the simulation of 4MFA requires further work to sufficiently model this complex 3D arrangement.

TABLE 9: RECTIFIED VOLTAGE V_{REC} MEASURED ON THE SIP ACROSS LOAD R_L

	1.0 A primary current	1.5 A primary current	2.0 A primary current	2.5 A primary current
Configuration	(V)	(V)	(V)	(V)
Air core, 0˚	7.3	10.6	13	17.1
Air core, 30˚	6	9	11.6	14.6
Air core, 60˚	3.7	5.5	7.3	9.1
Air core, 90˚	0	0	0	0.14
4MF, 0˚	10.9	16.2	21.1	29.3
4MF, 30˚	9.4	13.9	18.3	23.5
4MF, 60˚	5.6	8.2	10.7	13.1
4MF, 90˚	0	0	0.14	0.32
4MFA, 0˚	11.1	16.3	22.2	33.6
4MFA, 30˚	10.5	15.1	19.9	27.3
4MFA, 60˚	7.1	10.4	13.2	16.2
4MFA, 90˚	1.2	2.3	3.3	4.1
WFR_4, 0˚	3.7	5.8	8.1	10.2
WFR_4, 30˚	2.9	4.7	6.4	8.1
WFR_4, 60˚	1.2	2.1	3.2	4
WFR_4, 90˚	0	0	0	0.26

For the application of this work, the SIP is intended as a stimulator and EEG measurement device for small rodents, as shown in Fig. 35. In such an application, the power needed to start up the circuit is 51 mW for 100 – 300 milliseconds. After start-up, the system can run indefinitely with a power of 12 mW. Given the experimental results reported here, the 4MFA configuration is best suited for the stimulator/EEG application to deliver power at typical orientations and positions of the rodent within the animal cage. Although 4MFA cannot deliver enough power at the 90° orientation, the rodent rarely stands in such a pose with the device at this angle, for more than 1 second. To cope with the reduced power, a capacitor bank (C_{st} of 800 µF) is used to store energy, where the storage period is given by:

$$\Delta t = \frac{\Delta V \times C}{I_L} = \frac{(9.27 - 3) \cdot 800 \cdot 10^{-6}}{4 \times 10^{-3}} = 1.3\ seconds \tag{35}$$

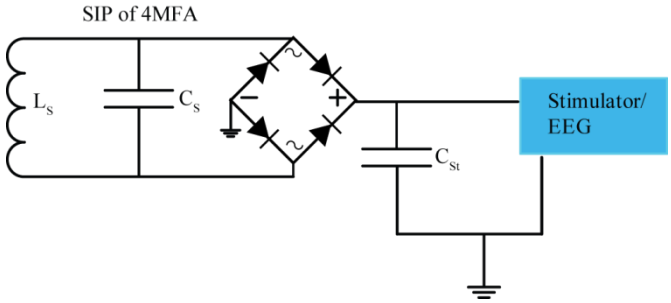

Figure 35: Circuit diagram of RID.

TABLE 10: TOTAL EFFICIENCY ($\eta_{DC\text{-}LOAD}$)

Configuration	1.0 A primary current (%)	1.5 A primary current (%)	2.0 A primary current (%)	2.5 A primary current (%)
Air core, 0˚	0.38	0.52	0.63	0.77
Air core, 30˚	0.17	0.37	0.46	0.56
Air core, 60˚	0.04	0.10	0.18	0.22
Air core, 90˚	0	0	0	0
4MF, 0˚	0.42	0.6	0.76	1.13
4MF, 30˚	0.31	0.45	0.57	0.73
4MF, 60˚	0.11	0.15	0.19	0.23
4MF, 90˚	0	0	0	0
4MFA, 0˚	0.44	0.61	0.84	1.5
4MFA, 30˚	0.39	0.52	0.68	0.98
4MFA, 60˚	0.18	0.25	0.3	0.36
4MFA, 90˚	0	0.01	0.018	0.02
WFR_4, 0˚	0.1	0.15	0.22	0.27
WFR_4, 30˚	0.06	0.10	0.13	0.17
WFR_4, 60˚	0.1	0.02	0.03	0.04
WFR_4, 90˚	0	0	0	0

TABLE 11: COMPARISON BETWEEN SIMULATION RESULTS AND EXPERIMENTAL RESULTS

Secondary coil configurations	Simulation		Experiment	
	Total Flux ψ_{SP} through the coil	Normalized Percent Variation	Rectified voltage in Secondary	Normalized Percent Variation
	$(Wb) \times 10^{-8}$	(%)	(V_{rec})	(%)
Air core, 0˚	2.95	100	17.1	100
Air core, 30˚	2.56	87	14.6	85
Air core, 60˚	1.48	50	9.1	53
Air core, 90˚	0	0	0.14	1
4MF, 0˚	4.14	100	29.3	100
4MF, 30˚	3.61	87	23.5	80
4MF, 60˚	2.17	53	13.1	45
4MF, 90˚	0	0	0.32	1
4MFA, 0˚	3.46	100	33.6	100
4MFA, 30˚	3.33	96	27.3	81
4MFA, 60˚	2.64	76	16.2	48
4MFA, 90˚	0.85	25	4.1	12
WFR_4, 0˚	0.89	100	10.2	100
WFR_4, 30˚	0.72	82	8.1	79
WFR_4, 60˚	0.40	45	4	39
WFR_4, 90˚	0	0	0.26	2.5

Chapter 5: Design Wireless Measurement System

5.1 Literature of Traditional Measuring Techniques

In order to characterize the LCWPT systems, some key performance parameters need to be accurately measured. These include the induced voltage, the received power, and the overall efficiency of the LCWPT, measured from the secondary circuit. A number of researchers have measured the induced voltage, received power, or efficiency of WPT systems with various schemes using coaxial cables, twisted-pair cables, or oscilloscope voltage/current probes.

Jow *et al.* used a digital oscilloscope (MSO4034B, Tektronix) to measure the peak-to-peak voltage across the LC-tank that was connected to a 500 Ω resistor load in their secondary circuit. To do this, they placed a voltage probe within the primary coil's electromagnetic field, to measure the induced voltage in the secondary LC-tank circuit, and they calculated the received power [69]. Pinuela *et al.* initially measured the induced current of their secondary using an Agilent N2783A current probe. However, they noted that the results did not reflect the true operation of their WPT, as current probes are not capable of measuring the induced current precisely in the presence of significant electromagnetic noise. Also, they could not measure the induced voltage (V_{ind}) using a voltage probe across the load, because the capacitance of the probe can detune the resonance of the receiver circuit. Therefore, they measured the efficiency of their WPT system using a thermal measurement scheme. This was done by measuring the temperature of the heat sink of the receiver coil, and the temperature of their metal film resistor load, by calculating the applied DC input power to their WPT system [81]. Russell *et al.* placed the resistor load of their secondary outside the primary field of their WPT system, and connected that load to the secondary coil via twisted-pair wires. They measured the DC voltage across the resistor load using a NI card (PCI-6025E) interfaced with LabVIEW [67]. Zhao *et al* built a LCWPT system for an epiretinal prosthesis application. They measured the induced voltage by connecting a voltage probe and a ground probe across the resistor load of the secondary circuit, all of which were within the primary coil's electromagnetic field. These probes were part of a single coaxial cable, which was connected to an oscilloscope [89]. Xu *et al.* built a WPT system for rodent (rat) applications, where their WPT system was based on four coils: driver coil, transmitter coil, receiver coil (secondary coil), and load coil (application load). Their load coil is intended for implantation subcutaneously within the dorsal region of a rat. They likely used a

coaxial cable to connect their load coil to an oscilloscope, to measure the peak-to-peak induced voltage of the load coil [71-72]. Dionigi *et al.* presented a secondary resonator based on a coaxial cable, which is suitable for WPT applications [90-91]. Their work indicates that coaxial cables can affect the magnetic resonance of WPT systems.

In this Chapter, we designed, constructed, and tested the WMS to avoid potential measurement errors inherent with coaxial cables, twisted-pair cables, or oscilloscope probes within the primary field. The WMS is connected to the output of the SIP to measure the rectified voltage (V_{rec}) of our LCWPT system.

5.2 Design Methodology for WMS

There are a few possible ways to measure the power transfer of the LCWPT systems. These include: (i) Using current probes to measure the current passing through the secondary load, R_L, while it is within the primary electromagnetic field; (ii) Using voltage probes to measure the voltage across the secondary load, R_L, while it is within the primary field; (iii) Placing the secondary load, R_L, outside the primary field and connecting it to the secondary coil via coaxial cable or twisted-pair wires. Then, measuring the current/voltage of the load R_L with oscilloscope probes.

In regards to approach (i) or (ii), Pinuela *et al.* found the probe's capacitance of 15 pF was enough to detune the secondary coil from resonance. They also concluded that current probes were not capable of measuring the current accurately in the presence of significant electromagnetic fields [81] due to noise. Hence, oscilloscope probes should not be used inside the primary field electromagnetic zone.

In regards to approach (iii), coaxial cables or twisted-pair cables can be used to place the load R_L farther away from the primary field, to measure the voltage across the load, or the current through the load, as Russell did in [67]. However, twisted/coaxial cables add an impedance to the secondary circuit. For example, coaxial cable has an impedance of 50 or 75 Ω depending on connector type. This impedance increase may cause impedance mismatch, leading to reflected power loss in the secondary coil.

The purpose of this Chapter is to measure the power transfer of the LCWPT systems precisely using a cable-free (wireless) approach. By avoiding the use of coaxial cables, twisted-pair wires

and current/voltage probes, we are able to avoid the problems described above. The design of the WMS is explained in Section 5.3.

5.3 WMS Design for LCWPT Systems

The main motivation for the WMS is to measure the power transfer of our LCWPT system. Given this goal, a set of design requirements for the WMS are established, and summarized in Table 12. Several design iterations were undertaken to create the WMS, to meet the design requirements and to achieve a robust measuring system. A high-level diagram of the WMS connected to the SIP is provided in Fig. 36. The requirement to minimize volume keeps the WMS compact and lightweight. It also minimizes physical interference when connected to the SIP/RID, and allows for easy placement and orientation within the primary coil. Ideally, the WMS should not disturb the primary magnetic field, and should not have significant effect on the system coupling. As noted in the methodology, a wireless (radio link) communication system has been designed into the WMS to transmit the measured data to an external base-station that records it. The WMS has an on-board CPU, radio and other electronics requiring power, which is supplied by a battery. This is needed since the WMS must operate independently of the WPT system, which it measures.

Several detailed points are made here regarding the WMS physical construction: (i) We used the nRF24LE1-F16Q24 microcontroller, since it is a low-power, wireless, system on-a-chip design that is suitable for RF applications [92]; (ii) The WMS is built on a four layer PCB that includes power (V_C) and ground (GND) planes in the middle, and two routing planes (top and bottom), for best performance in RF applications [93]; (iii) Use of surface-mount devices (SMD) of size 0201/0402 are ideal, since these sizes improve the RF performance and have good thermal properties [94-95]; (iv) We built a customized impedance matching circuit network for the RF antenna (FR05-S1-N-0-110) [96], by following the schematic circuit diagram of the QFN24 as described in [92]. (v) We avoid use of nonlinear components (such as voltage regulators or zener diodes) in the measurement stream. These components may affect the resonant frequency of the secondary circuit, as mentioned in [86]; (vi) We use a lithium-polymer (non-metallic) battery to power the WMS, since it is small and its composition is minimally disruptive to the primary field, which avoids the problems described in point (v). We cannot use induced power from the SIP/RID, since that power is variable during development experiments.

TABLE 12: DESIGN REQUIREMENTS FOR THE WMS

Design Requirement	Description	Value / Range [units]
Minimum volume	Minimize volume of WMS	1600 [mm^3]
Non-disruptive to induced field	WMS design should not interfere with resonance or coupling of the WPT	-
Measure induced voltage	Wide measurement range across the secondary load	0 - 63 [V]
Wireless data transmission	Transfer the measurement data by radio signal	4800 bits/sec
Self-powered	Powered by lithium-polymer battery	4.2 [V]
Disconnectable	WMS should be easily removable	two header connector

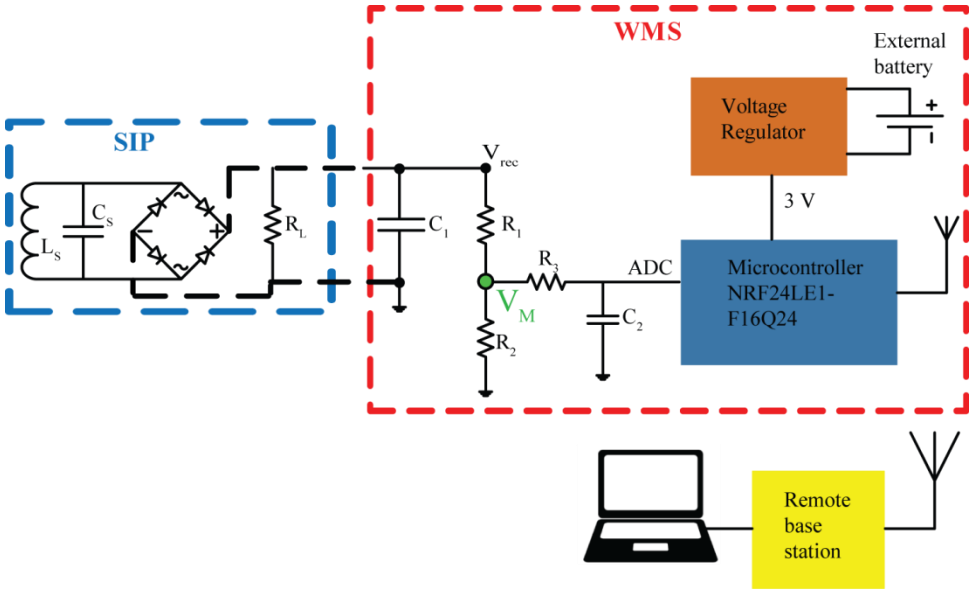

Figure 36: High-level diagram of the WMS configuration.

The design of the measurement circuit on the WMS is described here. The WMS measures the voltage developed across R_L on the SIP, which represents the application load. The value of R_L is pre-selected to ensure a good impedance match with the L_SC_S-tank and rectifier of the SIP/RID. The rectified voltage developed across load R_L can vary between 0 to 35 volts, depending on the experimental setup of the SIP [2].

The WMS employs a voltage divider when making measurements. This is needed since the voltage (V_M) measured by the microcontroller cannot exceed the internal reference value of the

analog-to-digital converter (ADC). The reference value is set by an internal bandgap of the microcontroller (nRF24LE1), which is nominally 1.2 V [92]. The system was simulated with Multisim software (National Instruments) to configure the resistor and capacitor values. Fig. 37 shows the Multisim model with voltage labels for the simulation results. The voltage source represents the induced voltage (V_{ind}) from the L_SC_S-tank of the SIP. It is assumed that the maximum output voltage of the L_SC_S-tank is 66 V (peak-to-peak), using a resistor load R_L of 5 kΩ, and the parameter values as listed in Table 13. The voltage points at V_{rec}, V_M and V_{out} of the WMS simulation are plotted in Fig. 38.

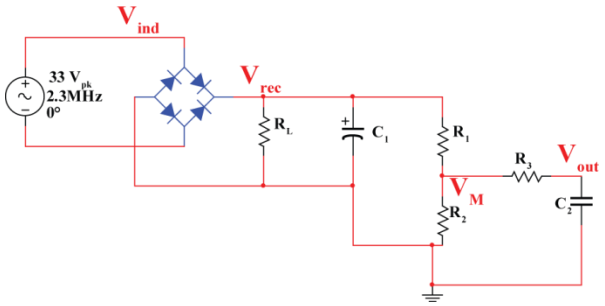

Figure 37: Multisim model of the SIP connected to the WMS.

The measured voltage (V_M) is digitized using a 12-bit setting on the ADC relative to the internal reference value of 1.2 V. The values of the voltage divider resistors R_1 & R_2 control the resolution of the range of the measured voltage (V_M), allowing the WMS to measure DC voltages up to 62.4 V, as explained in equation (36). We can ignore the voltage drop over the filter (R_3 & C_2), as the resistance value of R_3 is small compared to R_2, as shown in Table 13. We can back-calculate the rectified voltage (V_{rec}) over the resistor load R_L as follows:

$$V_M = V_{ind}\frac{R_2}{R_1 + R_2}$$
$$V_{rec} = V_M\frac{R_1 + R_2}{R_2} \qquad (36)$$
$$V_{rec} = \frac{V_{A/D}}{2^{12} - 1}V_{Ref}G$$

where,

$V_M = \frac{V_{A/D}}{4095}V_{Ref}$,

G: Voltage divider factor ($\frac{R_1+R_2}{R_2}$), it is 52,

V_{Ref}: Internal reference (1.2V).

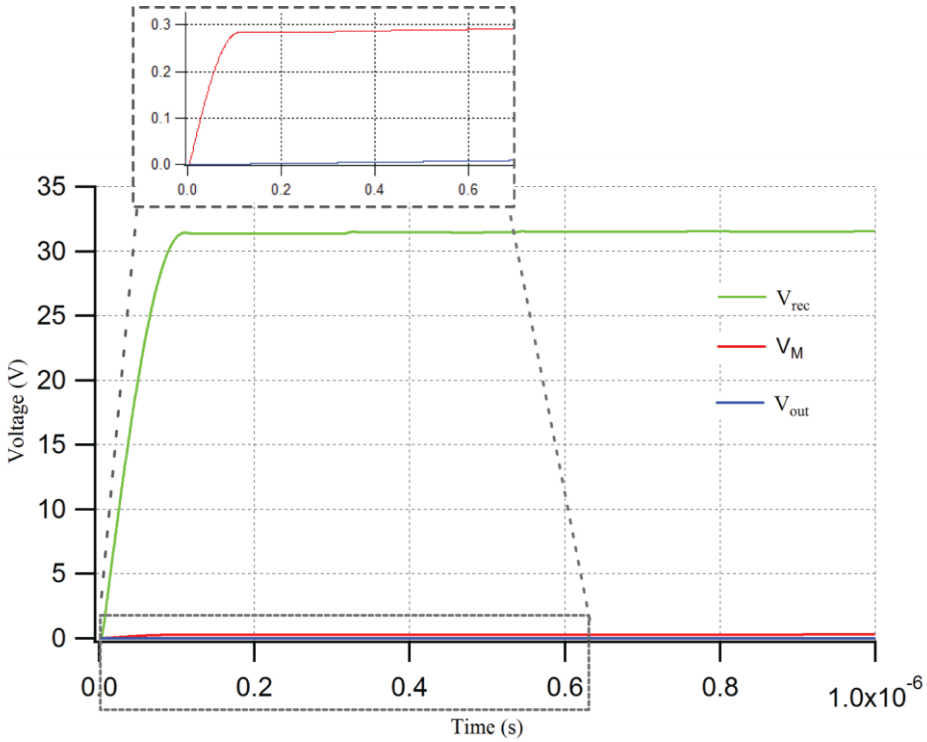

Figure 38: Voltage traces of the WMS simulation.

Table 13 lists the performance parameters of the final WMS design. The WMS circuit schematic was designed using Altium CAD software and is shown in Fig. 39. A radio communication protocol is built into the Nordic platform and uses a proprietary handshaking network protocol to transfer the measured voltage (V_M) in digital format. The microcontroller chip on the motherboard is programmed by compiling the program on a computer, and downloading it to the chip using a USB-connected interface board.

The magnetic resonant properties of our LCWPT system were evaluated with and without the WMS attached. This was done by first measuring the resonant frequency of the SIP L_SC_S-tank, as listed in Table 8. The resonant frequency of 4MF was 2.057 MHz when we measured the resonant frequency of the SIP alone (without connecting the WMS). When we measured the resonant frequency of the SIP with the WMS attached, we observed a resonant frequency 2.067 MHz with the 4MF configuration. This difference of frequency is only 10 kHz (0.5%), which shows that the WMS does not cause a large shift in the resonant properties for LCWPT systems.

TABLE 13: FINAL DESIGN PARAMETERS FOR THE WMS

Design Parameter	Description	Design Value [units]
Overall size	$L \times W \times H$	$35 \times 18 \times 1$ [mm]
Total weight	The weight of WMS	3 [g]
C_1	Smoothing capacitor	0.1 µF
R_3 & C_2	Filter	1 kΩ & 2 nF
R_1 & R_2	voltage divider resistor	510 & 10 kΩ
Nonlinear component	Power the voltage regulator externally	-

5.4 WMS Experimental Results

The physical WMS was constructed and a set of experiments were conducted to test its performance. First, we examined the effect of measuring the rectified voltage (V_{rec}) across the secondary load (R_L) using the WMS, and compared it to measurements using a physically connected coaxial cable. Measurements using the WMS are described in Section 4.5. The measurements using the coaxial cable were performed with one end of the cable connected to the output of the rectifier on the SIP, and then running the remaining length of the coaxial cable outside the primary coil. The other end of the coaxial cable was connected to the secondary load (R_L), where the rectified voltage (V_{rec}) was measured using the high voltage probe (measured outside the primary coil). We varied the shape and orientation of the coaxial cable within the primary magnetic field using four shapes/orientations which were: straight cable (parallel to magnetic field), 45° titled cable (45° to magnetic field), S-shape bent cable (in plane parallel to magnetic field), and circle-shape bent cable (in plane parallel to magnetic field). Table 14 summarizes the measured voltage and the received power using both the WMS and the four coaxial cable configurations. All tests were done using the *air core* configuration (SIP) over four days, placed at the center of the cage, using a 2.5 A current (sinusoidal, peak-to-peak) applied to the primary coil. We observed that the measured value of the rectified voltage (V_{rec}) using the four shapes of the coaxial cable was not consistent from shape-to-shape, and also not consistent from day to day. However the measured values from the WMS were very consistent. The

measured values of the V_{rec} using the four shapes of the coaxial cable were higher than the values obtained using the WMS by 5 – 28%.

Note: It is not practical to place the voltage probe or current probe directly into the primary field, since the probes will pick up significant noise, and will affect the magnetic resonance of the WPT system, as explained in Section 5.2. Hence the R_L resistor cannot reside on the SIP if using direct cable-based probe measurements.

We also investigated our LCWPT behaviour using different types of battery to power the WMS. Since the WMS must provide reliable measurements over time, its power must be supplied by a battery to make its operation independent of the SIP performance. We tested the use of AA, coin cell, and lithium-polymer batteries. We found that the primary circuit of the WPT system draws more voltage and current from the DC supply when using the AA and coin cell batteries, in comparison to the lithium-polymer battery. This is likely due to the metallic components of the AA or coin cell battery, which produce a load in the electromagnetic field. In addition, metallic objects near the field affect the inductance of the primary coil to shift the operating point (resonant frequency) of the Class-E power amplifier [97]. The Class-E power amplifier compensates for this load effect by drawing more DC current to maintain application of the sinusoidal current to the primary coil. The extra draw on the DC power supply of voltage and current when using the AA or coin cell batteries was 1 – 2 V and 0.1 – 0.3 A.

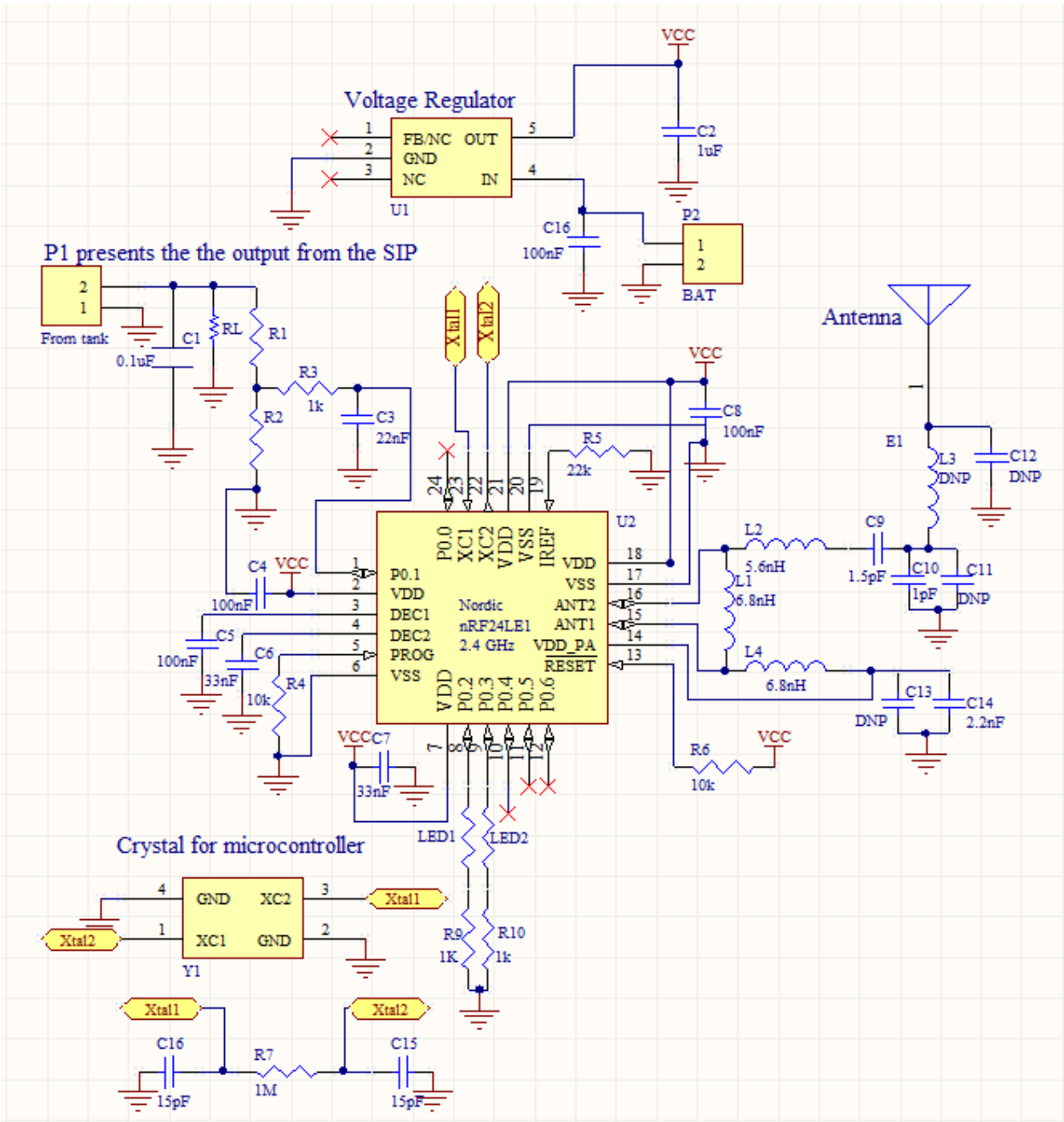

Figure 39: Schematic diagram of the WMS.

TABLE 14: MEASURED THE V_{REC} AND RECEIVED POWER OF *AIR CORE* USING WMS AND THE FOUR SHAPES OF THE COAXIAL CABLE

Measuring approach		Day 1	Day 2	Day 3	Day 4
WMS	V_{rec} (V)	17.06	17.03	17.06	17.03
	P(mW)	58.2	58.04	58.2	58.04
Straight coaxial cable	V_{rec} (V)	18.7	18.3	17.85	18.02
	P(mW)	69.9	65.7	63.72	64.9
45° tilted coaxial cable	V_{rec} (V)	18.03	17.52	17.2	17.3
	P(mW)	65.1	61.4	59.2	59.9
S-shape coaxial cable	V_{rec} (V)	21.3	20.2	18.9	19.1
	P(mW)	90.73	81.6	71.5	72.9
Circle-shape coaxial cable	V_{rec} (V)	21.8	21.1	19.5	20.02
	P(mW)	95	89	76.1	80.2

5.5 Discussion

The WMS communicates wirelessly via radio link to a receiving base station that is connected via USB to a laptop that collects performance data of the WPT system under test. The utility of the WMS approach is that it overcomes many of the problems that result when using directly connected coaxial cables or voltage/current probes to measure the performance of the secondary circuit. In our earlier work, we had measured the rectified voltage (V_{rec}) using a coaxial cable connected to an external (outside the primary field) load (R_L), however, those measurements were plagued by offset and noise problems. This lead to the development of the WMS system presented in this paper, where reliable performance measurements were needed at various orientations and positions of the SIP, within the primary field. Such measurements of the SIP using a tethered coaxial cable produce inconsistent results. By using the WMS, measurements are consistent (within 0.2%) from day-to-day as shown in Table 14, whereas those from the cables varied by 5% from day-to-day. Furthermore when the same length cable was bent in different shapes, measurements of the RID (with all other parameters fixed) varied by 5 – 27%. This variation is because we took down the experimental setup each day after conducting the measurements. The primary coil (cage), the power amplifier, the oscilloscope, current probe, the

signal generator, and the base station remained in the same place each day. The secondary circuit (SIP), voltage probe, and the four shapes of the coaxial cable had to be placed at the beginning of the experiment each day, hence the slight change in values for using four shapes of the coaxial cable in Table 14.

Note that the WMS is not able to measure the sinusoidal induced (AC) voltage of the L_SC_S-tank circuit because of a floating ground issue. This occurs since the measured voltage (V_M) over the voltage divider (Fig. 36) will be a floating signal with respect to the ADC of the microcontroller. The WMS was only designed to measure the rectified DC voltage (V_{rec}), as shown in Fig. 36. When developing the WMS, we wanted a rough check of the WMS DC measurement values. We did this with a coaxial cable to measure the AC voltage across the L_SC_S tank, even though we acknowledge the problems of Section 5.4 and Table 14. We placed a 5 kΩ (R_L) resistor outside the primary cage, and connected it to the L_SC_S-tank using a straight coaxial cable. We measured the induced voltage across R_L using a voltage probe connected to an oscilloscope. We found the induced AC voltage was 54.2 V (peak-to-peak) when driving the primary coil with (I_P) 2.5A (peak-to-peak). An AC value of 54.2 V corresponds to 17.3 V DC (rectified voltage, V_{rec}), which approximately matches the measurements using the WMS, as shown in Table 14.

In general, the WMS system described here could be used for measurement of induced DC voltage of various WPT systems. This could be done, by modifying the WMS configuration of the voltage dividers (R_1 and R_2) and by modifying R_3 and C_2 (filter) to measure the induced voltage and the received power for any WPT application.

Chapter 6: Maximizing Efficiency of LCWPT Systems

6.1 Design Methodology for LCWPT

We reported the development of a novel configuration of the secondary circuit employing four ferrite rods placed at edge corners of a PCB and oriented at 45° within the secondary coil. This configuration is denoted as 4MFA, which improved power transfer at most orientations with respect to the primary electromagnetic field. The maximum efficiency achieved using 4MFA in the previous design of LCWPT was 1.5%, as described in Chapter 4. A further limitation of our previous LCWPT system is poor efficiency because of high heat dissipation and losses in the primary and secondary circuits. High efficiency is of great importance for the WPT in biomedical applications. The LCWPT systems are recommended to have a good efficiency to minimize the electronic heating problem that represents a major concern for any implantable device [61-62]. Our focus in this Chapter is on improving the efficiency of the LCWPT system.

A number of researchers improved the efficiency of the LCWPT systems for rodents using a four coil system, as described in Section 4.1. Our LCWPT is based on a simple two coil system, namely the primary coil (L_P) and the secondary coil (L_S). In this Chapter, we rebuilt our rectangular-helical primary coil (L_P) to improve its quality factor (Q_P). The size of the new stationary primary coil is 250 × 120 × 45 mm^3 (length × width × height), as shown in Fig. 40. It is wrapped around the mouse housing cage that is needed to meet the minimum animal care standards for mice [1-2]. We redesigned the whole LCWPT system using mathematical analysis to minimize the losses and improve the efficiency. We used the *air core* and the 4MFA configurations to investigate the performance of the improved LCWPT for rodents. In this Chapter, the received power by the SIP and the efficiency of the LCWPT are investigated at the middle and the edge of the cage.

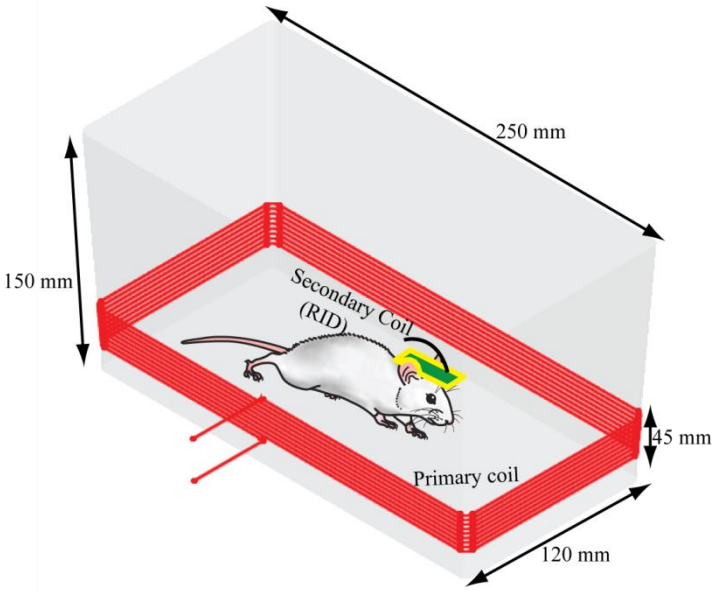

Figure 40: Redesigned wrapping primary coil around a small mouse housing cage for rodents.

6.2 Design LCWPT

The coupling coefficients in the biotelemetry applications of the LCWPT are restricted by the separation and the size of the coils. The low value of the coupling coefficient of the LCWPT causes low efficiency of the system [62, 87]. The efficiency of a two coil system using magnetic resonance is a function of the quality factor of the primary coil (Q_p) and the secondary coil (Qs), and the coupling coefficient (k). The main goals for improving the efficiency of LCWPT systems are increasing the quality factor of the coils and minimizing the losses of the LCWPT systems [87]. The efficiency of a two coil system using magnetic resonant coupling is approximately derived as [62, 90]:

$$\eta = \frac{k^2 Q_P Q_S}{\left(1 + \sqrt{1 + k^2 Q_P Q_S}\right)^2} \tag{37}$$

The coupling coefficient is a function of the dimensions of the coils, the orientation with respect to each other of the two coils, the number of turns of the coils, the distance between the two coils, and the magnetic core that if the coils are wound around [98-100]. The coupling coefficient was calculated as a function of the dimensions of the two coils and the distance between the two coils (two parallel single-turn coils), it is given as [99]:

$$k = \sqrt{\frac{4a_P a_S}{(a_P + a_S)^2 + d^2}} \tag{38}$$

where, *d* is the separation distance between the coils.

Improving the quality factor of the coils and the different type of the losses in the LCWPT systems are discussed in this section. There are two sources of losses in the WPT systems which cause a decrease in the efficiency of power transfer. The first source is the effect of the reflected impedance from the secondary circuit over the primary circuit [60]. There are four possible compensation topologies, which are PP, PS, SP and SS, where these four topologies have different values of the reflected impedances. The primary compensation capacitors for the reflected impedances are analyzed in this section. The second source is radiation and ohmic losses. The radiation loss is proportional to the fourth power of the operating frequency and the ohmic loss is nearly proportional to the square root of the frequency [62, 100]. The ohmic losses are caused by skin and proximity effects, which are the dominant parts of losses. The radiation loss is negligible in this type of WPT system (non-radiative) because the ratio of the perimeter of the primary and secondary coil to the wavelength of the electromagnetic field is usually less than one-tenth. Our WPT system is based on the near field region operation [100-101].

6.2.1 Reflected impedance

The reflected impedance is a measure of how much of the actual load of the secondary circuit is seen by the primary coil (L_P). It is a function of the mutual inductance (M_{SP}) between the coils, the operating frequency, and the distance between the coils [102-103]. The mutual inductance and the reflected impedance increase when the coils are closer to each other [102]. The reflected impedance causes: (1) a shift of the resonant frequency of the WPT system; (2) changing in the amount of applying current (I_P) to the primary coil (L_P), which is affected by the position of the secondary coil; and (3) an increase of the required VA rating of the DC power supply [103-104]. The primary capacitor (C_P) is designed to compensate both the primary coil and the reflected impedance to achieve the magnetic resonance. At the magnetic resonance, the zero phase angle of the primary circuit occurs and the maximum power transfer is achieved with minimum VA rating of the power supply [60].

Fig. 41 shows the four basic topologies (SS, SP, PP and PS) for the LCWPT systems and the primary circuits with the reflected impedance. The primary series compensation topologies (SP and SS) are independent of the load (R_L), which is a desirable property particularly when the loading profile of WPT system is variable [105]. However, the primary parallel compensation topologies (PP and PS) depend on the coupling coefficient (k) and load resistance (R_L) [57]. Since the required primary compensation capacitance of the SP topology depends on the coupling coefficient (k), the use of SS compensation is recommended for a high coupling WPT system for moving objects (secondary coil; like vehicles) [60, 106]. Table 15 lists the required primary compensation capacitance of the four topologies and the value of the reflected impedance at the magnetic resonance [60, 105]. For a general analysis, a normalized primary capacitance is defined as the primary compensation capacitance divided by the primary capacitance, which is determined by equation (39), as listed in Table 15.

$$C_{Pn} = \frac{C_P}{\frac{C_S L_S}{L_P}} \tag{39}$$

$$w_o = \frac{1}{\sqrt{C_S L_S}} = \frac{1}{\sqrt{C_P L_P}} \tag{40}$$

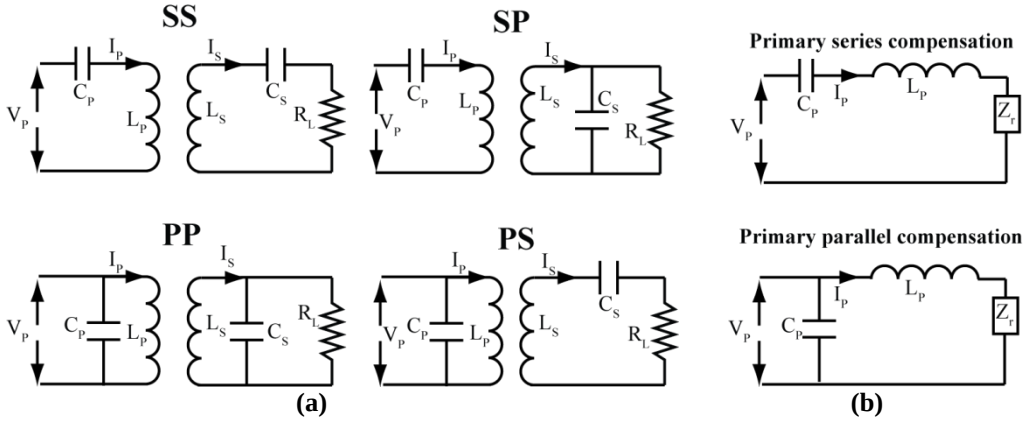

Figure 41: Modelling WPT system of four topologies; (a) four topologies, (b) primary circuits with reflected impedance.

TABLE 15: PRIMARY CAPACITANCE (C_P), NORMAL PRIMARY CAPACITANCE (C_{pn}) AND REFLECTED IMPEDANCE (Z_R) OF THE FOUR TOPOLOGIES

Topology	Primary capacitance	Normal primary capacitance	Reflected impedance at resonance
SS	$C_P = \frac{1}{w_o{}^2 L_P}$ (41)	$C_{Pn} = 1$ (45)	$Z_r = \frac{w_o{}^2 M_{SP}{}^2}{R_L} + j\,0$ (49)
PS	$C_P = \frac{L_P}{(\frac{M_{SP}{}^2 w_o{}^2}{R_L})^2 + w_o{}^2 L_P{}^2}$ (42)	$C_{Pn} = \frac{1}{Q_S{}^2 k^4 + 1}$ (46)	
PP	$C_P = \frac{(L_P - M_{SP}{}^2/L_S)}{(\frac{M_{SP}{}^2 R_L}{L_S{}^2})^2 + w_o{}^2 (L_P - M_{SP}{}^2/L_S)^2}$ (43)	$C_{Pn} = \frac{1-k^2}{Q_S{}^2 k^4 + (1-k^2)}$ (47)	$Z_r = \frac{M_{SP}{}^2 R_L}{L_S{}^2} - j\,\frac{w_o M_{SP}{}^2}{L_S}$ (50)
SP	$C_P = \frac{1}{w_o{}^2 (L_P - M_{SP}{}^2/L_S)}$ (44)	$C_{Pn} = \frac{1}{1-k^2}$ (48)	

The value of the coupling coefficient of biomedical devices ranges from 0.1% to 10% [1-2, 87] and our application device (stimulator/EEG) has a variable loading (impedance) profile, as described in Section 4.7. In order to investigate the effects of the coupling coefficient and the load on the primary compensation capacitance of the four topologies, the parameters of the primary and the secondary coils, listed in Table 16, are used to investigate the LCWPT performance. Fig. 42 shows the required primary capacitance (C_P) and the normal primary capacitance (C_{Pn}) versus the coupling coefficient (k). The values of the primary capacitance (C_P) for parallel compensations (PP & PS) decrease with increasing the coupling coefficient. The required parallel compensation capacitances at 10% of the coupling coefficient (k) drop by 100 pF from the required value at 0.1% of k, as shown in Fig. 42 (a). The normalized primary capacitance of using the SS topology is constant, as shown in Fig. 42 (b). At 10% of the coupling coefficient, the normalized primary capacitance of using the SP topology increases by 1% from the value of the normalized primary capacitance at 0.1% of k. However, the normalized primary parallel capacitances (PP and PS) at 10% of k decrease by 12% from the value at 0.1% of k, as shown in Fig. 42 (b). Fig. 43 shows the required primary capacitance (C_P) versus the resistor load (R_L). The primary capacitances of using the series compensations (SS & SP) are constant with changing the resistor load (R_L). However, the primary parallel compensation capacitances (PP & PS) decrease when increasing the resistor load (R_L). This concludes why the primary series compensations (SS & SP) are preferred for variable load and low coupling coefficient of LCWPT systems.

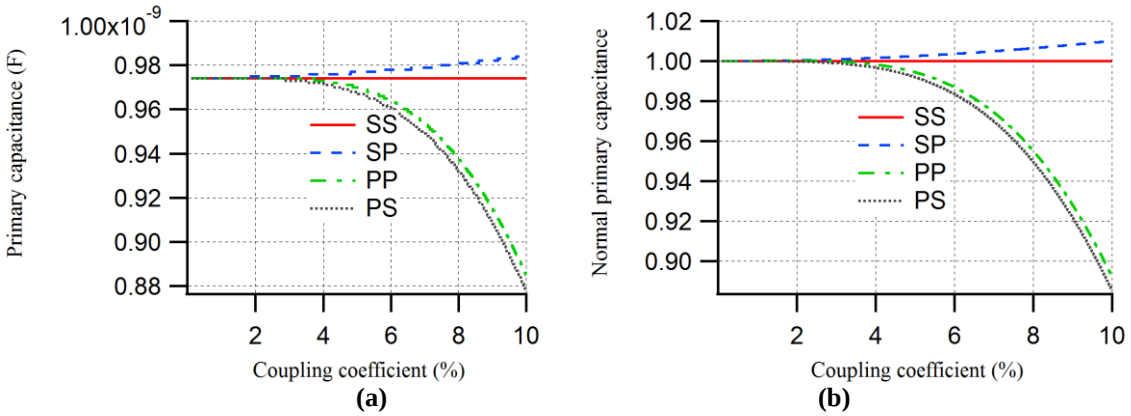

Figure 42: Primary capacitance of the four topologies versus the coupling coefficient; (a) primary compensation capacitance, (b) normalized primary capacitance.

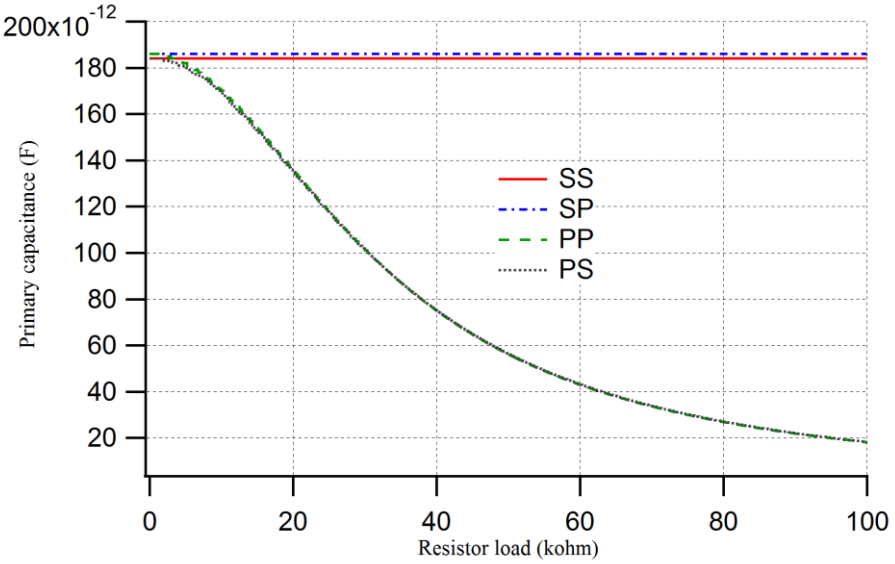

Figure 43: Primary capacitance of the four topologies versus load (R_L).

Since the mutual inductance (M_{SP}) of the LCWPT systems is very small and the resistor load of the secondary circuit (R_L) is in the range of 5-10 kΩ [1-2, 53], the magnitude of the reflected impedance (Z_r) at the resonance of the secondary series compensations (SS & PS) is negligible. Moreover, there is no imaginary component of the reflected impedance at the resonance of using the secondary series compensations, as shown in Table 15. However, the reflected impedance at the magnetic resonance of using the secondary parallel compensations (PP & SP) can be considered with respect to the used R_L, and it has a small imaginary value that can be disregarded. With respect to Figs 42-43 and Table 15, the primary series compensation (SS/SP) is suitable for our LCWPT system, where the primary coil (L_P) can be tuned out independent of either the magnetic coupling (k) or the load (R_L). The choice between the two primary series

compensation strategies (SS and SP) would depend on various factors such as efficiency, its tolerance to variable frequencies, and the desired power levels of operation, as described in Sections 6.4 and 6.5.

6.2.2 Designing High Quality Coils

The coils used in LCWPT for biomedical applications are desirable to have a low ESR to reduce the power dissipation. At higher frequencies, both skin effect and proximity effect increase the ESR and cause additional power dissipation. The ESR is given by [87]:

$$ESR = \frac{R_{AC}}{(1 - w^2 L C_{self})^2} \tag{51}$$

where, R_{AC} is the AC resistance of a coil, C_{self} is the equivalent parasitic capacitance of a coil. The AC resistance is derived as [87, 99]:

$$R_{AC} = R_{DC}(1 + \frac{f^2}{{f_h}^2}) \tag{52}$$

where, R_{DC} is the DC resistance of the coil, and f_h is the frequency at which power dissipation is twice the DC power dissipation and is given by [73, 87]:

$$f_h = \frac{2\sqrt{2}}{\pi {r_s}^2 \mu_o \sigma \sqrt{N_t N_{St} \upsilon \beta}} \tag{53}$$

where, r_s is the radius of an individual strand, μ_o is the permeability of the conductor, σ is the conductivity of the conductor, N_t is the total of turns, N_{st} is the number of strands, υ is a parameter defined to characterize a coil's geometry properties, and β is the area efficiency defined as the ratio of the total conducting area over the cross section of the winding. To optimize the power efficiency of the LCWPT systems, f_h should be as high as possible. In practical coil design, the power dissipation from the proximity effect is not the major concern when the f_h is higher than the operating frequency [87].

The efficiency of the two coils of the LCWPT systems is proportional to the quality factors of the coils (Q_P & Q_S) and quadratic of the coupling coefficient (k), as explained in equation (37). While the coupling coefficient is limited in LCWPT systems, the main focus is increasing the Q of the coils to improve the efficiency. The definition of the Q for the WPT systems agrees with

the intuition that a high quality resonator is one that does not dissipate much energy at resonance [107], which is a very important requirement for implantable biomedical devices.

The quality factor is a function of parameters and properties of the coils. These parameters need to be investigated to achieve a high *Q* factor for the primary and secondary coils (Q_P & Q_S). They are explained as follows: (1) Wire property: Litz wires are commonly used to reduce the AC resistance of wire (R_{AC}). Analytical models of winding losses using the Litz wire are presented in [108-109]. There are parameters that are used to determine the type of Litz wire, such as the operating frequency, diameter, and resistance [110]. For our purpose of the LCWPT, the range of our operating frequency is from 1 MHz to 3MHz, where no biological effects have been reported, and tissues have lower absorption for low-frequency RF signals compared to high-frequency signals [111]. This restricts our choice of wire from AWG40 to AWG48 [112]. (2) Optimal frequency of the quality factor: Yang *et al.* characterized the quality factor of the coil versus the operating frequency, where f_{peak} represents the frequency at which a coil has maximum quality factor [87]. The *Q* of the inductor is a function of the frequency, and the band width of the quality curve that is defined by f_h, as shown in equation (54). To reduce the AC resistance (R_{AC}) of the coil, f_h should be kept sufficiently high, as shown in equation (52). The quality factor is given by [87]:

$$Q(f) = 2\pi f \frac{1-(\frac{f}{f_{self}f})^2}{R_{DC}(1+(\frac{f}{f_h})^2)} \tag{54}$$

where, f_{self} is the self-resonant frequecy of an inductor. To obtain the f_{peak}, equation (54) is differentiated and set to zero. The f_{peak} is approximately given as [87]:

$$f_{peak}{}^2 \approx f_h{}^2 || (f_{self}{}^2/3) \tag{55}$$

The heat dissipation in the biotelemetry applications represents a big concern for biotelemetry applications, so it is desirable to operate near the f_{peak} [87]. Also, Hu *et al.* recommended the secondary circuit to operate near to the f_{peak}, because the secondary circuit is too sensitive to the circuit parameter changes at the f_{peak} [113]. The bandwidth (BW) of the quality factor curve is defined in terms of its 3 dB attenuating of Q_{peak} [87]. As an example, Fig. 44 shows the quality factor curve of the secondary coil of the 4MFA configuration. The BW is defined as:

$$BW = \frac{f_{peak}}{Q} = f_2 - f_1 \tag{56}$$

$$f_1 = f_{peak}\left(\sqrt{1 + \frac{1}{4Q^2}} - \frac{1}{2Q}\right) \tag{57}$$

$$f_2 = f_{peak}\left(\sqrt{1 + \frac{1}{4Q^2}} + \frac{1}{2Q}\right) \tag{58}$$

where, f_1 and f_2 are the lower and upper cut-off frequency. (3) Number of strands: the number of strands of a coil controls the bandwidth of the quality curve and the f_{peak}. The Q_{peak} becomes high at low frequency (0.1-2 MHz) when the number of strands increases [87]. This is due to the f_h increasing while decreasing the number of strands (N_S), as shown in equation (53). The DC resistance (R_{DC}) of a coil is much higher when fewer strands are used per winding [98]. (3) Number of turns: RamRakhyani *et al.* found that the Q of a coil increases when the number of turns per layer is less than 10 [112].

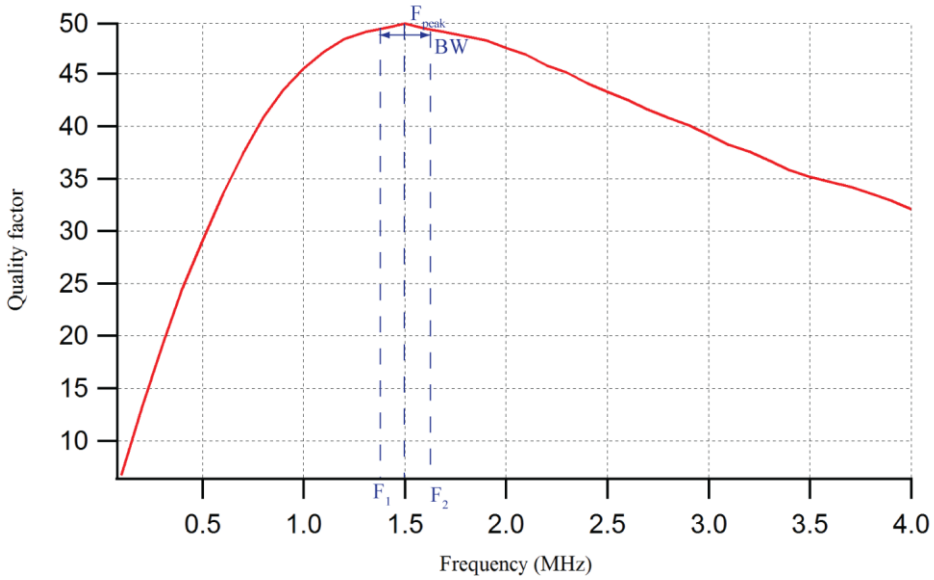

Figure 44: Quality factor the 4MFA configuration versus frequency.

6.3 Redesign Power Amplifier and Primary Coil

In order to transfer the power wirelessly, a sinusoidal alternating electromagnetic field is needed to be generated by the primary coil (L_P). Signal generators are not sufficiently strong to drive the primary coil directly, hence a power amplifier is needed to generate a high sinusoidal

current (I_P). The intensity of the electromagnetic field (B) is related to the amplitude of the applying current through the primary coil (L_P). The generated magnetic flux density from a solenoid coil is given as [51]:

$$\vec{B} = \frac{\mu_o N_P I_P \times \hat{x}}{l} \tag{59}$$

where, l is the length of the coil, and $\hat{x}$ is a unit vector of the transmission distance along x-axis.

The inductance of the primary coil is compensated by either a series or a parallel capacitor. Both ways have their benefits and drawbacks, as explained in Section 6.2.1. The use of the primary series compensation in the amplifier circuit delivers a high applying current (I_P) to the primary coil but lower applied voltage. The primary parallel compensation in the amplifier circuit maintains the need for a high output voltage of the amplifier, but the amplifier output current (I_P) is lower [88]. The Class-E amplifiers are fitted with a double tuned circuit. The series resonance Class-E amplifiers feature a series tuned primary coil (L_P) with a second capacitor in parallel with a switch. This offers an elegant solution as it combines the benefits of high voltage operation of a parallel resonance with the high current operation of a series resonance [88, 114]. This combination in the series resonance Class-E amplifier gives an advantage of the both the voltage and current ratings are designed to meet industrial regulation with the low cost of commercially available components [103]. The parallel capacitor bypasses the switch and takes up the larger part of the coil current (I_P), and the series capacitor acts as an AC coupling capacitor that separates the switch from the coil [114].

Fig. 45 depicts the schematic diagram of series resonance Class-E power amplifier that resonates in series. It consists of a DC supply (V_{CC}), a DC-feed inductor (L_{Choke}), a switch (MOSFET), the ESR of the windings of the primary coil (R_P), a parallel capacitor (C_{par}) with the MOSFET, and a series resonant circuit (L_P & C_{ser}). The power losses of the amplifier are minimized at the operating frequency that is called the Class-E point or Class-E mode [97-114].

The efficiency is maximized by minimizing power dissipation of the Class-E power amplifier. This is achieved when the MOSFET voltage (V_{DS}) or the voltage across the capacitor (C_{par}) is zero, and its derivative should be zero at switch closure; otherwise there will be power losses due to the simultaneous large current through and voltage across the MOSFET [97, 115-116]. The operation of the Class-E power amplifier at the Class-E mode is described as follows. The output

current (I_P) in the L_P and C_{ser} is sinusoidal with a frequency equal to the frequency of the MOSFET drive (V_G). When the MOSFET switch is closed, the L_P and C_{ser} supply current back to the MOSFET (I_P is negative), no current flows through C_{par} and the voltage across the MOSFET switch is zero. The series resonant tank (L_P and C_{ser}) continues supplying current (I_P is still negative), and this current also flows through C_{par} resulting in a positive voltage across the switch when the MOSFET switch opens. When the current in the L_P and C_{ser} reverses (becomes positive), the charge on C_{ser} supplies the current (I_P) and reduces the voltage across the MOSFET. When the voltage across the MOSFET becomes zero, the switch is closed and the cycle is repeated. At the operating frequency (Class-E point), the phase angle between the output voltage and output current (I_P) of the amplifier is close to 90°, and the voltage across the MOSFET (V_{DS}) is zero with zero slope. This ensures that no large peak currents in the switch and the switching losses of the Class-E power amplifier are minimized [97]. A parallel diode is added between the drain and source of the MOSFET, as shown in Fig. 45. The antiparallel diode in the MOSFET turns on when the voltage crosses zero, before the oscillation waveform reaches its minimum. This diode protects the MOSFET from damage. This configuration is referred to as suboptimum operation [1-2].

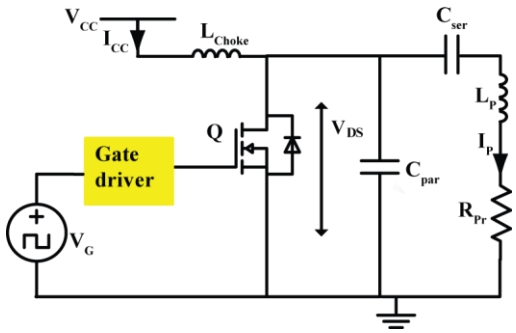

Figure 45: Class-E power amplifier (series resonance).

Class-E power amplifiers have many parameters and variables that affect the performance of the WPT systems. The derivations of design equations are carried out for achieving the Class-E operation, which are described as follows. (1) The duty cycle (D) of the signal generator: the required DC supply voltage (V_{CC}), increases when the duty cycle (D) decreases. Also, decreasing the duty cycle results in a reduction of DC supply current (I_{CC}) and vice versa. Since the input DC power to the power amplifier is given by $P_{in}= I_{CC}\cdot V_{CC}$, the DC supply voltage (V_{CC}) must be increased/decreased for a fixed applying current (I_P) to the primary coil (L_P) and a fixed output power (P_{out}). This presents a problem in low voltage battery operated systems [115, 117]. It is

preferred to set the switch duty cycle (D) as 50%, to draw reasonable VA ratings from the DC supply [97, 114-115] and to guarantee the voltage drain of the MOSFET (V_D) will reach its minimum before the zero crossing of the I_P [115]. (2) The inductance of the choke coil (L_{Choke}) is large enough to neglect its current ripple. It is chosen to be three to ten times greater than L_P [97, 115]. (3) The MOSFET ON resistance is low enough, so the current and voltage waveforms remain almost unchanged [115]. It is recommended to use the MOSFET (IRF840) that supports fast switching; a V_{DS} of up to 500 V and an I_{DS} of up to 8 A [115-116]. (4) A suitable gate driver guarantees ruggedness and matching rise and fall time of the MOSFET and provides a high output current, so the gate driver (MIC4421) is recommended [1-2, 83]. (5) The parallel capacitor (C_{par}): its value is affected by the reflected impedance and a parasitic capacitance of the MOSFET that is the drain-source (C_{DS}) capacitor of the MOSFET [112, 118]. (6) The series capacitor (C_{ser}) value depends on the properties (inductance, Q, ESR) of the primary coil (L_P) [112]. (7) The quality factor (Q_P) of the primary coil: the operating frequency of the Class-E power amplifier is dependent on the quality factor of the primary coil, as shown in equations (60-61). A number of researchers characterized the Class-E performance versus the quality factor of the primary coil as follows. The voltage across C_{par} does not return to zero and additional harmonics are generated along with the fundamental component of I_P when the value of the quality factor (Q_P) is too low. This performance of the Class-E power amplifier is denoted as too much damping. With too high Q_P (too little damping), the V_{DS} swings below zero and does not damp sufficiently. This leads to placing the MOSFET in the inverted mode which causes the switch voltage (V_{DS}) to have a negative peak below zero [97, 115, 120]. Under these conditions, the performance of the Class-E causes high power dissipation and breakdown of the MOSFET [120-121]. Since the quality factor of the coil is a function of the frequency, a suitable Q_P is required for minimum-loss operation of the Class-E power amplifier. It is recommended to use a high Q (> 80), with low ESR of the primary coil [51]. (8) The primary coil (L_P) increasing the turns of the L_P with reducing ESR will accomplish a high Q_P. This is achieved by using Litz wire to guarantee low ESR with more turns [97, 112]. A solenoid coil configuration is devised to meet care standards for rodents [1]. Our previous solenoid coil configuration with a separation of 15 mm between the windings generates a uniform electromagnetic field within its volume [1-2]. The inductance and the quality factor of the previous coil are 27 μH and 60, respectively. The new designed solenoid (primary) coil is wrapped around the same cage with a separation of 5 mm (as

minimum) between the windings to minimize the stray capacitance between the windings and improve the Q_P, as shown in Table 16. The height of the new wrapped coil occupies 45 mm of 150 mm of the cage to be able to monitor the rodent activity, as shown in Fig. 40.

We used COMSOL to compare the magnetic field distribution surrounding the 4MFA configuration of using the primary coil of the 15 mm and the 5 mm separation windings. A simulated current of 2.5 A (peak-to-peak) is applied through the primary coil windings. Fig. 46 shows an *x-y* plane plot of the magnetic flux density distribution produced by the primary coil, at the middle of the cage. The line AB shown in Fig. 46, which passes through two ferrites on the *x-y* plane, is used to plot the flux density. The magnitude of the flux density crossing the secondary coil at 0° orientation, along line AB is plotted in Fig. 47. As seen from Figs 46-47, the magnetic flux density produced by the primary coil using the new design (L_P of 5 mm separation windings) is higher than when using the previous (L_P of 15 mm separation windings). Hence, the induced voltage will be boosted and the received power by the secondary circuit will increase.

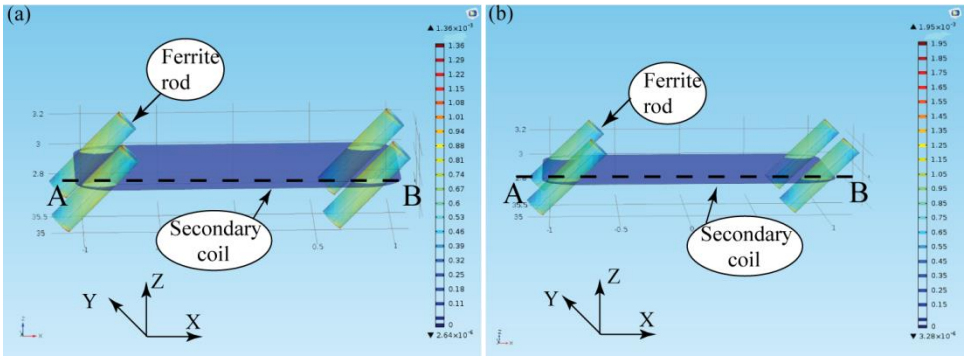

(a) **(b)**

Figure 46: Magnetic flux density; (a) plotted on the *x-y* plane within separation winding of 15 mm, (b) plotted on the *x-y* plane within separation winding of 5 mm.

The frequency of the Class-E power amplifier is dependent on the quality factor of the load network (primary coil) [97, 114-118, 120-121]. The resonant operating frequency (f) of the LCWPT is chosen as 1 MHz, with respect to the value of the Q_S & Q_P and the biomedical application limits [2, 118]. The numerical equations of Sokal are used to obtain the C_{ser} and C_{par} that are given as [120]:

$$C_{par} = \frac{1}{2\pi f R_{Pr} 5.447} \tag{60}$$

$$C_{ser} = \left(\frac{1}{(2\pi f)^2 L_P}\right)\left(1 + \frac{1.42}{Q_P - 2.08}\right) \tag{61}$$

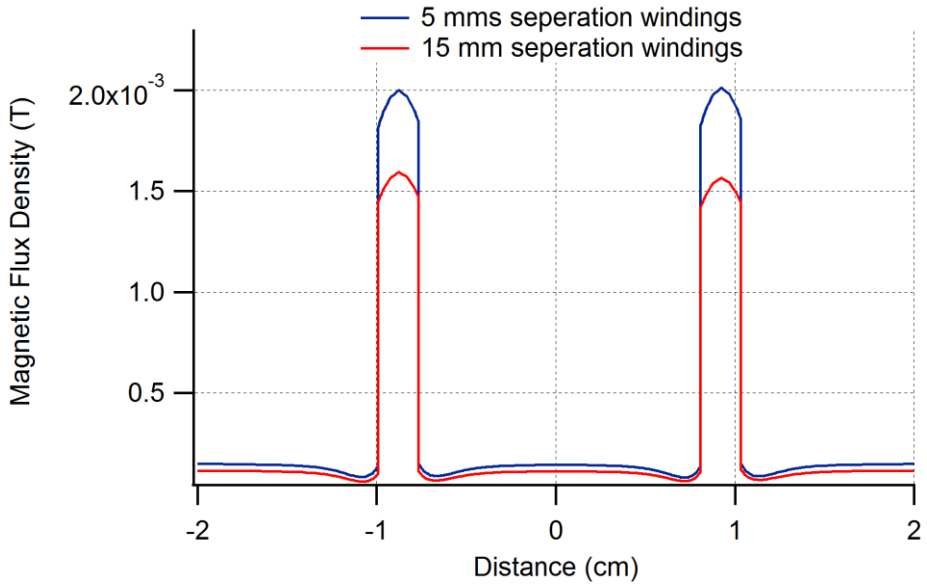

Figure 47: Waterfall plot of the magnetic flux density within the ferrite rods and the air space around them from the 5 mm and 15 mm separation primary windings.

The numerical values of the C_{ser} and C_{par} are 700 pF and 0.2 nF. The Multisim software is used to simulate the Class-E power amplifier with applying DC voltage (V_{CC}) of 40 V. Fig. 48 shows the output voltage, the switch voltage (V_{DS}) and output current (I_P) waveforms of the calculated capacitors (C_{par} & C_{ser}). The calculated value of the C_{par} (0.2 nF) is large, so the C_{par} could not be charged fast enough to achieve resonance in the coil voltage and current, as shown in Fig. 48. The researchers used different approaches to tune the C_{par} of the Class-E power amplifier. Jourand *et al.* used a contraction factor (CF) to calculate the tuned C_{par} as C_{par}/CF. They chose CF as 40, so the tuned C_{par} is 522 pF [118]. The output voltage and the switch voltage of using 522 pF have distortions, as shown in Fig. 48 (a). Then, they considered the parasitic capacitance (C_{parmos}) effect of the MOSFET (IRF840). Hence, they calculated the tuned C_{par} as (C_{par}/CF) is in parallel with C_{parmos} [118], so the tuned C_{par} is 210 pF while the output voltage and the switch voltage of using the tuned C_{par} (210 pF) have distortion also, as shown in Fig. 48 (a). We used a typical tuning approach that is developed by Sokal. The C_{par} is adjusted to achieve the nominal V_{DS} waveform, where increasing the C_{par} moves the trough of the waveform upwards and to the right and vice versa [116]. Fig. 48 shows the simulation result of the Class-E amplifier using the suitable tuned C_{par} (600 pF), where the highest output voltage and current obtained are about 2.5 kV and 8.8 A (peak-to-peak) respectively, with applying 40 DCV from the DC supply (V_{CC}).

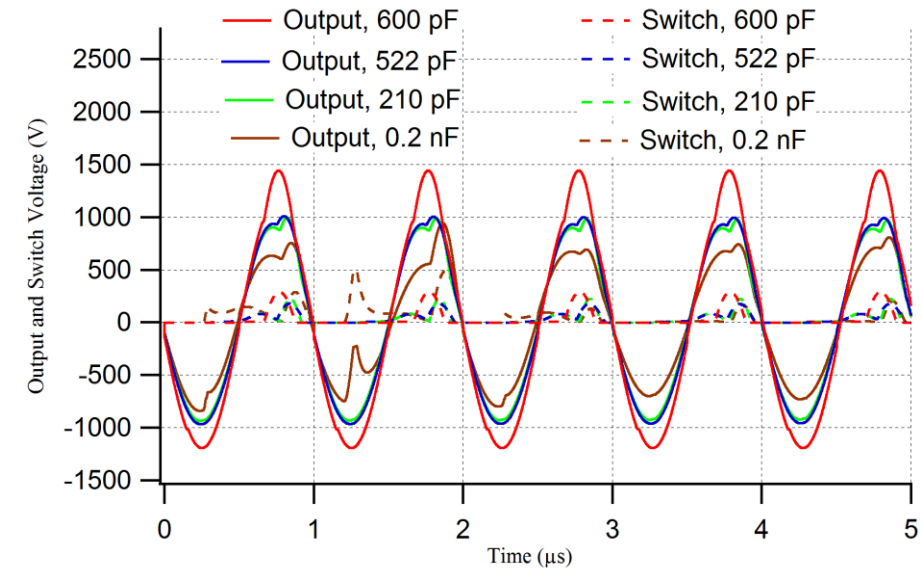

(a)

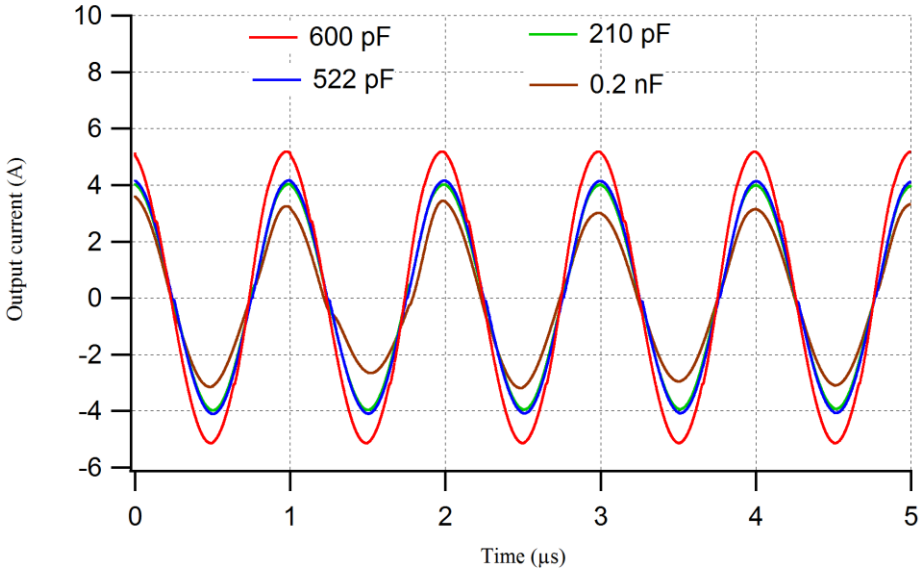

(b)

Figure 48: Simulation results of Class-E power amplifier (series resonance); (a) output and switch voltages, (b) output current (I_P).

The Altium CAD software is used to design a PCB for the Class-E power amplifier. The traces of PCB were built to handle ~8 A and ~2.5 kV (RMS values). Equation (62) shows the calculated width trace (w_t) of the PCB:

$$w_t = \frac{\left(\frac{I}{0.048\Delta T^{0.44}}\right)^{-0.725}}{t_{pcb}} \tag{62}$$

where, I is the maximum current in RMS value (8 A), ΔT is temperature difference, and t_{pcb} is the thickness of the PCB that is related to the amount of the copper covering the PCB.

6.4 Improved LCWPT Experimental Setup

The tissue absorption loss increases with frequency, while a lower operating frequency yields better power transfer efficiency [49]. A higher operating frequency reduces the physical size of electronic components; however, the power efficiency would decrease due to the increase in switching losses [50]. In order to avoid the tissue and switch losses problems, the operating resonant frequency of the redesigned LCWPT system is chosen as 1 MHz.

The *air core* and 4MFA configurations of the secondary coil employ 48/15 AWG/strands Litz wire. The same number of turns per layer in the 4MFA configuration is used, which is 7 turns/layer, however, we changed the number of the layers to three to improve the Q_S, as explained in Section 6.2.2. Fig. 49 shows the schematic diagram of the SIP (series and parallel resonance) for the *air core* and the 4MFA configurations.

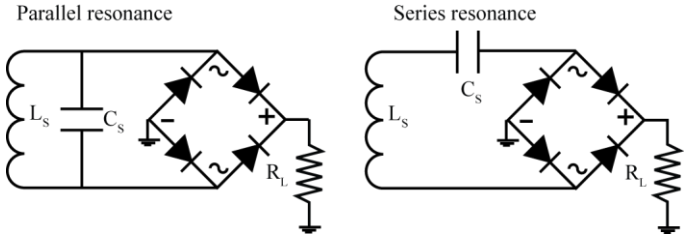

Figure 49: SIP configuration (series and parallel resonances).

The coil parameters (Q and L) of the primary coil, the *air core* and the 4MFA configurations are listed in Table 16, as measured using the HP 4285A LCR meter at 1 MHz. Ceramic capacitors (C_S) with a high quality factor and a low ESR were used to achieve high quality factor resonance of the secondary circuit. A secondary capacitor (C_S) of 1.180 nF is used to resonate the SIP at 1 MHz sharply. The quality factor (Q_S) of the secondary resonant circuit is given as [62]:

$$Q_S = \frac{R_{AC}}{w_o L_S} = w_o C_S R_{AC} \tag{63}$$

The resulting resonant frequency (1 MHz) and the L_SC_S-tank impedance (R_{LC}) for each configuration are measured using the HP 4193A Vector Impedance Meter for series and parallel resonance, as listed in Table 16.

TABLE 16: PARAMETERS OF REDESIGNED THE SECONDARY COIL AND THE LC-TANK IMPEDANCE OF SIP CONFIGURATIONS

Configuration	L (μH)	Q	R_{LC} (kΩ), parallel	R_{LC} (Ω), series
Primary coil	38.5	165	-	-
Air core	22.4	36	4.3	12
4MFA	21.4	45.5	4.7	15

A prototype of the redesigned LCWPT system for freely moving rodents was rebuilt, as shown in Fig. 50. The primary coil was wound around a rodent cage, as shown in Fig. 40 The output current of the Class-E (primary current (I_P)) is measured by a current probe (Agilent N2893A), as shown in Fig. 50. The output voltage and switch voltage (V_{DS}) of the Class-E power amplifier are measured by high voltage probes, as shown in Fig. 51.

6.5 Improved LCWPT Experimental Results

Experiments with the *air core* and the 4MFA prototype SIP configurations were conducted to measure the received power transfer at the center and the edge of the cage. The WMS measured the DC induced voltage across the load (R_L) and transmitted the data wirelessly to the base station, as shown in Fig. 25. Equation (30) calculated the received power that depends on the applying current (I_P) and the SIP orientation, as shown in Figs 52-53.

In order to investigate the performance of the SIP of using series or parallel resonance, as explained in Section 6.2, the induced current (I_{ind}) of the secondary circuit is calculated, which is given as [122]:

$$I_{ind} = \frac{jwM_{SP}I_P}{Z_2} \tag{64}$$

where, Z_2 is the impedance of the secondary circuit.

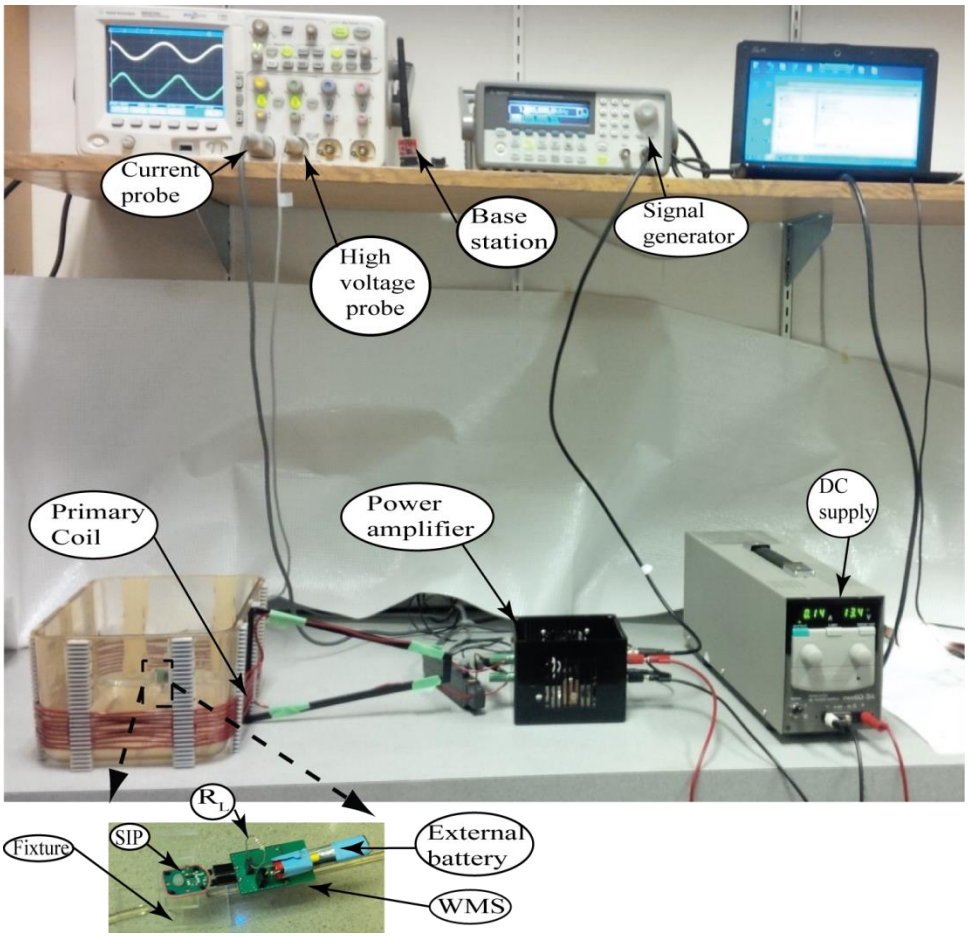

Figure 50: Experimental setup of improved LCWPT system.

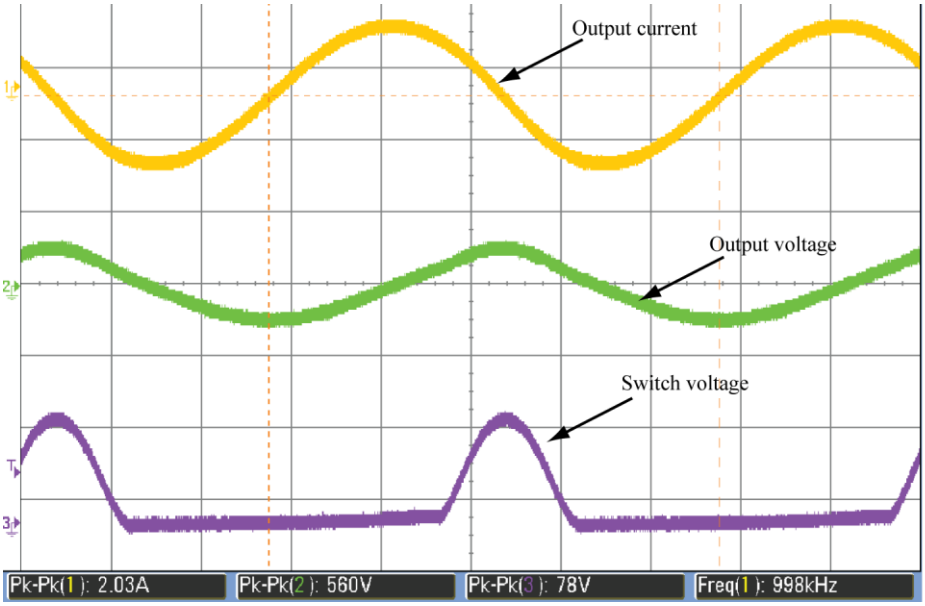

Figure 51: Outputs of Class-E power amplifier (series resonance).

Under resonant conditions the capacitor and the inductor cancel each other and Z_2 equals R_{LC}. The R_{LC} of the series resonance of the 4MFA is 15 Ω, however, the R_{LC} of the parallel resonance of the SIP is around 5 kΩ. Consequently, the high induced current (I_{ind}) of the series resonance is higher than the parallel resonance of the secondary circuit. However, we found that the rectified voltage (V_{rec}) of the series resonance of the secondary circuit (SIP) is low, in the mV range. Hence, the received power of the series resonance of the SIP is in µW range that is much lower than the parallel resonance of the SIP. Therefore, our experiments proceeded using the SP topology of the LCWPT.

6.5.1 Redesigned Air Core Configuration

Fig. 52 shows the received power to the *air core* configuration when it is placed at the center and the edge of the primary cage. The *air core* uses a R_L value of 5 kΩ to achieve impedance matching within the SIP itself. The maximum power received occurs at 0° orientation with an applied primary coil current (I_p) of 2.5 A. The maximum power transferred is 94.3 mW when the *air core* at the 0° orientation and at the edge of the primary cage, as shown in Fig. 52 (b).

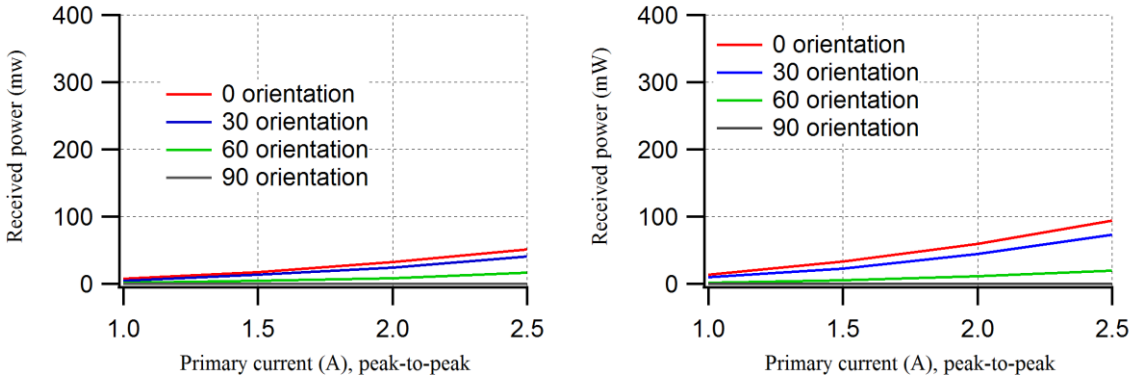

Figure 52: Power received in the *air core* configuration of the redesigned LCWPT at; (a) the middle of the cage, (b) the edge of the cage.

6.5.2 Redesigned 4MFA Configuration

Fig. 53 shows the power transferred to the 4MFA configuration at the center and the edge of the primary cage. The 4MFA configuration uses a R_L value of 5 kΩ to achieve impedance matching within the SIP. The maximum power received is 395 mW, which occurs at the 0° orientation and at the edge of the primary cage, as shown in Fig. 53 (b).

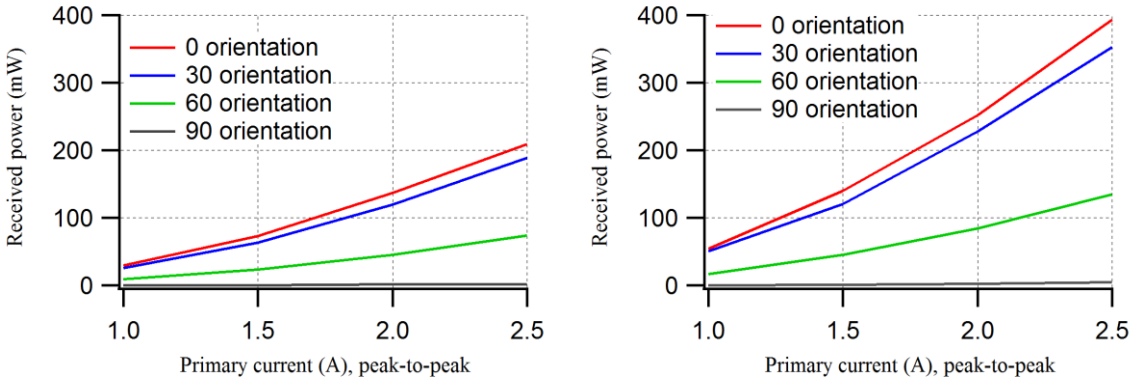

Figure 53: Power received in the 4MFA configuration of the redesigned LCWPT at; (a) the middle of the cage, (b) the edge of the cage.

6.6 Discussion

The results of the *air core* and the 4MFA configurations are as expected. As the applied primary current increases the V_{rec} increases, leading to higher power transfer. As long as the orientation of the SIP increases beyond 0°, coupling is reduced, leading to lower V_{rec}, which becomes very small when $\theta \approx 90°$.

In series compensation of the secondary circuit (SIP), the L_SC_S-tank acts as a short circuit. The induced voltage (V_{ind}) is independent of the load and equals to the secondary open circuit voltage [103]. We found the induced current (I_{ind}) of the 4MFA configuration with the matched impedance (15 Ω) was 30 mA, but the induced voltage was 468 mV when the applying current (I_P) was 2 A (peak-to-peak). In parallel compensation of the secondary circuit (SIP), the induced current (I_{ind}) is independent of the load [103]. The induced current of the 4MFA configuration with the matched impedance (5 kΩ) was 4 mA, and the induced voltage was 17 V when the applying current (I_P) was 2 A. Therefore, the SS topology is not suitable for LCWPT systems; it is applicable for a large-scale application like vehicles to provide a high charging current.

The electromagnetic field generated by the primary coil covers the whole cage area, but the magnetic field at the center is weaker than at the edge. Therefore, the power transferred to the SIP is higher at the edge of the cage than at the center of the cage, as shown in Figs 52-53. The complete LCWPT system is characterized in terms of end-to-end efficiency ($\eta_{DC\text{-}Load}$), as given in equation (34). Table 17 summarizes the efficiency of the *air core* and the 4MFA configurations at the center and the edge of the primary cage. Fig. 54 shows the total efficiency ($\eta_{DC\text{-}Load}$) of our LCWPT system using the 4MFA configuration versus the operational frequency

(from the signal generator), with applying current (I_P) of 2 A. The maximum efficiency is achieved at the edge of the cage when the magnetic resonant coupling is achieved at the resonant frequency (1 MHz), which is 14%. The efficiency drops gradually when the operation frequency deviates (increases/decreases) from the tuned point that represents the resonant frequency of the LCWPT. This is due to the fact that the required VA rating of the power supply increases dramatically when the operational frequency moves away from the tuned frequency [103]. The experimental results confirmed that the efficiency of WPT systems depends on the coupling coefficient, the quality factors of the coils, the distance and the orientation between the coils.

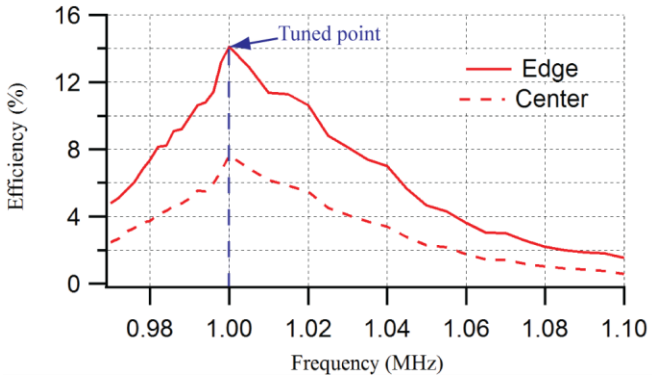

Figure 54: Total efficiency of the redesigned LCWPT versus the applied frequency.

TABLE 17: TOTAL EFFICIENCY ($\eta_{DC\text{-}LOAD}$) OF THE IMPROVED LCWPT

Configuration	1.0 A		1.5 A		2.0 A		2.5 A	
	Cen.	Edge	Cen.	Edge	Cen.	Edge	Cen.	Edge
Air core, 0˚	1.3	2.3	1.8	3.5	2.5	4.7	2.0	3.6
Air core, 30˚	0.8	1.7	1.4	2.7	1.9	3.5	1.6	2.8
Air core, 60˚	0.3	0.3	0.4	0.7	0.7	1	0.6	0.8
Air core, 90˚	0	0	0	0	0	0	0	0
4MFA, 0˚	4.8	8.9	6.6	12.7	7.6	14.1	7.5	14.1
4MFA, 30˚	4.2	8.2	5.7	10.9	6.7	12.7	6.8	12.7
4MFA, 60˚	1.4	2.7	2.1	4.1	2.5	4.7	2.6	4.8
4MFA, 90˚	0.01	0.04	0.03	0.1	0.07	0.13	0.07	0.16

Our redesigned LCWPT system draws 180 mA and 12 V from the DC power supply to provide the primary current (I_P) 2.5 A (peak-to-peak). The DC VA ratings of using this design LCWPT system are lower than the previous system of Chapter 4 (P_{in} is lower). The received power (P_o) increased using this design of the LCWPT system. Therefore, the total efficiency ($\eta_{DC\text{-}Load}$) of this design LCWPT system is higher than the previous LCWPT system (Chapter 4). We can operate our LCWPT with applying a current up to 2 A (peak-to-peak) only that draws 140 mA and 9 V from the DC supply. The redesigned LCWPT system can provide the needed power for the telemetry device (EEG/stimulator) with applying a primary current of 2 A. This design LCWPT system can be powered by a portable (external) battery.

Chapter 7: Controlling WPT by Tuning and Detuning Secondary Resonance

7.1 Introduction

One of our objectives of this thesis is powering multiple telemetric devices continuously that are implanted subcutaneously in rats or mounted on mice head. Fig. 55 shows freely moving multiple mice in one cage (primary coil), the telemetric device is placed on the head of a mouse. During building our WPT system for rodents, we observed some problems that cause a resonant frequency mismatch in WPT systems. Researchers reported these problems: (1) The loading effect, where McCormick *et al*. reported the loading effect causes mismatch of the resonant frequency of the WPT systems [70]; (2) The temperature effect, where Wang *et al*. found that the high induced voltage generates the higher temperatures in the implant that affects the secondary capacitor (C_s) and creates the resonant frequency mismatch of the L_SC_S-tank circuit [103]. Also, this increasing heat in the implant may cause a detrimental effect on the tissue in the long term, and may damage the electronic components of the telemetric devices (electronic heating problem) [62, 123]; (3) In the case of multiple secondary circuits within the same primary coil, mutual coupling may develop between the secondary coils. This mutual coupling will cause mismatch of the resonant frequency of each secondary circuit (telemetric device) [124].

A description of a literature review that illustrates how the resonant frequency mismatch is solved is referred to in Section 7.2. In this Chapter, we designed a novel scheme to remedy the electronic heating problems, and the resonant frequency mismatch between the primary coil and the RIDs. Furthermore, this novel scheme allows for the use of multiple secondary circuits (telemetric devices) to operate within a single primary coil, since each secondary circuit can tune/detune its resonant frequency independently of the others.

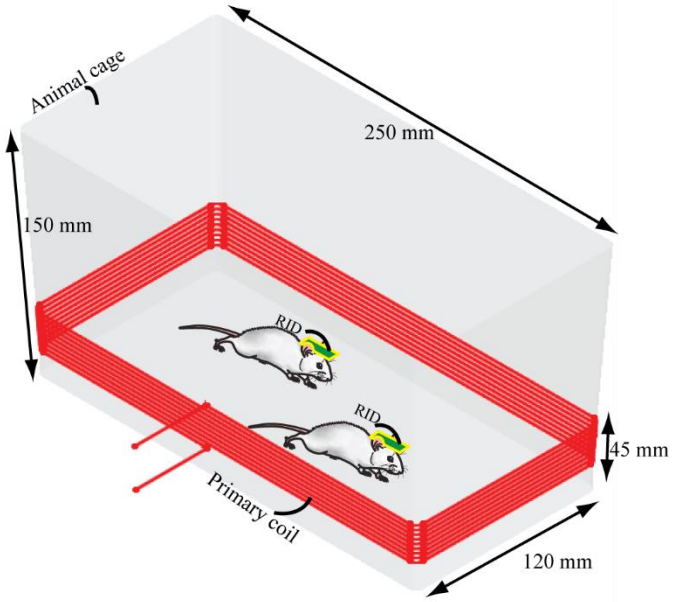

Figure 55: WPT concept for multiple rodents, with a primary coil wrapped around a mouse housing cage.

7.2 Literature Survey

A number of researchers investigated the WPT systems to eliminate the resonant frequency mismatch between the primary circuit and secondary circuit. The researchers used WPT systems for either large applications (received power higher than 10 W) or small applications (power transferred lower than 10 W). There are two main approaches used to control the WPT system. The first main approach is to control the primary circuit with respect to the secondary circuit. Dissanayake *et al.* designed a WPT system based on magnetic resonance for implantable medical devices in a sheep. Their WPT system was controlled using a variable capacitance in the primary tank circuit, which is used to adjust the resonant frequency. Their variable capacitance is achieved using switched capacitor control; however, the frequency of the secondary resonant tank is fixed [125]. Ng *et al.* built an adaptive controller using back telemetry (load modulation technique) to tune the resonant frequency of the primary (transmitter) coil; however, the resonant frequency of secondary tank circuit (retinal prostheses) is fixed [126]. Brusamarello *et al.* used two microcontrollers (MCUs), where one works with the primary circuit and the other MCU is in the secondary circuit. The MCU of the primary circuit initializes a communication link with the MCU of the secondary circuit. Thus, the control system on the primary circuit starts a scan frequency synchronized with the measurements of received power over the load of the secondary circuit. At each frequency point, a measurement of power is performed on the secondary circuit.

This measurement is sent by a wireless link to the primary circuit, and the algorithm scans for the optimum operation point, and adopts it as the resonant frequency [127]. Si *et al.* developed a frequency control method that is used for regulating the operating frequency of the primary driver circuit (Class-E power amplifier), with respect to the measured feedback resonant frequency of the implantable devices (left ventricular assist devices (LVAD)) [128].

The second main approach is to control the resonant frequency of the secondary circuit of the WPT system. Boys *et al.* designed a short control scheme that is the most well-known control technique used in the IPT. The controlled secondary circuit of the short control consists of a L_SC_S-tank, a switch (S), a rectifier, a freewheeling diode (D), a DC inductor (L_{DC}), and a DC capacitor (C_{DC}), as shown in Fig. 56. The short control works like a buck converter that uses a switch to control the average load current through hysteresis or pulse width modulation (PWM) [122]. Hu *et al.* designed a phase-controlled variable inductor to tune/detune the secondary coil, based on a short control scheme, as shown in Fig. 57. They built the phase-controlled inductor (L) based on two semiconductor switches (S_1 and S_2) to improve the power efficiency of their IPT system. The inductor (L) was controlled by the two series switches (S_1 and S_2), so the equivalent inductance would become variable. The AC inductor current (I_L) followed in both directions, as a result of the switches (S_1 and S_2) and their anti-parallel diodes. The I_L increased gradually in one direction when both switches (S_1 and S_2) were turned on, and zero current switching (ZCS) turn-on operation occurred. The ZCS turn-off operation was achieved when the inductor current was detected and the switch was only turned off when its anti-parallel diode is on [113]. This causes power losses to the IPT systems and decreases the overall efficiency of the system. The IPT system suffers severely from this inefficient operation particularly under no/light load conditions [129]. The short current occurs when the switch is on, which produces dangerous high current that causes the switching devices to fail [130].

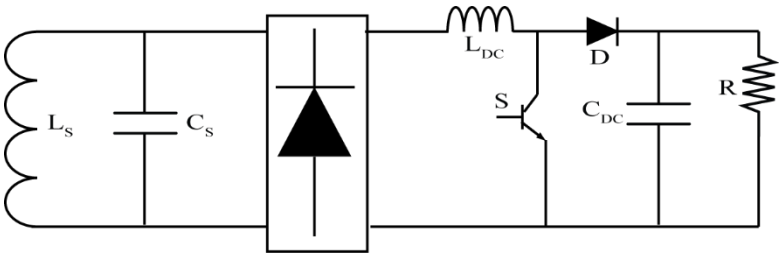

Figure 56: Short control scheme used in the secondary circuit [122].

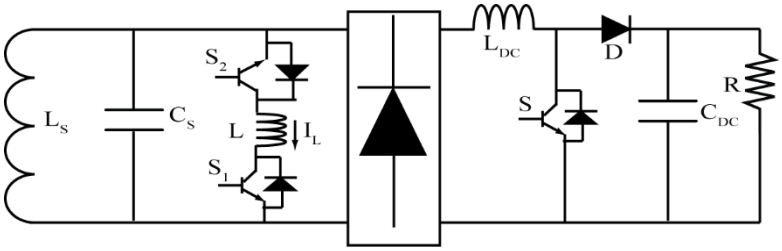

Figure 57: Secondary circuit with a phase controlled inductor [113].

James *et al.* used a variable inductor circuit within the L_SC_S-tank, which consists of a tuning inductor (L_2), two switches, two diodes, and a compensating capacitor (C_2). The two switches were controlled by a PLL scheme. The variable inductor circuit was connected in parallel with the LC-tank, where the current through L_2 was balanced by the current through C_2 in the normal operation. The PLL controlled the resonance of the secondary circuit when the current through L_2 changed (increased/decreased). Their variable inductor circuit kept the resonance of the secondary circuit by varying the current in the tuning inductor (L_2) and the compensating capacitor (C_2) [131]. Si *et al.* designed a dynamic tuning/detuning (DTD) control technique that dynamically changed the tuning/detuning condition of the secondary circuit with respect to the required voltage to power the load (application device). It is achieved by deliberately putting a soft switched capacitor (C) parallel to the secondary capacitor (C_s), as show in Fig. 58. The output voltage is used as a feedback signal to determine the turn on/off time of the soft switch and thereby achieves the required equivalent capacitance. The DTD process is divided into four segments: initial, discharging, charging, and final segment. Based on analytical analysis of each segment, an iterative method is used to obtain a numerical solution for the detuning operating frequency [132]. There are some challenges with the DTD method as follows: The relationship between the tuning capacitance and the output voltage is bell shaped; therefore, it can result in two possible operating points with one being in the over tuning region and the other in under tuning region [133]. It is insufficient to use the DTD method to achieve maximum power transfer when the operating frequency shifts to the other region due to circuit parameter variations. It may track in the wrong direction and fail to control the output voltage [134]. Covic *et al.* built a self-tuning WPT system. They used a binary series of capacitors (C, $2C$, $4C$, $8C$) that were switched via relays wired across the secondary LC-tank (L_SC_S), as shown in Fig. 59. Their binary series capacitors were added to tune the secondary LC-tank. The equivalent capacitance value from adding the tuning capacitors is big, in the range of μF that is suitable for high power applications.

Their WPT system was used in materials handling applications that require 500 W [135]. Hsu *et al.* designed a system using an inductor-capacitor-inductor (LCL) that is based on a transformer in the secondary circuit, as shown in Fig. 60 [133]. Hsu *et al.* discovered that their control approach (LCL) is restrained by the tuning step. A larger step change in the inductance often causes chattering of the output voltage. Although the chattering effect can be reduced by using a smaller step change in the inductance, it causes the overall response to be sluggish. They remedied this problem by designing a fuzzy logic controller to make the overall response fast [134].

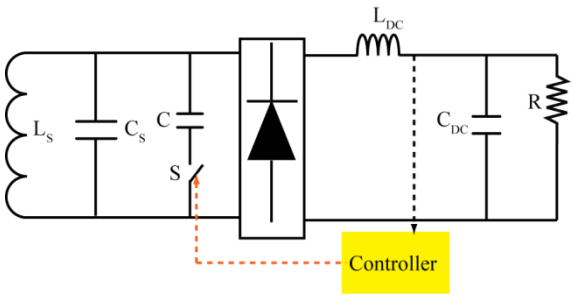

Figure 58: Schematic of DTD technique [132].

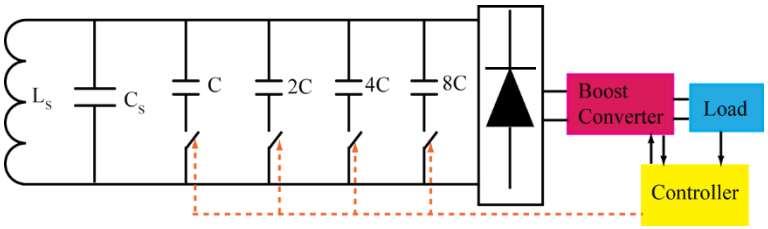

Figure 59: Schematic using relay to tune the secondary circuit [135].

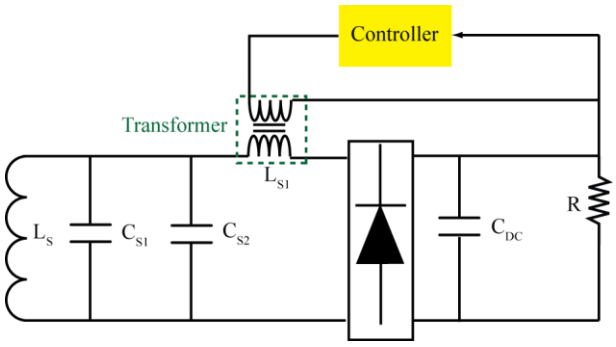

Figure 60: Using a transformer in the secondary circuit [133].

Huang *et al.* designed a fast switching control topology to regulate the power flow by adjusting the equivalent ac output voltage of the LCL network using two diodes and two switches (S_1 and S_2) in the secondary circuit. Their IPT system was used for vehicle applications, where their

received power of the secondary circuit was 2.5 kW. The idea of their topology is similar to the traditional controlled rectifier to regulate the average output current through the rectifier, while allowing variance in mutual coupling. Fig. 61 shows their designed secondary circuit, the series tuning capacitor (C_{series}) and C_S are used to achieve the resonance of the secondary circuit, the values of L_2 and C_2 are designed to accommodate the extra inductance introduced by the nonlinear effect of the rectifier to minimize the current in the secondary coil (L_S) [136]. Pantic *et al.* built a tri-state boost converter in their secondary circuit, as shown in Fig. 62. Their WPT system was used for vehicle applications, where the received power was 10 kW. They used a freewheeling period to control the reactive power reflected into the secondary resonant tank circuit (including rectifier circuit) by appropriately partitioning the freewheeling period [137]. Hsu *et al.* used the DTD control technique that was designed by Si *et al.* in [132], where the switch is connected in series with a tuning/detuning capacitor, which are connected in parallel with the secondary L_SC_S-tank circuit, as shown in Fig. 58. The objective of their approach is to control the power flow of the L_SC_S-tank circuit by either increasing or decreasing the tuning/detuning capacitance. The value of the tuning/detuning capacitor is big, in the µF range. The generated signal from the controller is denoted as a switching signal that controlled the effective tuning/detuning capacitance using different values of the duty cycle. The switch signal controlled the charging and discharging of the capacitor (can either be a unidirectional or bidirectional switch). They used a PI controller [138]; however, the PI controller was incapable of performing control over a bell-shape relationship between the tuning/detuning capacitance and the induce voltage, and the chattering effect, as explained in [139]. The performance of the controller is dependent on two major factors: the tuning/detuning step-size and the sampling frequency. Therefore, they used the fuzzy logic controller to overcome the limitations of the PI controller and make the system response fast [135]. The designed WPT systems by Hsu *et al.* [133-134, 138-139] are used for vehicle applications.

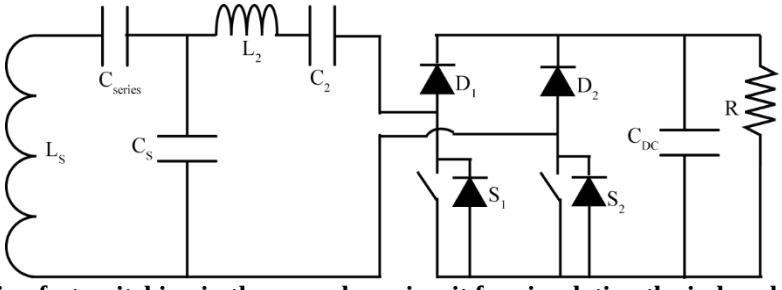

Figure 61: Using fast switching in the secondary circuit for circulating the induced current [136].

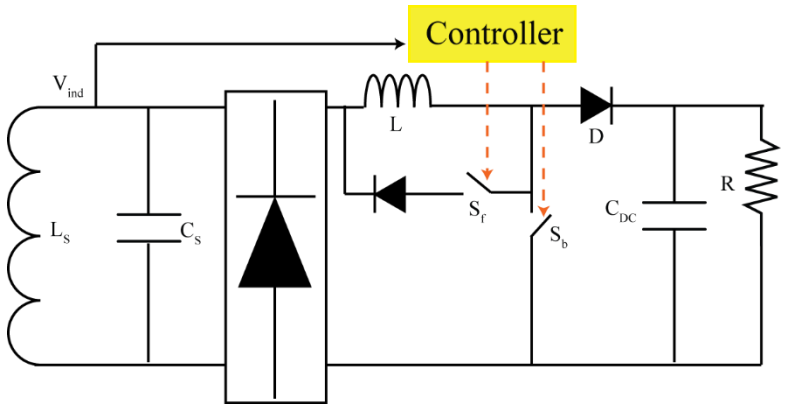

Figure 62: Tri-state boost in the secondary circuit [137].

Although the presented research of Hsu *et al.* is able to overcome all of the drawbacks of the previous solutions, some issues still remain. Namely, the nonlinearity, the slow dynamic, and the bulkiness of the transformer as the variable inductor are significant limitations of the proposed approach. Also, their design depends on complicated control algorithm using the fuzzy logic, for selection of a sampling frequency and step size [140].

Petersen designed a tuning WPT for biomedical applications, with efficiency of 0.7%. He used a switching capacitor circuit that was switched by MOSFETs to change the capacitance of the secondary circuit, as shown in Fig. 63. The switched capacitors C_{a1}/C_{a2} are small with respect to un-switched capacitors C_{b1}/C_{b2}, the effective range of the variability is small, and vice versa. The controller was used to switch the MOSFETs and control the timing of the MOSFET switching using different values of duty cycles. The control of the timing on the MOSFET switching allowed a continuously variable capacitance, where the minimum capacitance occurs with 50% duty cycle, and maximum capacitance happens with 100% duty cycle [141]. Riehl *et al.* designed a resonant WPT that uses parallel series resonant secondary capacitors (C_a and C_b) with an open-circuit impedance (Z_{oc}) adjustment by a switching capacitor (C_D), as shown in Fig. 64. The capacitor (C_D) was switched to adjust Z_{oc} to reduce the induced voltage. The switching capacitor changed Z_{oc} that also changed the reflected impedance seen by the primary coil, so the switching capacitor (C_D) regulated the induced voltage [142]. Yung-Chih *et al.* designed multiple wireless power receivers using a programmable power path. Their system depends on a linear low dropout regulator (LDO), where the LDO input voltage (rectified voltage) was controlled very close to the LDO output voltage. The rectifier voltage (V_{rec}) can be higher than the regulator output that made the power transfer very inefficient through the LDO. Therefore, a switching

mode regulator (SMPS) was applied for better efficiency when the voltage step down ratio is large [143].

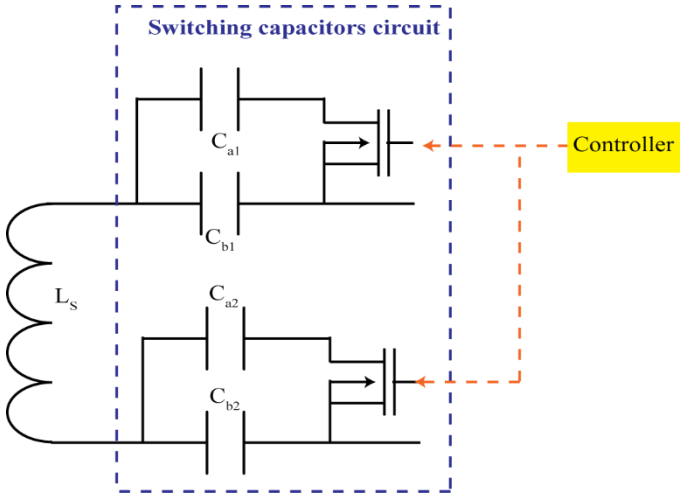

Figure 63: Designed tuning secondary circuit using switched capacitors of [141].

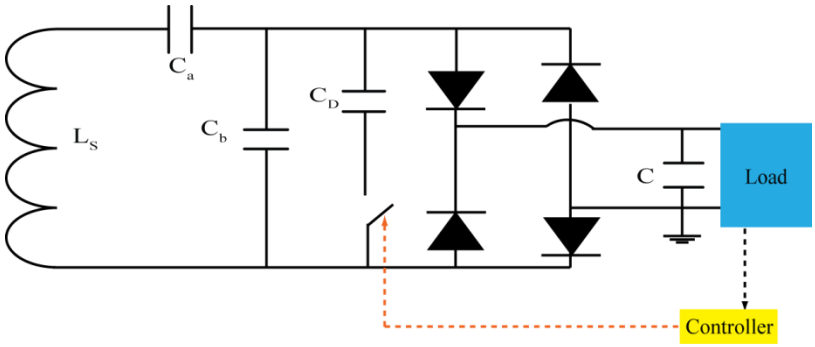

Figure 64: Controlling open circuit impedance of the secondary circuit of [142].

7.3 Limitation of Other Approaches of the Literature

In the various other schemes described in the literature, there are limitations of their approach, and they differ from our proposal. For the control schemes that control the primary circuit resonant frequency [125-128], these are not suitable for maintaining the resonance with multiple secondary coils within one primary coil. If there are multiple secondary coils in a single primary coil, each secondary circuit may have a slightly different resonant frequency that varies in time, for various reasons. The resonant frequency of each secondary circuit (RID) shifts as a result of the mutual inductance effect between the implants, and possible heating effects that change capacitance or inductance properties. Hence, by controlling the resonance of the primary circuit (power amplifier), it cannot keep the resonance of all the secondary circuits. In such a scenario, it is preferable to control the resonant frequency of each freely moving RID and fix the resonant

frequency of the primary circuit. Another limitation of tuning/detuning the primary circuit is the use of continuous switching, which can cause a large power loss due to switching, and the resultant surge currents that can damage the switching devices [133, 144].

The control schemes described for tuning/detuning the secondary circuit in [113, 122, 131, 133-139, 142-143], are more suitable for WPT systems for large scale applications like wireless charging of vehicles. This is because much higher power transfer levels are involved, the needed tuning/detuning inductor occupies a large volume, and the tuning/detuning capacitor value is large, in the range of μF. The control schemes of the secondary circuits in [133-134] are complicated, and have a slow dynamic response when tuning/detuning secondary circuits, which causes a sluggish response [140], and is not suitable for fast application devices (such as rodent movement). The limitation of using the DTD method [132] is that any change in the parameters of the secondary circuit affects the operation of the four segments and creates a resonant frequency mismatch. The WPT method using relays [135] is not suitable for biomedical (small size) applications since the relay occupies large volume. Also, the relay requires a high operating current to turn on, which represents a problem for low power applications (telemetry devices). Petersen claimed that his WPT system is used for biomedical applications [141]. However, the maximum received power of his secondary circuit (Fig. 63) was 15 W, which is considered high power for implant applications. Also, Petersen's WPT system is AC-AC, where the input to the primary circuit is AC power, and the output power of the secondary circuit is AC power. Since there is no rectification on the secondary circuit, DC power is not available which prevents the use of digital electronics needed for telemetry acquisition, signal processing, and digital communication. The WPT system of Riehl *et al*. (Fig. 64) [142] depends on controlling the reflected impedance of the secondary circuit seen by the primary circuit. Their WPT system is suitable for large WPT applications that have high coupling coefficient. But their WPT system is not suitable for the small WPT applications, such as LCWPT systems for biomedical devices. This is due to the reflected impedance of the secondary circuit is a function of the coupling coefficient, which can be neglected in LCWPT system, as described in Section 6.2.1. Also their designed secondary circuit might likely have a floating ground problem because of the connection of the switching capacitor (C_D) with the full bridge rectifier, as it is explained in detail in our design of the controllable LCWPT, in Section 7.5.1.

7.4 Methodology for Our Controllable LCWPT

There are two main approaches to control the LCWPT system to adjust the magnetic resonant coupling between the primary circuit and the secondary circuit(s). These two approaches are: (1) Controlling the resonance of the primary tank circuit with respect to the secondary circuit; (2) Controlling the resonance of the secondary tank circuits with respect to the primary circuit. The first approach is not applicable when using the multiple secondary circuits (RIDs) in a single primary coil, because of the potential resonant frequency differences and changes of the RIDs, as a result of mutual inductance effect between the implants, and possible electronic heating that change capacitance or inductance properties. Even if we control a telemetric device (secondary circuit) within a primary coil, the first approach is costly and complicated, where we need a feedback system to communicate from the secondary circuit to the base station, to control the resonance of the primary circuit. Our proposed technique is based on the second approach that tunes/detunes the resonant frequency of the secondary circuit(s), in order to match it with the steady resonant frequency of the primary circuit.

Our proposed controllable LCWPT system will meet two conditions: (i) Tuning the secondary circuits (RIDs) to achieve the magnetic resonant coupling with the primary circuit, in cases where resonant frequency mismatch occurs because of the mutual coupling effect from the multiple RIDs, from the heating effect on the L_SC_S-tank circuit, or from poor orientation between the secondary coil and primary coil; (ii) Detuning the secondary circuits (RIDs) to deviate the magnetic resonant coupling between the primary circuit and the RIDs when the secondary coil (L_S) induces high voltage that increases the temperature in the RID. This rising temperature creates electronic heating problems for the telemetric devices. Note that in our approach, we assume that nominal operation of the telemetric device occurs when the RID is oriented in a semi-favorable (limiting operation state) orientation between the secondary coil and primary coil.

We used the 4MFA configuration that acts as a L_SC_S-tank circuit in this Chapter. A number of experiments were done to validate our proposed tunable LCWPT system. One experimental setup was built to investigate the power transfer amounts at various orientations of the secondary coil with respect to the primary coil. Another experiment was done to characterize the power curve (received power versus frequency) of the secondary circuit, by adding and removing capacitors within the L_SC_S-tank circuit. This helped to establish the relationship between the capacitor values needed to tune or detune the secondary circuit operating (resonant) frequency by

specific amounts. Another experiment was done to determine the utility of using a MOSFET based switch within the L_SC_S-tank of the secondary circuit, while it operates within the primary electromagnetic field. Another experiment was done to investigate the mutual coupling effect between multiple secondary circuits within the same primary coil.

As we carried out this work, we designed a few different configurations to tune/detune the resonance of secondary circuits in a controllable manner. Most of these previous controllable secondary circuit configurations will work outside a primary electromagnetic field; however, they do not work within a primary electromagnetic field, as described in Section VI.A. We have included them here as a point of reference, to explain how we ultimately developed the working controllable LCWPT system proposed in this thesis.

7.5 Design of the Controllable Secondary Circuit

We designed our secondary (L_S) with a high quality factor (Q), shown by the sharp power curve (received power versus frequency) of Fig. 68 (a). The high Q coil gives a narrow frequency band which makes the secondary circuit sensitive to the operating frequency of the primary circuit, where the secondary resonant frequency is defined by its L_SC_S-tank circuit [141]. The secondary load is the collection of all application circuits (i.e. MCU, radio, etc.) on the secondary that consume power. Any extra (excess) power received by the secondary circuit increases the heat in the RID that causes electronic heating problems for the telemetric devices. Moreover, this increasing heat may affect the capacitance C_S of the L_SC_S-tank depending on the dielectric material of the capacitors [145-146], leading to resonant frequency shift.

The resonant frequency of our RID (secondary circuit) is a function of the L_SC_S-tank circuit. The proposed controller technique tunes/detunes the secondary resonance by adding/removing capacitor in parallel with the secondary capacitor (C_s), to change the overall capacitance value of L_SC_S-tank circuit. There are two different modes of operation achieved by adding/removing capacitor as follows: (1) Adding/removing (by electronic switching) small capacitors in range of 10-70 pF for fine tuning the resonant frequency of the secondary circuit. These small capacitor(s) tune the secondary circuit when the resonant frequency deviates due to the mutual coupling effect from the multiple secondary circuits, or due to the temperature effect; (2) Adding/removing (by electronic switching) large capacitors in the range of 100-800 pF to detune the RIDs (implants) when the temperature of the RID increases because of excessive received

power by the secondary coil due to favorable orientation between the primary and secondary coils. Experiments were done with different secondary circuit prototypes to determine the appropriate capacitor values corresponding to appropriate shifts in resonant frequency, as well as determining appropriate MOSFETs to be used as switches, as explained below. The main features of these capacitors are high *Q* and low ESR, where its dielectric material is independent of temperature and its voltage coefficient is constant over different applied voltages. We found that the NP0 dielectric material has these features in the ceramic capacitors [145].

7.5.1 Initial Designs

As explained in the methodology, we want to be able to add or remove capacitor within the L_SC_S-tank, upon command. Initially, we used MOSFETs to switch open/close capacitors (C_{D1}) that are in parallel to C_S, as shown in Fig. 65 (a, b and c). Our baseline design for the controllable secondary circuit (telemetric device) contains the L_SC_S-tank, the switching system (MOSFETS and capacitors), a rectifier bridge, the application secondary load, and a tuning/detuning controller that measures the rectified voltage (V_{rec}) and controls the switching system by a MCU. We used the Nordic MCU (nRF24LE1-F16Q24) that is used for the WMS, as described in Chapter 5.

As shown in Fig. 65 (a, b, and c), the MOSFET is connected in series with a tuning/detuning capacitor (C_{D1}), with both connected in parallel with the C_S capacitor. A DC control signal (high/low value of 3 V or 0 V, respectively) is supplied from the MCU to the MOSFET gate (G) via a wire. In Fig. 65 (a) the capacitor is connected to the drain (D) of the MOSFET, whereas in Fig. 65 (b) the capacitor is connected to the source (S) of the MOSFET. Both configurations of Fig. 65 (a and b) operate well outside an electromagnetic field, and the measured resonant frequency shift of the secondary circuit follows theoretical predictions. However, these configurations do not work properly when the secondary circuit is placed within the primary electromagnetic field. Upon further analysis, we found there a floating ground problem. As evident in the circuit diagram of Fig. 65, the L_SC_S-tank is AC (V_{ind} sinusoidal), while the MCU and application load are DC, where both halves of the circuit are separated by the full-wave bridge rectifier and buffer capacitor (C_{smooth}). The problem occurs because we are controlling the gate of the MOSFET with a DC control signal from the MCU, but the source and drain of the MOSFET are exposed to AC conditions. This creates a floating ground problem for the MOSFET operation, causing erratic operation. In order to overcome this problem, we decided to

use a half-wave bridge (voltage doubler) rectifier, which provides a common ground on the AC side (V_{ind} sinusoidal) and DC side of the secondary circuit, as shown in Fig. 65 (c). Using a half-wave bridge (voltage doubler) rectifier is very unusual for rectification of AC power, since it has a lower efficiency than full-wave bridge rectifiers (about 30% less efficient), and nearly all systems do not use it. However, it has the value of a common ground that we need here. Therefore we used a half-wave bridge (voltage doubler) rectifier that consists of two diodes, a coupling capacitor (C_C= 0.1µF), and a smoothing capacitor (C_{smooth}= 0.1µF), as shown in Fig. 65 (c). In our initial attempt, we connected the tuning/detuning capacitor (C_{D1}) to the source of the MOSFET, as shown in Fig. 65 (c); however, this setup does not work. This occurs since the capacitor effectively isolates the MOSFET from ground, and hence also creates the floating ground problem. This finally leads us to the correct design, as described in the next section below.

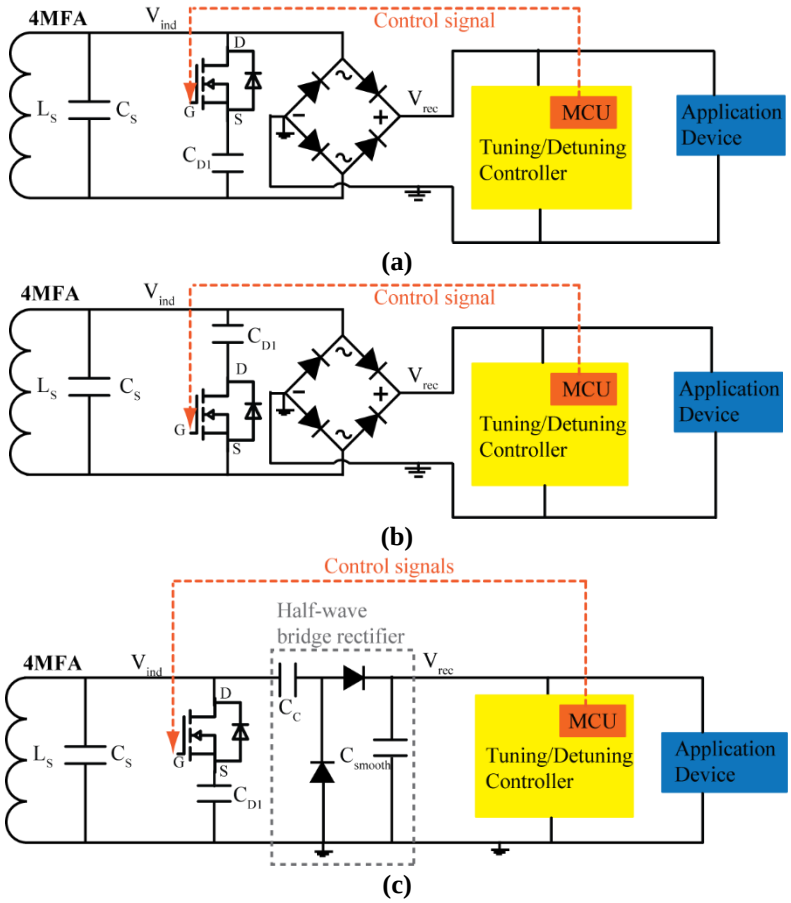

Figure 65: Switching capacitor techniques (not working); (a) using a full bridge rectifier, (b) using a full bridge rectifier with swapping the MOSFET and the C_D, (c) using a half-wave bridge rectifier.

7.5.2 Working Design

For our proposed working system, we connected the tuning/detuning capacitor (C_{D1}) to the drain of the MOSFET, while the source of the MOSFET is connected directly to the common ground, as shown in Fig. 66. This now provides the MOSFET with a common ground with respect to the MCU, allowing the control signal to effectively switch the MOSFET on/off. This is not intuitive, since it must use a half-wave bridge (voltage doubler) rectifier between the AC and DC side of the circuit, in order to operate the MOSFET via a DC control signal from a MCU.

The theory of operation of our proposed working system is now described: For achieving maximum power transfer, the resonant frequency of the secondary circuit (telemetric device) must equal the operating frequency of the primary circuit (1 MHz in our application). As previously explained, the resonant frequency of the secondary circuit may increase because of the heating effect [103, 146], which causes the secondary capacitor (C_S) value to drop. In addition, the resonant frequency of the secondary circuit may decrease when the secondary inductance (L_S) increases because of the mutual coupling of the multiple secondary circuits [103, 105] within the primary field. This increasing inductance is denoted as ΔL, the equivalent secondary inductance (L_{eq}) due to the multiple secondary coils, and is given as:

$$L_{eq} = \Delta L + L_S \tag{65}$$

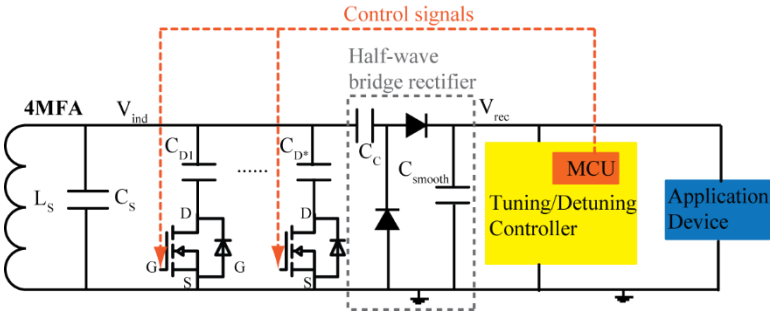

Figure 66: Switching capacitor technique using half-wave bridge rectifier with grounding the source of the MOSFET.

As a result of the multiple secondary circuits/RIDs, the total reflected impedance (Z_{rtot}) from the multiple RIDs is given as [105]:

$$Z_{rtot} = \sum_{i=1}^{n} Z_{ri} = n\frac{W^2 {M_{SP}}^{2^2}}{Z_s} \tag{66}$$

where, *n* is the number of the RIDs in the cage. The equivalent mutual inductance and coupling coefficient of the multiple RIDs are [105]:

$$M_{SPn} = \sqrt{n} M_{SP} \tag{67}$$

$$k_n = \sqrt{n} k \tag{68}$$

In order to compensate the ΔL, the secondary capacitance should be:

$$C_S = \frac{1}{{w_o}^2 (L_S + \Delta L)} \tag{69}$$

Our switching capacitor technique adds/removes capacitor (C_{D1}) to tune the RIDs to the resonant frequency. Also, we can add/remove additional capacitors (C_{D*}) to detune the RID from the resonant frequency to decrease the induced voltage (V_{ind}). In order to tune and detune the secondary circuits/RIDs and avoid bell-shape problem, we designed the $L_S C_S$-tank to resonate at over tuning region. While switching on and off between the capacitors (C_{D*}), we must keep the value of the R_{AC} almost same to achieve the matched impedance (R_L) and avoid the reflected impedance problem that may detune the resonance of the primary circuit, as report in [142]. The resistance, R_{AC}, should maintain its value during switching as [139, 147-149]:

$$R_{AC} \approx R_P \frac{\pi^2}{8} \tag{70}$$

where, R_P is the equivalent parallel resistance of the secondary coil, it is measured using a LCR meter [147-149].

The core of our telemetry device is based upon a system on chip (SOC) from Nordic Semiconductor (nRF24LE1). This SOC includes a 2.4GHz RF transceiver core, an 8-bit CPU, embedded Flash memory (16 kB), and a rich set of on-chip analog and digital peripherals which provides a flexible, single chip solution for our application [92]. Our analog signal of the rectified voltage (V_{rec}) and the application device (EEG/stimulator) are connected to the peripheral 12-bit ADC located on the SOC. The 2.4GHz radio provides a wireless link to the base station which passes the transmitted data to the laptop for view/saving the data.

The lack of memory precludes storage of parameters such as sample frequency, gain settings, and stimulation parameters. The sampling frequency of the controller should be selected based on the settling time (t_s). The settling time can be written as [145]:

$$t_s = R_{AC} C_{D*} \tag{71}$$

The sampling time of the proposed controller must be higher than t_s, otherwise the controller response will be sluggish with high values of the R_{AC} and C_{D*} [145]. We found that the power requirements increase linearly with the frequency of sampling of biological data. The time constant of our system is based on sampling rate/number of samples per packet. We set the sampling frequency of our telemetry device at 409Hz and 14 samples per packet, so the data (biology signals and V_{rec}) are transmitted at 29.2Hz or 34.2 milliseconds.

7.6 Experimental Setup of Controllable LCWPT

The SP topology is used to achieve the magnetic resonant coupling between the primary circuit and the secondary circuit, as illustrated in Section 6.6. Fig. 67 shows the schematic diagram of the controllable LCWPT system. The measured V_{rec} by the WMS is used as a feedback to control the MOSFETs. The telemetry device is composed of an application device (EEG/stimulator), a tuning/detuning controller, a MCU (nRF24LE1-F16Q48), and the WMS that uses the same MCU (nRF24LE1-F16Q48). A 2.4 GHz radio communication is built into the Nordic platform and uses a proprietary handshaking network protocol to transfer the measured data of the telemetry device to the base station.

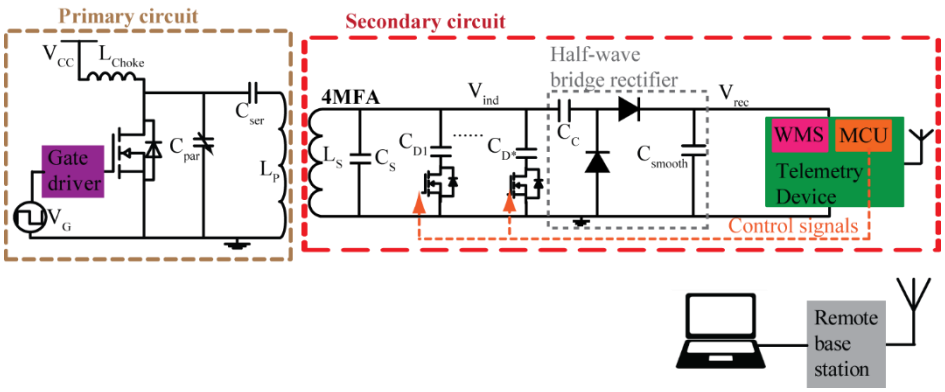

Figure 67: Block diagram of our controllable LCWPT system.

The controllable RID contains a $L_S C_S$-tank of the 4MFA configuration, the switch capacitors and a half-wave bridge rectifier, as shown in Fig. 67. The used MOSFET (switch) is a chip

(Si1026X) that has two N-channel MOSFETs. The properties of these MOSFETs are high power handling (V_{DS} up to 60 V), nanosecond switching (15 ns) capabilities and a low on-resistance (1.4 Ω) [150] that should not damp the coupling factor of the L_SC_S-tank. We used switching diodes (DA4J101K0R) for the half-wave bridge rectifier, which have a small reverse current (100 nA) and a short reverse recovery time (3 ns) [151].

In this Chapter, we wrapped the 4MFA secondary coil using the Litz wire 44/15 AWG/strands. The coil parameters (R_P, Q and L_s) of the primary coil and the secondary coil are listed in Table 18, as measured using the HP 4285A LCR meter. The L_SC_S-tank is created by using a 1313 pF capacitor (C_s) to resonate the RID at 1 MHz sharply. The HP 4193A vector impedance meter is used to measure the resonant frequency and impedance of the RID, where the measured impedance (R_{LC}) at the resonant frequency was 7.04 kΩ. Our experimental measurements make use of a conjugately matched load R_L to ensure the maximum power transfer for the overall system. The R_P of the secondary coil (L_S) is 8.2 kΩ, so the R_{AC} is recommended to be kept around 10.2 kΩ while switching capacitors (C_{D*}). The used match impedance (R_L) for the experiments is 10 kΩ.

For our controllable LCWPT experiments, we used the experimental setup of Fig. 50. We found that the resonant frequency of the primary circuit (Class-E amplifier) decreases by 10 kHz. This is a result of the total reflected impedance (Z_{rtot}) from the mutual inductance (M_{SPn}) of the multiple RIDs in the same primary coil. The C_{par} was needed to be decreased/increased by 3-8 pF when the multiple RIDs are in the same cage (primary coil). This small decrement/increment of the C_{par} was accomplished by a variable capacitor to achieve the magnetic resonant coupling between the primary circuit and the multiple RIDs (secondary circuits).

TABLE 18: PARAMETERS OF THE PRIMARY AND THE SECONDARY COILS OF THE CONTROLLABLE LCWPT SYSTEM

Configuration	AWG	R_P (kΩ)	Q	L (μH)
Primary coil (L_P)	22	49.5	165	38.5
Secondary coil (L_S)	44	8.2	55	19.3

7.7 Experimental Results of Controllable LCWPT

The physical RID (controllable secondary circuit) was constructed and a set of experiments were conducted to test its performance. The LCWPT experiment depends on the four parameters (I_P, R_L, the position and the orientation). We measured the received power by the RID at 0° orientation, the middle of the cage, with a matched impedance (R_L) 10 kΩ, and with applying a current (I_P) of 2 A only (peak-to-peak).

We investigated our controllable LCWPT performance using the WMS. Since the WMS must provide reliable measurements over time, its power must be supplied by a lithium-polymer battery to make its operation independent of the RID performance [1-2, 152], as shown in Fig. 50. We used the WMS to measure the rectified voltage (V_{rec}) of the secondary circuit, and then we calculated the received power at the various orientations [152]. The maximum power transferred (180 mW) occurs when the secondary coil is parallel to the primary electromagnetic field. However, the received power decreases as the orientation increases [2], where the received powers at 30°, 60°, and 90° are 127 mW, 38.2 mW, and 3.5 mW, respectively.

In order to determine the required switching capacitors to tune/detune the RID, the received power curve of our RID is needed to be obtained. We used different values of the secondary capacitors (C_S), to get the received power curve of the received power versus the frequency/C_S, as shown in Fig. 68 (a). The curve has a sharp peak, and the maximum received power is 180 mW at the resonant frequency of 1 MHz using the resonant secondary capacitor C_S of 1313 pF. We did the same measurements with using the switch MOSFET by adding a capacitor (C_{D1}) to find out the MOSFET effect. We noticed there is quite a difference between the received power by the RID with and without using the MOSFET, as shown in Fig. 68 (b). This difference is due to the stray capacitance of the MOSFET that changes in the electromagnetic field [150]. The stray capacitances of a MOSFET are given as:

$$C_{iss} = C_{GD} + C_{GS} \tag{72}$$

$$C_{oss} = C_{DS} + C_{GD} \tag{73}$$

$$C_{rss} = C_G \tag{74}$$

where, C_{iss} (input capacitance) is measured between the gate and the source, with the drain shorted to the source. C_{oss} (output capacitance) is measured between the drain and the source, with the gate shorted to the source. C_{rss} (reverse transfer capacitance) is measured between the

drain and the gate, with the source is connected to the ground. C_{GD}, C_{GS} and C_{DS} are the gate-drain capacitance, gate-source capacitance and drain-source capacitance, respectively.

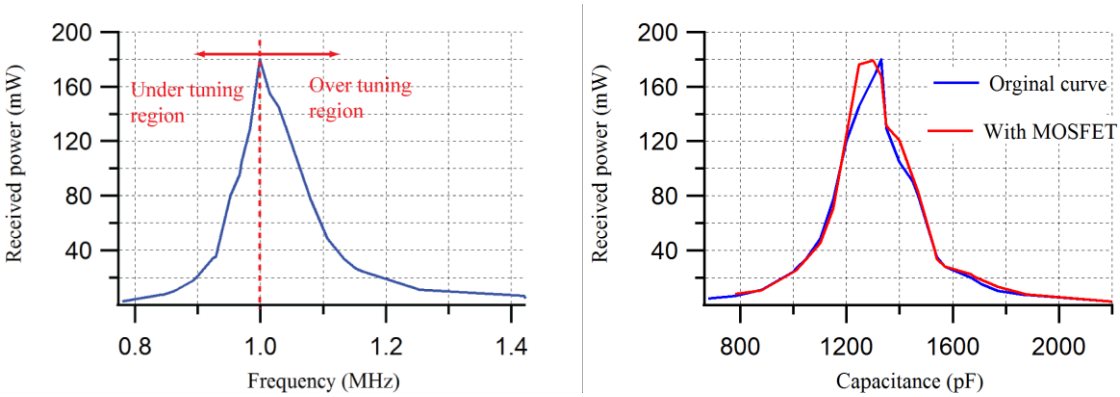

Figure 68: Received power versus frequency/capacitance; (a) received power versus frequency, (b) received power versus capacitance with and without using MOSFET.

We noticed that the impedance value (R_{LC}) of the RID changes when we switch with different values of the capacitors (C_{D*}). Therefore, we used a combination of switching capacitors (C_{D*}), which achieves a constant impedance value of the RID, while switching between these capacitors (C_{D*}). Moreover, the value of secondary capacitor (C_S) is chosen as lower than 1313 pF to resonate the implant in the over tuning region to avoid the bell curve problem. We used C_S= 680 pF, C_{D1}= 470 pF, C_{D2}= 100 pF, C_{D3}= 68 pF and C_{D4}= 47 pF, so we have 16 states of different received power values of our RID. The value of C_{D3} is used to tune the RID when two RIDs are at 0° orientation, in the same cage and separated by a distance of 0 cm (their edges touch each other), as explained in Section 7.8. The C_{D4} can be used to tune the secondary circuit when the secondary capacitance (C_S) decreases because of the heat effect. The two capacitors (C_{D1} and C_{D2}) are used to detune the RID when the heat increases due to high induced voltage (excessive received power). Table 18 shows the measured resonant frequency, impedance (R_{LC}), rectified voltage (V_{rec}) and received power of the different 16 states. The measured impedance (R_{LC}) is almost constant over switching between the four capacitors, as shown in Table 19. This avoids the reflected impedance problem. The maximum power (180 mW) is achieved at the resonant frequency of 1 MHz when the four capacitors are connected.

TABLE 19: MEASURED RESONANT FREQUENCY, IMPEDANCE, RECTIFIED VOLTAGE AND RECEIVED POWER OF SWITCHING CAPACITORS OF THE RID

C_{D1} 470 pF	C_{D2} 100 pF	C_{D3} 68 pF	C_{D4} 47 pF	F_{res} (MHz)	R_{LC} (kΩ)	V_{rec} (V)	P (mW)
1	1	1	1	1	6.26	42.4	179.6
1	1	1	0	1.024	6.3	37.6	141.2
1	1	0	1	1.028	6.33	37.5	140.3
1	1	0	0	1.037	6.33	32.4	104.6
1	0	1	1	1.053	6.31	29.1	84.7
1	0	1	0	1.056	6.37	28.9	83.8
1	0	0	1	1.066	6.31	25.9	67.1
1	0	0	0	1.076	6.36	22.8	52.2
0	1	1	1	1.236	6.85	11.5	13.2
0	1	1	0	1.243	6.88	10.2	10.4
0	1	0	1	1.257	6.9	9.8	9.6
0	1	0	0	1.279	6.94	9.3	8.8
0	0	1	1	1.283	7	9.1	8.2
0	0	1	0	1.29	6.92	8.9	7.9
0	0	0	1	1.333	7.04	7.6	5.8
0	0	0	0	1.338	7.05	7.2	5.1

7.8 Experimental Results of Multiple RIDs

In order to characterize the effect of mutual coupling as a result of using multiple RIDs (secondary circuit), an experimental setup of using multiple RID was conducted, as shown in Fig. 55. This helps to determine the required adding/removing capacitor (C_D) to compensate the ΔL due to the mutual coupling of the multiple RIDs. We used two RIDs in the primary coil, where the fixtures were used to mimic the orientations of the two RIDs. The received power by a RID is measured at 0° orientation and the center of the cage; we denoted this RID as a fixed RID. The other RID moves around the cage and rotates by 0°, 30°, 60°, and 90° with respect to the fixed RID. The received power is a function of the orientation and distance between two

RIDs. Table 20 lists the measured V_{rec} and the received power of the fixed RID. We found that the maximum dropped power is 6% when the moving RID is at the same orientation (0°) and 0 distance with the fixed RID (their edges touch each other), as shown in Table 20.

We measured the secondary inductance (L_{eqv}) using the HP 4285A LCR meter when the two secondary coils are at 0° orientation and their edges touch each other. We found the ΔL equals to 1.2 µH. In order to tune the RID due to the ΔL, equation (69) is used to determine the required capacitance (C_D) to be added/removed. This tuning capacitor equals 64 pF that is used to compensate the dropped power as a result of the mutual coupling between RIDs.

TABLE 20: MEASUREMENTS OF THE RECTIFIED VOLTAGE AND THE RECEIVED POWER OF THE FIXED RID

Distance (cm)	0°		30°		60°		90°	
	V_{rec} (V)	P (mW)	V_{rec} (V)	P (mW)	V_{rec} (V)	P (mW)	V_{rec} (V)	P (mW)
0	40.9	168	41.6	173	41.9	175.9	42.2	177.9
1	41.2	170	41.9	175.6	42.2	177.9	42.4	179.5
2	41.8	174	42.3	178.5	42.4	179.5	42.4	179.5
3	42.1	146.8	42.4	179.5	42.4	179.5	42.4	179.5
4	42.3	178.6	42.4	179.5	42.4	179.5	42.4	179.5
5	42.4	179.5	42.4	179.5	42.4	179.5	42.4	179.5
6	42.4	179.5	42.4	179.5	42.4	179.5	42.4	179.5

7.9 Discussion

We designed a controllable WPT system to tune and detune the resonance of the secondary circuit. For rodent applications, the code we wrote to control the MCU monitored the telemetry device every 400 milliseconds by checking the V_{rec} with respect to the power requirement of the application device (EEG/stimulator). The maximum settling time achieved is 20.4 ns using equation (71), as a result of adding capacitance (C_{D*}) of 2 nF, and R_{AC} is 10.2 kΩ.

We observed that the mutual coupling between the multiple secondary coils, and the thermal effect on the secondary capacitance (C_S), will detune the resonant frequency of the secondary circuits by 5-20 kHz. As a result of this resonant frequency mismatch, the received power by the RID drops slightly [103]. For example, the maximum reduction of the received power by the

RID is 6%. This happens when the edges of the two different RIDs touch each other at the same orientation, as shown in Table 20. Also, the resonance of the primary circuit detunes by 10 kHz when multiple (two) RIDs are used in the same primary coil.

In other cases, however, detuning the secondary circuits (RIDs) is needed when the RIDs induce too much voltage/current. This may present trouble by excessive heating of the electronic circuits in the telemetry device. The received power at 0° and 30° orientations is generally quite high, and will cause the described electronic heating problems for the telemetric devices for rodents. To remedy the electronic heating problem, we can detune the secondary circuit to decrease the high induced voltage. This can be done by adjusting the status of the switching capacitors (C_{D*}) that are listed in Table 19. For example, when the secondary circuit is oriented between 0° and 30° orientations, the programmed state "1001" corresponds to connection of capacitors C_{D1} (470 pF) and C_{D4} (47 pF) in parallel with the tank capacitor, thereby setting the resonant frequency (1.066 MHz), allowing for a received power of approximately 67 mW. If needed, the control system will change the programmed state to "0111", that corresponds to connection of capacitors C_{D2} (100 pF), C_{D3} (68 pF) and C_{D4} (47 pF), thereby changing the resonant frequency (1.236 MHz), and limiting the power transferred to 13.2 mW. This state "0111" can be used when the secondary circuit is oriented between 30° and 60° orientations. When using these states, the secondary circuit can guarantee our needed power to start up the telemetry device that is 51 mW for 100 – 300 milliseconds, and to run it indefinitely with a power of 12 mW after start-up. Our novel controllable scheme can be considered as a coarse tuning/detuning of the resonance of the secondary circuit, which has an advantage point of a low switching loss from the MOSFETs.

Chapter 8: Discussion

In this thesis, we show different ways to power telemetric devices for use as implants in biomedical applications. The focus has been on investigation of WPT systems, which have been found as the most suitable candidates to provide the needed power for our telemetric device application with rodents. The main characteristic of WPT systems for biomedical applications is that they are generally loosely coupled systems, which means low transferred power and efficiency. To increase the efficiency of the power transfer, we employed magnetic resonant coupling to match the frequency of the stationary primary coil (transmitter around the cage) to the resonant frequency of the freely moving secondary coil (receiver on the biosensor). Initially, we designed a piezoelectric-based device (EHAM) to generate electrical power by harvesting the kinetic energy available from the natural movement of mice. The maximum harvested power was 68 μW when the excitation frequency (mouse motion) corresponded to the resonant frequency of the energy harvester (11.7 Hz), as described in Chapter 2. Since mouse movements are spread across a range of low frequencies, and due to the size and mass restrictions of devices suited to mice and rats, this energy harvesting scheme (EHAM) was inherently unsuitable to power our telemetry devices.

Chapter 4 investigated a LCWPT system suitable for transmitting power to a telemetric device located on a freely moving rodent. Since the rodent orientation is variable, the coupling between the primary and secondary coils varies with the orientation between them. Methods to improve coupling at various orientations were investigated using ferrite rods placed within the secondary coil. FEA simulation was performed to find the magnetic flux density distribution around various secondary configurations to predict the best arrangements of ferrites within the secondary coil. Physical prototypes of four configurations (*air core*, WFR_4, 4MF and 4MFA) were constructed and experiments were conducted to determine the power transfer performance at the center of the cage. The 4MF configuration showed a clear improvement in power transfer compared to WFR_4, even though both configurations had similar coil properties and used the same volume of ferrite rods. By tilting the ferrite rods of the 4MF configuration to create the 4MFA configuration, it is shown that 4MFA increased power transfer in comparison to all other configurations and at all angular orientations. The 4MFA configuration was shown to provide up to 113 mW of power when oriented at 0° to the primary field, with a WPT efficiency of 1.5%. These maximum

received power and efficiency values were obtained when the applied current (I_P) was 2.5 A (peak-to-peak). Since the simulation results were non-resonant while the experimental results were resonant, only comparisons of normalized trends between the simulation and experiment were made. For any WPT system, some form of application circuit resides on a PCB to perform a function. In such a case, our design approach allowed for plenty of volume within the secondary coil winding for application circuits. The winding was wrapped around the perimeter of the PCB, with four ferrites placed in the corners inside the coil. This was in contrast to traditional approaches to tightly wrap the secondary coil around a solid ferrite. By using this approach, the minimal addition of ferrite rods at carefully placed locations provided significant improvements in power transfer at most orientations, while leaving plenty of volume for application circuits.

Chapter 5 described the design of a new testing device called WMS, for evaluating the LCWPT system properties. The WMS was designed and built to reduce measurement errors that are inherent to cable-based measurement due to field interference, noise, and voltage offset. The WMS measured sample analogue values (0 to 62.4 V) from the SIP/RID within the primary magnetic field and digitized them with 12-bit resolution. It then digitally transmitted these values via a wireless radio so that the performance of our LCWPT could be assessed during development. Furthermore, the WMS was made to minimize its own interference with the resonance of the LCWPT system by adhering to the design requirements summarized in Table 12 to achieve the specifications listed in Table 13. The WMS served as a useful and portable tool to evaluate the SIP/RID device without the problematic use of coaxial cables or current/voltage probes within the primary field. Physical prototypes of the WMS and SIP/RID configurations were constructed. Experimental tests showed that the WMS performed well by gathering data. It did not significantly affect the magnetic resonance of the LCWPT system and measured the received power with better performance than cable-based-measurement systems, as listed in Table 14.

Chapter 6 described work to redesign the LCWPT system to improve its total efficiency, by adjusting the power amplifier design, better coil design with higher quality factors, and changing the system (primary circuit and secondary circuit) topology. The previous LCWPT system of Chapter 4 has a low coupling coefficient, resulting in poor efficiency due to low quality factors

of the primary and the secondary coils, and also due to a long separation distance between the two coils (L_S and L_P). The efficiency of a WPT system using magnetic resonance is a function of the coupling coefficient and the quality factors of the primary and secondary coils. The coupling coefficient is limited by the separation distance between the coils, the primary coil to secondary coil diameter ratio, and the coil-to-coil angular misalignment. Different types of losses in the primary and secondary circuits were analyzed to maximize the total efficiency. The four topologies (SS, SP, PP and PS) for achieving the magnetic resonant coupling between the primary and the secondary circuit were investigated as a function of coupling coefficient and the variable load application to minimize the reflected impedance losses in the LCWPT systems. The redesigned LCWPT system was built with high quality factors of the primary and the secondary coils. Experimental results affirmed that the SP topology was suitable for LCWPT systems for biomedical applications. When the redesigned 4MFA configuration was used, the received power increased to 200 mW at the middle of the cage and at 0° orientation. The maximum total efficiency achieved at the center and the edge of the cage were 7.6% and 14.1%, respectively, as listed in Table 17. These values were obtained when the applied current (I_P) was 2 A (peak-to-peak), and the secondary coil was oriented to the primary electromagnetic field. The required VA ratings drawing from the DC power supply to provide 2 A (peak-to-peak) at the magnetic resonance were 9 V and 140 mA. Hence, an external and a portable DC power supply/battery can be used to power our redesigned LCWPT system.

Chapter 7 explored a new area to actively control the resonant frequency of the secondary circuit, using on-board closed-loop control. This allows us to control the resonant frequency match between the primary circuit and the secondary circuits in the WPT systems. This has two important applications: First, it allows us to control the temperature of the secondary circuit in cases where the secondary coil receives too much power. Second, it allows us to use multiple secondary coils (each one independently tuning itself) within a single primary coil. This allows for multiple mice (each with implants) to be present in a single cage, where that cage is powered by a primary coil. In the first application, the high induced voltage (due to favourable orientation with the primary) creates a temperature rise in the secondary circuit, which may affect the secondary capacitance (C_S) and leads to a resonant frequency mismatch of the secondary circuit. The high temperature can create problems with the electronic components of the telemetry device, and an implanted device may cause damage to the rodent tissue. A literature review, in

Section 7.2, demonstrated how the resonant frequency mismatch in WPT systems was solved. Researchers used two schemes to eliminate the resonant frequency mismatch problem: Controlling the resonance of the primary circuit with respect to the secondary circuit and controlling the resonance of the secondary circuits of the WPT system. In the second application, we can use this approach for multiple freely moving rodents with RIDs within the same stationary primary coil. This second application is suitable to control the resonance of each secondary circuit (RID) independently. Different initial schematics were built to tune/detune the RID resonance, which did not work properly within the primary electromagnetic field because of the floating ground problem in the L_SC_S-tank circuit. Fig. 67 shows the novel schematic controllable LCWPT system using adjustable magnetic resonance. The resonance of the secondary circuit was controlled by adding/removing capacitors (C_{D*}) into the L_SC_S-tank circuit. This was achieved using MOSFETs with a half-wave bridge (voltage doubler) rectifier. An experimental setup of multiple RIDs was conducted to investigate the mutual coupling effect between the RIDs. These results showed that the maximum drop of the received power was 6% when the edges of the two RIDs at the same orientation touched each other, as listed in Table 20. The mutual coupling of the multiple secondary coils did not present a problem for powering rodent applications; however, the rising temperature caused electronic heating problem for the telemetric devices. Extra received power by the secondary circuit (RID) occurred when the RID was oriented equal to or less than 30° to the primary electromagnetic field. Hence, our proposed controller for rodent applications detuned the resonance of the secondary circuit when the secondary coil induced high voltage that increased the temperature. For rodent applications, every 400 milliseconds the rectified voltage (V_{rec}) was compared to the load requirements to control the resonance of the secondary circuit. Our controller circuit used four switching capacitors (C_{D1}-C_{D4}) to tune/detune the RID, as listed in Table 19. Our novel controllable WPT system allowed us the ability to use freely moving multiple RIDs (telemetry devices) within the same primary coil, where the controller of each RID tunes/detunes its resonance independently of the other RIDs.

The specifications of our design LCWPT based on a two coil system are summarized in Table 21. Our LCWPT was used to power rodent applications, such as an EEG/stimulator. The electrophysiological data were transferred to a base station via a RF communication, as shown in

Fig. 67. The base station was connected to a notebook via an USB cable, where the transmitted data (electrophysiological and V_{rec}) were displayed and saved via a customized GUI.

TABLE 21: FEATURES OF OUR LCWPT SYSTEM USING MAGNETIC RESONANCE COUPLING (1 MHZ)

Circuit	Item	Feature	Note
Primary	Primary coil (L_P)	Wrapped around an acrylic cage (Fig. 40)	The size of the rectangular cage is 250 × 120 × 150 mm^3 (length × width × height)
	Power Amplifier	Series resonance (Fig. 45)	Using high quality factor ceramic capacitors
	DC power	Portable DC battery up to 12 V and 150 mA	Needs 9 V and 140 mA to provide 2 A (peak-to-peak) to the L_P
	Signal generator	Provide a square signal at 1 MHz	Internal/external
Secondary	Secondary coil (L_S)	Wrapped around a PCB with four angled ferrites	Using 4MFA configuration, the size of the rectangular PCB is 18.14 × 11.55 × 1.5 mm^3 (length × width × height)
	LC-tank	Parallel resonance	Using high quality factor ceramic capacitor, its dielectric is independent of temperature and applied voltage
	Energy store	Buffer capacitor (800 μF)	Provide a power for 1.5 sec when the rodent moves to an unfavorable orientation for a brief instant.
	Application device	EEG/stimulator, sampling frequency 410 Hz	Needed power: 51 mW to start up for 100-300 milliseconds and 12 mW for normal operation

Chapter 9: Conclusion, Future Work, and Thesis Contributions

9.1 Conclusion

The WPT system we designed consists of a stationary coil (primary coil) and a free moving telemetry device (secondary coil). The secondary coil can be subcutaneously implanted in a rat or mounted on a mouse head and wrapped around the perimeter of the PCB. To conduct research with rodents effectively, they must be able to move freely inside their cage. However, the continuously changing orientation of the rodent leads to coupling loss/problems between the primary and secondary coils, presenting a major challenge. We designed a novel secondary coil configuration (4MFA) employing four ferrite rods placed at the corners of the PCB and angled at 45^{o} with respect to the PCB plane. The 4MFA coil configuration improved the loose coupling problem as a result of high orientation with respect to the primary electromagnetic field (beyond 60^{o}). The 4MFA configuration received power up to 395 mW when oriented at 0^{o} to the primary electromagnetic field and at the edge of the primary coil. The maximum total efficiency obtained at the center and the edges of the cage were 7.6% and 14.1%, respectively when applying a current of 2 A (peak-to-peak) to the primary coil.

The performance of LCWPT systems is a function of many parameters such as resonance matching, coil quality factor, system impedance match, and others. We designed a novel WMS that collects real-time performance data from the secondary coil circuits while testing LCWPT systems. We built the WMS to greatly reduce such measurement errors when using voltage/current probes or coaxial cables placed directly into the primary magnetic field. Our WMS characterized the properties of the LCWPT systems by measuring the induced voltage and calculating the received power.

Our LCWPT system was designed to transfer the power needed by the telemetric device while it was at a poor orientation and poor position within the primary coil. However, when the secondary coil was oriented equal to or less than 30° to the primary electromagnetic field, extra received power transfer by the secondary coil occurred. This resulted in high induced voltage on the secondary circuit, leading to high temperature that caused electronic heating problem for the telemetric device. A novel control scheme was designed to eliminate the electronic heating problems in the secondary circuit and the resonant frequency mismatch of using the multiple

secondary coils within the same primary coil of the LCWPT system. Furthermore, this novel scheme facilitated the use of multiple secondary circuits (telemetric devices) to operate within a single primary coil, where the internal control algorithm of each RID was able to tune or detune the resonant frequency independently of the others. This allows for applications where multiple rodents (each equipped with a telemetric device) can run around in a stationary primary coil, all receiving adequate power to power their telemetric device regardless of the rodents' position or orientation within the cage. The design controller tuned/detuned the resonance of the secondary circuits (RID) to meet the load requirements of the telemetric devices for rodents.

9.2 Future Work

In order to extend the developments in this thesis for powering implantable biomedical devices using a WPT system, several design improvements can be made in future research. The first improvement is to decrease the size of our secondary coil that is currently too big to be implanted in mice, where the size of the secondary circuit (RID) is 20.25 × 13.25 × 1.7 mm (length × width × height).

The second improvement is to build the WMS as a self-powering system. Our RID communicates wirelessly via radio link to a base station. The base station is connected via USB to a laptop that collects performance data of our LCWPT system and the biological information. We investigated our LCWPT performance using the WMS. We powered our WMS using an external battery to ensure the WMS did not affect the operation and the matched impedance of the SIP/RID. A lithium-polymer battery was used to power the WMS to provide accurate measurements during the experiments and communicate independently to the remote base station via RF [1-2, 53, 152], as shown in Fig. 36. We propose using the matched impedance of the RID that includes the L_SC_S-tank circuit, rectifier circuit, voltage regulator, the MCU, and the application circuit (EEG/stimulator). A vector network analyzer will be needed to characterize the impedance profile of the secondary circuit (application device) during its operation. By using this matched impedance within the RID, the rectified voltage (V_{rec}) can power the MCU via the voltage regulator directly or to charge a battery.

The third improvement is to design a novel rectification system to rectify the induced voltage and adjust the resonance of the secondary circuit. We used a full bridge rectifier in our initial

designs as the full bridge rectifier was suitable for low power applications (such as LCWPT systems) [86, 152]. However, we used a half-wave bridge (voltage doubler) rectifier for controlling the switching capacitors to avoid the floating ground problem in the full bridge rectifiers, as shown in Fig. 67 (explained in Chapter 7). There are two losses associated with the diodes that are explained in Section 4.5. Some researchers investigated replacing the diodes from the full bridge rectifier with MOSFETs [145, 153-155]. The use of the MOSFETs in the full bridge rectifier reduces the conduction losses that are achieved by a lower forward voltage drop in the MOSFETs (with a low on-resistance) than in the diodes. The MOSFETs have a lower conduction loss compared with the diodes, so the efficiency of the WPT systems using the MOSFETs in the rectifier increases [145]. However, the proposed MOSFETs in the rectifier systems [153-155] need to be activated by control signals that drive the gates of the MOSFETs to switch the MOSFETs on/off. These drive control signals synchronize with freewheeling diodes that are connected in parallel with the source-drain MOSFETs to rectify induced voltage efficiently [145]. We recommend designing a controllable secondary circuit that contains a novel schematic design using the MOSFTs for rectifying the induced voltage and tuning/detuning the resonance of the secondary circuit, which will improve the efficiency of the LCWPT systems.

9.3 Thesis Contributions

The main purpose of this thesis was to provide a wireless power transmission to the telemetric devices for rodents, while the rodents move freely inside the cage (primary coil). The novelty of the proposed WPT system itself was comprised of several major developments. These were briefly introduced in Chapter 1, with the details provided by the following:

The first major contribution was to design an energy harvester device based on piezoelectric material. The EHAM was designed to harvest the mechanical energy from mouse movement. An experimental setup was established to compute the PSD of a mouse running using an accelerometer device that was mounted on a mouse head. The highest power of the PSD was observed in the *x*-axis (forward/backward motion) at 11.7 Hz. In order to obtain maximum electrical power, the matched load with the EHAM was used and the resonant frequency of the design EHAM corresponded to 11.7 Hz. FEA COMSOL software was used to simulate the EHAM. The maximum electrical power harvested by EHAM was 68 μW that is insufficient power for the telemetry devices.

The second major contribution was to design and build a WPT system for a freely moving secondary coil (telemetric device for rodents). The rodents (secondary coils) continuously change their orientation which leads to a coupling problem between the primary coil and the secondary coils. A novel secondary coil configuration was designed to eliminate this coupling problem at high orientations (beyond 60°). We built four secondary coil configurations that have same size, inductance, and quality factor. We used FEA COMSOL software to simulate the magnetic flux distribution surrounding the four secondary coil configurations of our design WPT system. The simulation and the experimental results showed that the secondary coil 4MFA configuration improved the power transferred at most orientations.

The third major contribution was to design and construct a measuring system (WMS) to characterize the properties of the WPT systems. The WMS measured the induced voltage onto the secondary coil and transmitted the data to a base station via a RF link. We used the WMS to avoid the measurement errors associated with using coaxial cables and voltage/current probes.

The fourth major contribution was to redesign our LCWPT system to improve the efficiency. Our LCWPT was based on a two coil system that is a stationary primary coil and a freely moving secondary coil. The resonances of the primary and secondary circuits were analyzed and the constructions of the primary and secondary coils were rebuilt to minimize the losses of the LCWPT for rodent applications.

The fifth major contribution was to design a controllable WPT system for rodent applications. We found the high induced voltage onto the secondary coil raised the temperature that caused electronic heating problem for the telemetric devices. We built an adjustable magnetic resonant system capable of tuning and detuning the WPT system, to be able to use multiple secondary coils (telemetry devices) within the same primary coil, and eliminate the rising temperature problem (electronic heating problem). We controlled the resonance of the secondary circuits with respect to the load requirements.

References

[1] B. M. Badr, R. Somogyi-Gsizmazia, N. Dechev, and K. R. Delaney, "Power Transfer via Magnetic Resonant Coupling for Implantable Mice Telemetry Device," presented at 2nd IEEE WPTC, pp. 259-264, Jeju, South Korea, May 8-9, 2014.

[2] B. M. Badr, R. Somogyi-Gsizmazia, K. R. Delaney, and N. Dechev, "Wireless Power Transfer for Telemetric Devices with Variable Orientation, for Small Rodent Behavior Monitoring," *IEEE Sensors Journal*, vol. 15, no. 4, pp. 2144-2156, April 2015.

[3] K. M. Silay, C. Dehollain, and M. Declercq, "A Closed-Loop Remote Powering Link for Wireless Cortical Implants," *IEEE Sensors Journal*, vol. 13, no. 9, pp. 3226-3235, Sept. 2013.

[4] P. Si, A. P. Hu, J. W. Hsu, M. Chiang, Y. Wang, S. Malpas, and D. Budgett, "Wireless Power Supply for Implantable Biomedical Device Based on Primary Input Voltage Regulation," presented at 2nd IEEE ICIEA, pp. 235-239, Harbin, China, May 23-25, 2007.

[5] A. D. Y. Poon, "Miniaturization of Implantable Wireless Power Receiver," in *Implantable Bioelectronics*, Weinheim, Germany: Wiley, ch. 4, pp. 45-64, March 2014.

[6] M. Soma, D. C. Galbraith, and R. L. White, "Radio-Frequency Coils in Implantable Devices: Misalignment Analysis and Design Procedure," *IEEE Trans. Biomed. Eng.*, vol. BME-34, no. 4, pp. 276-282, April 1987.

[7] M. A. Adeeb, A. B. Islam, M. R. Haider, F. S. Tulip, M. N. Ericson, and S. K. Islam, "An inductive link based wireless power transfer system for biomedical applications," *Journal of Active and Passive Electronic Components*, vol. 2012, pp.1-11, March 2012.

[8] M. Ghovanloo and K. Najafi, "A Modular 32-Site Wireless Neural Stimulation Microsystem," *IEEE J. Solid-State Circuits*, vol. 39, no. 12, pp. 2457–2466, Dec. 2004.

[9] P. Wouters, R. Puers, R. Geers, and V. Goedseels, "Implantable Biotelemetry Devices for Animal Monitoring and Identification," presented at 14th IEEE EMBS Conference, pp. 2665–2666, Paris, France, Oct. 29–Nov. 1, 1992.

[10] V. Leonov, P. Fiorini, S. Sedky, T. Torfs, and C. V. Hoof, "Thermoelectric MEMS generators as a power supply for a body area network," presented at 13th IEEE Conference Solid-State Sensors, Actuators and Microsystems, pp. 291-294, Seoul, Korea, June 5-9, 2005.

[11] C.-Y. Sue, and N.-C. Tsai, "Human Powered MEMS-Based Energy Harvest Devices," *Applied Energy*, vol. 93, pp. 390–403, May 2012.

[12] Animal Research Review "Guidelines for the Housing of Mice in Scientific Institutions" (2014, Nov. 16). [Online]. Available: http://www.animalethics.org.au/.

[13] P. Cinquin, C. Gondran, F. Giroud, S. Mazabrard, A. Pellissier, F. Boucher, J.-P. Alcaraz, K. Gorgy, F. Lenouvel, S. Mathé, P. Porcu, S. Cosnier, "A Glucose BioFuel Cell Implanted in Rats," *journal Plos one*, vol. 5, no. 5, pp. 1-7, May 2010.

[14] C. B. Williams, and R. B. Yates, "Analysis of a Micro-Electric Generator for Microsystems," International Conference on Solid-State Sensors and Actuators, pp. 369-372, Stockholm, Sweden, June 25-29, 1995.

[15] B. M. Badr, K. R. Delaney, and N. Dechev, "Design of a Low Frequency Piezoelectric Energy Harvester for Rodent Telemetry," *Journal of Ferroelectrics*, vol. 481, pp. 98-118, Sep. 2015.

[16] B. M. Badr, and W. G. Ali, "Application of Piezoelectric Materials," *Advanced Materials Research*, vol. 189-193, pp. 3612-3620, Feb. 2011.

[17] S. P. Beeby, M. J. Tudor, and N. M. White, "Energy Harvesting Vibration Sources for Microsystems Applications," *Measurement Science and Technology,* vol. 17, no. 12, pp. R175- R195, 2006.

[18] B. M. Badr, K. R. Delaney, and N. Dechev, "Design Piezoelectric Energy Harvesting Using COMSOL for Mice Telemetry Device" presented at the Proceedings of the 2015 COMSOL conference, pp. 1-7, Boston, USA, Oct. 8-10, 2015.

[19] P. Glynne-Jones, S. P. Beeby, and N. M. White, "Towards a Piezoelectric Vibration-Powered Microgenerator," *IEE Proceedings – Science, Measurement and Technology*, vol. 148, no. 2, pp. 68–72, March 2001.

[20] S. Roundy, P. K. Wright, and J. Rabaey, "A study of Low Level Vibrations as a Power Source for Wireless Sensor Nodes," *Computer Communications*, vol. 26, no. 11, pp. 1131–1144, July 2003.

[21] R. Duggirala, H. Li, A. M. Pappu, Z. Fu, A. Apsel, and A. Lal, "Radioisotope Micropower Generator for CMOS Self-powered Sensor Microsystems," Proceeding of 4th International Workshop on Micro and Nanotechnology for Power Generation and Energy Conversion Applications Power MEMS, pp. 133–136, Kyoto, Japan, Nov. 28-30, 2004.

[22] M. Marzencki, S. Basrour, B. Charlot, A. Grasso, M. Colin, and L. Valbin, "Design and Fabrication of Piezoelectric Micro Power Generators for Autonomous Microsystems," Proceeding Symposium on Design, Test, Integration and Packaging of MEMS/MOEMS DTIP05, pp. 299-302, Montreux, Switzerland, June 1-3, 2005.

[23] D. Shen, J.-H. Park, J. Ajitsaria, S.-Y. Choe, H. C. Wikle, and D.-J. Kim, "The Design, Fabrication and Evaluation of a MEMS PZT Cantilever with an Integrated Si Proof Mass for Vibration Energy Harvesting," *Journal of Micromechanics and Microengineering,* vol. 18, no. 5, pp. 055017-055024, 2008.

[24] C. B. Williams, C. Shearwood, M. A. Harradine, P. H. Mellor, T. S. Birch, and R. B. Yates, "Development of an electromagnetic micro-generator," *IEE Proceedings Circuits, Devices Systems*, vol. 148, no. 6, pp. 337–342, Dec. 2001.

[25] M. El-hami, P. Glynne-Jones, N. M. White, M. Hill, S. Beeby, E. James, A. D. Brown, and J. N. Ross, "Design and Fabrication of a New Vibration-Based Electromechanical Generator," *Sensors Actuators A: Physical*, vol. 92, no. 1-3, pp. 335–342, Aug. 2001.

[26] P. Glynne-Jones, M. J. Tudor, S. P. Beeby, and N. M. White, "An Electromagnetic, Vibration-Powered Generator for Intelligent Sensor Systems," *Sensors and Actuators A: Physical*, vol. 110, no. 1-3, pp. 344-349, Feb. 2004.

[27] A. Pérez-Rodríguez, C. Serre, N. Fondevilla, C. Cereceda, J.-R. Morante, J. Esteve, and J. Montserrat, "Design of Electromagnetic Inertial Generators for Energy Scavenging Applications," presented at Proc. Eurosensors XIX, pp. 344-349, Guimaraes, Portugal, 2005.

[28] W. J. Li, Z. Wen, P. K. Wong, G. M. H. Chan, and P. H. W. Leong, "A Micromachined Vibration-Induced Power Generator for Low Power Sensors of Robotic Systems," presented at the 8th International Symposium on Robotics with Applications, Maui, Hawaii, June 11-16, 2000.

[29] N. N. H. Ching, H. Y. Wong, W. J. Li, P. H. W. Leong, and Z. Wen, "A Laser-Micromachined Multi-Modal Resonating Power Transducer for Wireless Sensing Systems," *Sensors Actuators A: Physical*, vol. 97, no. 98, pp. 685–690, April 2002.

[30] S. Meninger, J. O. Mur-Miranda, R. Amirtharajah, A. P. Chandrakasan, and J. H. Lang, "Vibration-to-Electric Energy Conversion," *IEEE Transactions on Very Large Scale Integration (VLSI) Syst.*, vol. 9, no. 1, pp. 64–76, Feb. 2001.

[31] P. D. Mitcheson, P. Miao, B. H. Stark, A. S. Holmes, E. M. Yeatman, and T. C. Green, "Analysis and Optimisation of MEMS On-Chip Power Supply for Self-Powering of Slow Moving Sensors," presented at the 17th European conference on sensors and actuators, pp. 48-51, Guimaraes, Portugal, Sep. 21 – 24, 2003.

[32] Y. Arakawa, Y. Suzuki, and N. Kasagi, "Micro Seismic Power Generator Using Electret Polymer Film," presented at the 4th Micro and Nanotechnology for Power Generation and Energy Conversion Applications Power MEMS, pp. 187–190, Kyoto, Japan, Nov. 28-30, 2004.

[33] G. Despesse, T. Jager, C. Jean-Jacques, J.-M. Léger, A. Vassilev, S. Basrour, and B. Charlot, "Fabrication and Characterization of High Damping Electrostatic Micro Devices for Vibration Energy Scavenging," Proc. Design, Test, Integration and Packaging of MEMS/MOEMS, pp. 386-390, Montreux, Switzerland, June 01-03, 2005.

[34] S. J. Roundy, "Energy Scavenging for Wireless Sensor Nodes with a Focus on Vibration to Electricity Conversion," PhD Thesis University of California, Berkeley, 2003.

[35] M. Herbin, J.-P. Gasc, and S. Renous, "Symmetrical and asymmetrical gaits in the mouse: patterns to increase velocity," *J COMP PHYSIOL A*, vol. 190, no. 11, pp. 895-906, Feb. 2004.

[36] M. Zhu, E. Worthington, and J. Njuguna, "Analyses of Power Output of Piezoelectric Energy-Harvesting Devices Directly Connected to a Load Resistor Using a Coupled Piezoelectric-Circuit Finite Element Method," *IEEE Trans. Ultrason., Ferroelect., Freq. Control.*, vol. 56, no. 7, pp. 1309-1318, July 2009.

[37] B. M. Badr, and W. G. Ali, *Fuzzy Control for Nanopositioning Piezoelectric Actuators*, Germany: VDM Verlag, March 2011.

[38] B. M. Badr, and W. G. Ali, "Identification and Control for a Single-Axis PZT Nanopositioner Stage," presented at 4th international conference ICMSAO, pp. 1-6, Kuala Lumpur, Malaysia, April 19-21, 2011.

[39] H. A. Sodano, and D. J. Inman, "Comparison of Piezoelectric Energy Harvesting Devices for Recharging Batteries," *Journal of Intelligent Material Systems and Structures*, vol. 16, no. 10, pp. 799–807, 2005.

[40] M. Zhu, E. Worthington, and A. Tiwari, "Design Study of Piezoelectric Energy Harvesting Devices for Generation of Higher Electrical Power Using a Coupled Piezoelectric-Circuit Finite Element Method," *IEEE Trans. Ultrason., Ferroelect., Freq. Control.*, vol. 57, no. 2, pp. 427- 437, 2010.

[41] H. Hosaka, K. Itao, and S. Kuroda, "Damping Characteristics of Beam-Shaped Micro-Oscillators," *Sensors and Actuators A: Physical*, vol. 49, no. 1-2, pp. 87-95, Feb. 1995.

[42] P. J. Frey, and P.-L. George, *Mesh Generation: Application to Finite Elements*, UK: ISTE Press, 2000.

[43] S. W. Han, "Wireless Interconnect Using Inductive Coupling in 3D-ICs," PhD Thesis University of Michigan, Michigan, 2012.

[44] D. C. Yates, A. S. Holmes, and A. J. Burdett, "Optimal Transmission Frequency for Ultralow-Power Short-Range Radio Links," *IEEE Trans. Circuits and Systems*, vol. 51, no. 7, pp. 1405–1413, July 2004.

[45] V. Chawla, and D. S. Ha, "An Overview of Passive RFID," *IEEE Communications Magazine*, vol. 45, no. 9, pp. 11-17, Sept. 2007.
[46] W. C. Brown, "The History of Power Transmission by Radio Waves," *IEEE Trans. Microw. Theory Techn.*, vol. 32, no. 9, pp.1230 -1242, Sept. 1984.
[47] L. Summerer, and O. Purcell, "Concepts for Wireless Energy Transmission via Laser," *European Space Agency (ESA)-advanced Concepts Team*, 2009.
[48] G. A. Landis, "RE-Evaluating Satellite Solar Power Systems for Earth," presented at 4th IEEE conference of Photovoltaic Energy Conversion, pp.1939-1942, Waikoloa , Hawaii, May 7-12, 2006
[49] Y. Zhang, Z. Zhao, and K. Chen, "Frequency Decrease Analysis of Resonant Wireless Power Transfer," *IEEE Trans. Power Electron.*, vol. 29, no. 3, pp. 1058-1063, March 2014.
[50] N. Tesla, *The Wireless Tesla*, UK: Wilder Publications, 2007.
[51] D. Fleisch, *A Student's Guide to Maxwell's Equations*, UK: Cambridge University press, 2008.
[52] O. H. Stielau, and G. A. Covic, "Design of Loosely Coupled Inductive Power Transfer Systems", presented at PowerCon, vol. 1, pp. 85 -90, Perth Australia, Dec. 4-7, 2000.
[53] B. M. Badr, Robert Somogyi-Csizmazia, K. R. Delaney, and N. Dechev, "Maximizing Wireless Power Transfer Using Ferrite Rods within Telemetric Devices for Rodents" presented at the Proceedings of the 2015 COMSOL conference, pp. 1-7, Boston, USA, Oct. 8-10, 2015.
[54] N. Tesla, "Apparatus for Transmitting Electrical Energy," USA patent number 1 119 732, Dec. 1914.
[55] INCPR. (2016, April 27). [Online]. Available: http://www.icnirp.org/
[56] C. H. Durney, M. F. Iskander, H. Massoudi, and C. C. Johnson, "An Empirical Formula for Broad-Band SAR Calculations of Prolate Spheroidal Models of Humans and Animals," *IEEE Transactions on Microwave Theory and Techniques*, vol. 27, no. 8, pp. 758-763, 1979.T.
[57] Trezise, "Modelling Inductively Coupled Coils for Wireless Implantable Bio-Sensors, A Novel Approach Using the Finite Element Method", MSc Thesis University of Victoria, Canada, 2011.
[58] S. Ramo, J. R. Whinnery, and T. V. Duzer, *Fields and Waves in Communication Electronics*, New York, USA: Wiley, February 1994.
[59] K. Finkenzeller, *RFID Handbook*, Chichester, UK: Wiley, April 2001.
[60] C. S. Wang, G. A. Covic, and O. H. Stielau, "Power Transfer Capability and Bifurcation Phenomena of Loosely Coupled Inductive Power Transfer Systems," *IEEE Trans. on Industrial Electronics*, vol. 51, no. 1, pp. 148–157, Feb. 2004.
[61] D. M. Budgett, A. P. Hu, P. Si, W. T. Pallas, M. G. Donnelly, J. W. T. Broad, C. J. Barrett, S.-J. Guild, and S. C. Malpas, "Novel technology for the Provision of Power to Implantable Physiological Devices," *Journal of Applied Physiology*, vol. 102, no. 4, pp. 1658-1663, April 2007.
[62] R.-F. Xue, K.-W. Cheng, and M. Je, "High-Efficiency Wireless Power Transfer for Biomedical Implants by Optimal Resonant Load Transformation," *IEEE Trans. Circuits Syst. I, Reg. Papers*, vol. 60, no. 4, pp. 867-874, April 2013.

[63] C. T. Wentz, J. G. Bernstein, P. Monahan, A. Guerra, A. Rodriguez and E. S. Boyden, "A Wirelessly Powered and Controlled Device for Optical Neural Control of Freely-Behaving Animals," *J. Neural Eng.*, vol. 8, no. 4, pp. 1–10, Aug. 2011.

[64] A. N. Laskovski, T. Dissanayake, and M. R. Yuce, "Wireless Power Technology for Biomedical Implants," in *Biomedical Engineering*, Rijeka, Croatia: Intech, ch. 7, pp. 119–132, Oct. 1, 2009.

[65] P. Cong, N. Chaimanonart, W. H. Ko, and D. J. Young, "A Wireless and Batteryless 10-Bit Implantable Blood Pressure Sensing Microsystem With Adaptive RF Powering for Real-Time Laboratory Mice Monitoring," *IEEE J. of Solid-State Circuits*, vol.44, no.12, pp. 3631–3644, Dec. 2009.

[66] N. Soltani, M. S. Aliroteh, and R. Genov, "Cellular Inductive Powering System for Weakly-Linked Resonant Rodent Implants," presented at IEEE BioCAS, pp. 350–353, Rotterdam, Netherlands, Oct. 31–Nov. 2, 2013.

[67] D. Russel, D. McCormick, A. Taberner, M. Lim, and S. Malpas, "Wireless Power Delivery System for Mouse Telemeter," presented at IEEE BioCAS, pp. 273–276, Beijing, China, Nov. 26–28, 2009.

[68] E. G. Kilinc, G. Conus, C. Weber, B. Kawkabani, F. Maloberti, and C. Dehollain, "A System for Wireless Power Transfer of Micro-Systems *In-Vivo* Implantable in Freely Moving Animals," *IEEE J. of Sensors*, vol. 14, no.2, pp. 522–531, Feb. 2014.

[69] U. Jow and M. Ghovanloo, "Geometrical Design of a Scalable Overlapping Planar Spiral Coil Array to Generate a Homogeneous Magnetic Field," *IEEE Trans. Magn.*, vol. 49, no. 6, pp. 2933–2945, June 2013.

[70] D. McCormick, A. P. Hu, P. Nielsen, S. Malpas, and D. Budgett, "Powering Implantable Telemetry Devices from Localized Magnetic Fields," presented at 29th IEEE EMBS Conference, pp. 2331–2335, Lyon, France, Aug. 23-26, 2007.

[71] Q. Xu, H. Wang, Z. Gao, Z. Mao, J. He, and M. Sun, "A Novel Mat-Based System for Position-Varying Wireless Power Transfer to Biomedical Implants," *IEEE Trans. Magn.*, vol. 49, no. 8, pp. 4774-4779, Aug. 2013.

[72] Q. Xu, Z. Gao, H. Wang, J. He, Z. H. Mao, and M. Sun, "Batteries Not Included: A Mat-Based Wireless Power Transfer System for Implantable Medical Devices as a Moving Target," *IEEE Microwave Magazine*, vol. 14, no. 2, pp. 63–72, April 2013.

[73] K. Eom, J. Jeong, T. H. Lee, J. Kim, J. Kim, S. E. Lee, and S. J. Kim, "A Wireless Power Transmission System for Implantable Devices in Freely Moving Rodents," *Med Bio Eng Comput*, vol. 52, no. 8, pp. 639-651, June 2014.

[74] J. U. Hsu, A. P. Hu, P. Si, and A. Swain, "Power Flow Control of a 3-D Wireless Power Pick-up," presented at IEEE ICIEA, pp. 2172–2177, Harbin, China, May 23-25, 2007.

[75] M. K. Hosain, A. Z. Kouzani, S. J. Tye, O. A. Abulseoud, A. Amiet, A. Galehdar, A. Kaynak, and M. Berk, "Development of a Compact Rectenna for Wireless Powering of a Head-Mountable Deep Brain Stimulation Device," *IEEE J. Transl. Eng. Health Med.*, vol. 2, pp. 1-13, April 2014.

[76] R. Ameli, A. Mirbozorgi, J. -L. Néron, Y. LeChasseur, and B. Gosselin, "A Wireless and Batteryless Neural Headstage with Optical Stimulation and Electrophysiological Recording," presented at 35th IEEE EMBS, pp.5662-5665, Osaka, Japan, July 3-7, 2013.

[77] R. Carta, J. Thoné, and R. Puers, "A wireless Power Supply System for Robotic Capsular Endoscopes," *Sensors Actuators A: Physical*, vol. 162, no. 2, pp. 177–183, Aug. 2010.

[78] B. Lenaerts, and R. Puers, *Omnidirectional Inductive Powering for Biomedical Implants*, Netherlands: Springer, 2009.
[79] P. T. Theilmann, and P. M. Asbeck, "An Analytical Model for Inductively Coupled Implantable Biomedical Devices with Ferrite Rods," *IEEE Trans. Biomed. Circuits Syst.*, vol. 3, no. 1, pp. 43-52, Feb. 2009.
[80] Ferrite 4B1. (2014, Oct 15). [Online]. Available: http://www.ferroxcube.com.
[81] M. Pinuela, D. C. Yates, S. Lucyszyn, and P. D. Mitcheson, "Maximizing DC to Load Efficiency for Inductive Power Transfer," *IEEE Trans. Pow. Electronics*, vol. 28, no. 5, pp. 2437–2447, May 2013.
[82] N. O. Sokal and A. D. Sokal, "Class E-A New Class of High-Efficiency Tuned Single-Ended Switching Power Amplifiers," *IEEE J. of Solid-State Circuits*, vol. 10, no. 3, pp. 168–176, June 1975.
[83] Gate driver "MIC4421" (2014, May 16). [Online]. Available: http://www.micrel.com
[84] MOSFET "STP16NK65Z" (2014, May 16). [Online]. Available: http://www.st.com/
[85] Rectifiers"NSDEMN11XV6T1" (2015, May 16). [Online]. Available: http://www.onsemi.com/
[86] G. Vandevoorde, and R. Puers, "Wireless Energy Transfer for Stand-Alone Systems: a Comparison between Low and High Power Applicability," *Sensors and Actuators A: Physical*, vol. 92**,** no. 1-3, pp. 305-311, Aug. 2001.
[87] Z. Yang, W. Liu, and E. Basham, "Inductor modeling in wireless links for implantable electronics," *IEEE Trans. Magnetics*, vol. 43, no. 10, pp. 3851–3860, Oct. 2007.
[88] R. Puers, K. V. Schuylenbergh, M. Catrysse, and B. Hermans, "Wireless Inductive Transfer of Power and Data," in *Analog Circuit Design*, Netherlands: Springer, ch. 18, pp. 395–414, 2006.
[89] Y. Zhao, M. Nandra, C. Yu, and Y. Tai, "High Performance 3-coil Wireless Power Transfer System for the 512-electrode Epiretinal Prosthesis," presented at IEEE EMBS, pp. 6583-6586, San Diego, USA, Aug. 28-Sep. 1, 2012.
[90] M. Dionigi, and M. Mongiardo, "A Novel Coaxial Loop Resonator for Wireless Power Transfer," *International Journal of RF and Microwave*, vol. 22, no. 3, pp. 345-352, Feb. 2012.
[91] M. Dionigi, and M. Mongiardo, "Coaxial Capacitor Loop Resonator for Wireless Power Transfer Systems," presented at the 7th IEEE GeMiC, pp. 1-4, Ilmenau, Germany, March 12-14, 2012.
[92] Microcontroller Nordic "nRF24LE1-F16Q48, Ultra-low Power Wireless System" (2015, June 16). [Online]. Available: www.nordicsemi.com
[93] Application note "RF Design Guidelines: PCB Layout and Circuit and Circuit Optimization", (2015, June 16). [Online]. Available: www.semtech.com.
[94] Application note "AN1294", (2015, June 16). [Online]. Available: www.st.com.
[95] J.-W. Kim, C.-K. Ryu, and Y.-O. Han, "Development of SMD Chip Inductors for RF System Applications," in *Convergence and Hybrid Information Technology*, Berlin: Springer-Verlag, pp. 602-610, 2012.
[96] RF antenna "FR05-S1-N-0-110" (2015, July 16). [Online]. Available: http://www.fractus.com/
[97] P. R. Troyk, and M. A. K. Schwan, "Closed-Loop Class E Transcutaneous Power and Data Link for MicroImplants," *IEEE Trans. Biomed. Eng.*, vol. 39, no. 6, pp. 589-599, June 1992.

[98] C. Alexander, and M. Sadiku, *Fundamentals of Electric Circuits*, USA: McGraw-Hill, 2003.

[99] U.-M. Jow, and M. Ghovanloo, "Design and Optimization of Printed Spiral Coils for Efficient Transcutaneous Inductive Power Transmission," *IEEE Trans. Biomed. Circuits Syst.*, vol. 1, no. 3, pp. 193 -202, Sept. 2007.

[100] J. Kim, E. Basham, and K. D. Pedrotti, "Geometry Based Optimization of Radio-Frequency Coils for Powering Neuroprosthetic Implant," *Med Biol Eng Comput*, vol. 51, no. 1, pp. 123-134, Oct. 2012.

[101] S.-H. Lee, and R. D. Lorenz, "Development and Validation of Model for 95% Efficiency, 220 W Wireless Power Transfer over a 30cm Air-gap," presented at IEEE ECCE, pp. 885-892, Atlanta, USA, Sep. 12-16, 2010.

[102] S. Aldhaher, "Design and Optimization of Switched-Mode Circuits for Inductive Links," Ph.D. thesis, Department of Electrical Engineering, Cranfield University, Bedford, UK, 2014.

[103] C.-S. Wang, O. H. Stielau, G. A. Covic, "Load models and their application in the design of loosely coupled inductive power transfer systems," presented at IEEE PowerCon Conference, Perth, Australia, pp. 1053-1058, Dec. 04–07, 2000.

[104] E. Bou, E. Alarcon, and J. Gutierrez, "A Comparison of Analytical Models for Resonant Inductive Coupling Wireless Power Transfer," presented at Electromagnetics Research Symposium proceedings, pp. 689-693, Moscow, Russia, Aug. 19-23, 2012.

[105] C.-S. Wang, O. H. Stielau, and G. A. Covic, "Design Considerations for a Contactless Electric Vehicle Battery Charger," *IEEE Trans. Ind. Electron,* vol. 52, no. 5, pp. 1308-1314, Oct. 2005.

[106] J. Shin, S. Shin, Y. Kim, S. Ahn, and S. Lee, "Design and Implementation of Shaped Magnetic-Resonance-Based Wireless Power Transfer System for Roadway-Powered Moving Electric Vehicles," *IEEE Trans. Ind. Electron*., vol. 61, no.3, March 2014.

[107] J. Peters, "Design of High Quality Factor Spiral Inductors in RF MCM-D," M. Eng., Dept. of Electrical Engineering and Computer, Massachusetts Institute of Technology, USA, Sep. 2004.

[108] F. Tourkhani, and P. Viarouge, "Accurate Analytical Model of Winding Losses in Round Litz Wire Windings," *IEEE Transactions on Magnetics*, vol. 37, no. 1, pp. 538-543, Jan. 2001.

[109] M. Bartoli, N. Noferi, and A. Reatti, "Modeling Litz-Wire Winding Losses in High-Frequency Power Inductors," presented at 27th IEEE Power Electronics Specialists Conference, pp. 1690–1696, June 23-27, 1996.

[110] Application note, "Litz Wire Technical Information" (2015, June 16). [Online]. Available: www.newenglandwire.com

[111] M. Soma, D. C. Galbraith, and R. L. White, "Transmission of Time Varying Magnetic Field through Body Tissue," *J. Biol. Phys.*, vol. 3, pp. 95–102, June 1975.

[112] A. K. RamRakhyani, S. Mirabbasi, and M. Chiao, "Design and Optimization of Resonance-Based Efficient Wireless Power Delivery Systems for Biomedical Implants," *IEEE Trans. Biomed. Circuits Syst.*, vol. 5, no. 1, pp. 48-63, Feb. 2011.

[113] A. P. Hu, and S. Hussmann, "Improved Power Flow Control for Contactless Moving Sensor Applications," *IEEE Power Electron Lett.*, vol. 2, no. 4, pp. 135-138, Dec. 2004.

[114] K. V. Schuylenbergh, and R. Puers, *Inductive Powering: Basic Theory and Application to Biomedical Systems,* Netherlands: Springer, 2009.

[115] G. A. Kendir, W. Liu, G. Wang, M. Sivaprakasam, R. Bashirullah, M. S. Humayun, and J. D. Weiland, "An Optimal Design Methodology for Inductive Power Link With Class-E Amplifier," *IEEE Trans. Circuits Syst*., vol. 52, no. 5, pp. 857-866, May 2005.
[116] N. O. Sokal, "Class-E RF Power Amplifiers," *Application Note*, Feb. 2001.
[117] M. K. Kazimierczuk and K. Puczko, "Exact analysis of class E tuned power amplifier at any Q and switch duty cycle," *IEEE Trans. Circuits Syst*., vol. 34, no. 2, pp. 149-159, Feb. 1987
[118] P. Jourand, and R. Puers, "A Class-E driven Inductive Power Delivery System Covering the Complete upper Body," *Sensors and Actuators A: Physical*, vol. 183, pp. 132-139, June 2012.
[119] MOSFET "IRF840" (2015, May 16). [Online]. Available: http://www.vishay.com
[120] N. O. Sokal, and A. D. Sokal, "Class-E a New Class of High Efficiency Tuned Single-Ended Switching Power Amplifiers," *IEEE Journal of Solid-state Circuits*, vol. SC-10, no. 3, pp. 168-176, June 1975.
[121] R. L. Bailey, "Large-Signal Nonlinear Analysis of a High-Power High-Frequency Junction Transistor," *IEEE Trans. Electron Devices*, vol. ED-17, no. 2, pp. 108-119, Feb. 1970.
[122] J. T. Boys, G. A. Covic, and A. W. Green, "Stability and control of inductively coupled power transfer systems," *IEEE Proc. Electr. Power Appl.*, vol. 147, no. 1, pp. 37-43, Jan. 2000.
[123] M. Kiani, and M. Ghovanloo, "An RFID-Based Closed Loop Wireless Power Transmission System for Biomedical Applications," *IEEE Trans. Circuits Syst. I, Reg. Papers*, vol. 57, no. 4, pp. 260-264, April 2010.
[124] B. L. Cannon, J. F. Hoburg, D. D. Stancil, and S. C. Goldstein, "Magnetic Resonant Coupling As a Potential Means for Wireless Power Transfer to Multiple Small Receivers," *IEEE Trans. Power Electron*., vol. 24, no. 7, pp. 1819-1825, July 2009.
[125] T. D. Dissanayake, D. M. Budgett, P. Hu, L Bennet, S. Payner, L. Booth, S. Amirapu, Y. Wu, and S. C. Malpas, "A Novel Low Temperature Transcutaneous Energy Transfer System Suitable for High Power Implantable Medical Devices: Performance and Validation in Sheep," *Artificial Organs*, vol. 34, no. 5, pp. 160-17, 2010.
[126] D. C. Ng, S. Bai, J. Y, N. Tran, and E. Skafida, "Wireless Technologies for Closed-Loop Retinal Prostheses," *J Neural Eng*., vol. 6, no. 6, pp. 1-10, Dec. 2009.
[127] V. J. Brusamarello, Y. B. Blauth, R. d. Azambuja, I. Muller, and F. R. d. Sousa, "Power Transfer With an Inductive Link and Wireless Tuning," *IEEE Trans. Instrum. Meas*., vol. 62, no. 5, pp. 924-931, May 2013.
[128] P. Si, A. P. Hu, S. Malpas, and D. Budgett, "A Frequency Control Method for Regulating Wireless Power to Implantable Devices," *IEEE Trans. Biomed. Circuits Syst.*, vol. 2, no. 1, pp. 22-29, March 2008.
[129] S. Hussmann, and A. P. Hu, "A Microcomputer Controlled ICPT Power Pick-up and Its EMC Considerations for Moving Sensor Applications," presented at Proc. Int. Conf. on Power System Technology, pp. 1011-10115, Kunming, China, 13–17 October 2002.
[130] A. Dai and Y. Sun, "An Accurate Frequency Tracking Method Based on Short Current Detection for Inductive Power Transfer System," *IEEE Trans. Ind. Electron.*, vol. 61, no. 2, pp. 776-783, Feb. 2014.
[131] J. James, J. Boys, and G. Covic, "A Variable Inductor Based Tuning Method for ICPT Pickups," presented at 7th IEEE IPEC Conference, Singapore, pp. 1142-1146, Nov. 29–Dec. 2, 2005.

[132] P. Si, A. P. Hu, S. Malpas, and D. Budgett, "Switching Frequency Analysis of Dynamically Detuned ICPT Power Pick-ups," presented at IEEE PowerCon Conference, pp. 1-8, Chongqing, China, Oct. 22-26, 2006.
[133] J.-U. W. Hsu, A. P. Hu, and A. Swain, "A Wireless Power Pickup Based on Directional Tuning Control of Magnetic Amplifier," *IEEE Trans. Ind. Electron.*, vol. 56, no. 7, pp. 2771-2781, July 2009.
[134] J.-U. W. Hsu, A. P. Hu, and A. Swain, "Fuzzy based Directional Tuning Controller for a Wireless Power Pick-up," presented at 10th IEEE TENCON Conference, pp. 1-6, Hyderabad, India, Nov. 19–21, 2008.
[135] G. A. Covic, J. T. Boys, and J. C.-H Peng, "Self Tuning Pick-ups for Inductive Power Transfer," presented at Power Electronics Specialists Conference, pp. 3489-3494, Rhodes, Greece, 15-19 June, 2008.
[136] C.-Y Huang, J. T. Boys, G. A. Covic, and S. Ren, "LCL Pick-up Circulating Current Controller for Inductive Power Transfer Systems," presented at Energy Conversion Congress and Exposition, pp. 640-646, Atlanta, USA, Sep. 12-16, 2010.
[137] Z. Pantic, S. Bai, and S. Lukic, "A New Tri-State-Boost-Based Pickup Topology for Inductive Power Transfer," presented at Energy Conversion Congress and Exposition, pp. 3495-3502, Phoenix, USA, Sep. 17-22, 2011.
[138] J.-U. W. Hsu, A. Swain, and A. P. Hu, "Implicit Adaptive Controller for Wireless Power Pickups," presented at Industrial Electronics and Applications Conference, pp. 514-519, Beijing, June 21-23, 2001.
[139] J.-U. W. Hsu, A. P. Hu, and A. Swain, "Fuzzy Logic-Based Directional Full-Range Tuning Control of Wireless Power Pickups," *Power Electronics, IET*, vol. 5, no. 6, pp. 773-781, Sep. 2012.
[140] Z. Pantic, "Inductive Power Transfer Systems for Charging of Electric Vehicles," Ph.D. thesis, Department of Electrical Engineering, North Carolina State University, Raleigh, North Carolina, 2013.
[141] E. Petersen, "Variable Capacitor for Resonant Power Transfer Systems," US patent number WO2014018968 A2, July 2015.
[142] P. S. Riehl, A. Satyamoorthy, and H. Akram, "Open-Circuit Impedance Control of a Resonant Wireless Power Receiver for Voltage Limiting," US patent number WO2014052686 A2, Sep. 2014.
[143] Y.-C. Yen, P. S. Riehl, H. Akram, and A. Satyamoorthy, "Wireless Power Receiver with Programmable Power Path," US patent number WO2015105924 A1, July 2015.
[144] M. W. Baker, and R. Sarpeshkar, "Feedback Analysis and Design of RF Power Links for Low-Power Bionic Systems," *IEEE Trans. Biomed. Circuits Syst.*, vol. 1, no. 1, pp. 28-38, 2007.
[145] J.-U. W. Hsu, "Full-Range Tuning Power Flow Control of IPT Power Pickups," Ph.D. thesis, Department of Electrical and Electronic Engineering, University of Auckland, Auckland , New Zealand, 2010.
[146] Application note "Comparison of ceramic and tantalum capacitors" (2015, June 16). [Online]. Available: www. Kemet.com.
[147] J. T. Boys, G. A. Covic, and Y. Xu "DC analysis Technique for Inductive Power Transfer Pick-ups," *IEEE Power Electron. Lett.*, vol. 1, no. 2, pp. 51–53, June 2003.

[148] Q. Yu, T. W. Holmes, and K. Naishadham, "RF Equivalent Circuit Modeling of Ferrite-Core Inductors and Characterization of Core Materials," *IEEE Transaction on Electromagnetic Compatibility*, vol. 44, no. 1, pp. 258-262, Feb. 2002.
[149] L. Green, "RF-inductor modeling for the 21st century," *Designfeature*, pp. 67-74, Sept. 2001.
[150] 2N-channel MOSFET "Si1026X" (May 15, 2015). [Online]. Available: www.vishay.com
[151] Two switching diode "DA4J101K0R" (May 15, 2015). [Online]. Available: www.panasonic.com
[152] B. M. Badr, R. Somogyi-Csizmazia, P. Leslie, K. R. Delaney, and N. Dechev, "Design of a Wireless Measurement System for Use in Wireless Power Transfer Applications for Implants," *Journal of Wireless Power Transfer*, 2016.
[153] S.-J. Chen, and H.-C. Chang, "Analysis and Implementation of Low-Side Active Clamp Forward Converters with Synchronous Rectification," presented at 33rd IECON, pp. 1506-1511, Taipei, Taiwan, Nov. 5-8, 2007.
[154] H. K. Ji, and H. J. Kim, "Active Clamp Forward Converter with MOSFET Synchronous Rectification," presented at 25th IEEE PESC, pp. 895-901, Taipei, Taiwan, June 20-25, 1994.
[155] Y. Liu, Y. Jiang, and G.C. Hua, "A Self-Driven Synchronous Rectification Scheme for Low Output Switching-Mode Converter," presented at 4th IPEMC, pp. 1166-1169, Xi'an, China, Aug. 14-16, 2004.

List of Publications

Basem M. Badr, Art Makosinski, Kerry R. Delaney, and Nikolai Dechev, "Controlling Wireless Power Transfer Levels by Controlled Tuning and Detuning of Secondary Tank Resonance," U.S. provisional application No. 62/327,352, filed on April 25, 2016.

Basem M. Badr, Robert Somogyi-Csizmazia, Kerry R. Delaney, and Nikolai Dechev, "Wireless Power Transfer for Devices with Variable Orientation," US Patent Application, no. 14/978,961, filed on December 22, 2015.

Basem M. Badr, R. Somogyi-Csizmazia, P. Leslie, K. R. Delaney, and N. Dechev, "Design of a Wireless Measurement System for Use in Wireless Power Transfer Applications for Implants," *Journal of Wireless Power Transfer,* 2016 (accepted).

Basem M. Badr, K. R. Delaney and N. Dechev, "Design of a Low Frequency Piezoelectric Energy Harvester for Rodent Telemetry," *Journal of Ferroelectrics,* vol. 481, no. 1, Sep. 2015.

Basem M. Badr, Robert Somogyi-Gsizmazia, N. Dechev and K. R. Delaney, "Wireless Power Transfer for Telemetric Devices with Variable Orientation, for Small Rodent Behavior Monitoring," *IEEE Sensors Journal*, vol. 15, no. 4, Oct. 2014.

Basem M. Badr, Robert Somogyi-Csizmazia, Kerry R. Delaney, and Nikolai Dechev, "Maximizing Wireless Power Transfer Using Ferrite Rods within Telemetric Devices for Rodents," COMSOL Conference, Boston, USA, Oct. 7-9, 2015.

Basem M. Badr, Kerry R. Delaney, and Nikolai Dechev, "Design Piezoelectric Energy Harvesting Using COMSOL for Mice Telemetry Device," COMSOL Conference, Boston, USA, Oct. 7-9, 2015.

Basem M. Badr, Robert Somogyi-Gsizmazia, N. Dechev and K. R. Delaney, "Power Transfer via Magnetic Resonant Coupling for Implantable Mice Telemetry Devices," IEEE Wireless Power Transfer Conference (WPTC), Jeju, South Korea, May 8-9, 2014.